Experimental Calibration of Aluminum Partitioning between Olivine and Spinel as a Thermometer

By

Zhihuan Wan
B.Sc., Peking University, 2004

A Thesis Submitted in Partial Fulfillment of the
Requirements for the Degree of

MASTER OF SCIENCE

In the School of Earth and Ocean Sciences

Experimental Calibration of Aluminum Partitioning between Olivine and Spinel as a Thermometer

By

Zhihuan Wan
B.Sc., Peking University, 2004

Supervisory Committee

Supervisor:

Dr. Laurence Coogan, (School of Earth and Ocean Sciences)

Co-Supervisor:

Dr. Dante Canil, (School of Earth and Ocean Sciences)

Departmental Member:

Dr. Kathryn Gillis, (School of Earth and Ocean Sciences)

Departmental Member:

Dr. Stephen Johnston, (School of Earth and Ocean Sciences)

External Examiner:

Dr. James Scoates, (Department of Earth and Ocean Sciences, University of British Columbia)

Supervisory Committee

Supervisor: Dr. Laurence Coogan

Co-Supervisor: Dr. Dante Canil

Departmental Members: Dr. Kathryn Gillis and Dr. Stephen Johnston

External Examiner: Dr. James Scoates

ABSTRACT

An experimental study of the partitioning of aluminum between olivine and spinel was carried out at 100 kPa over the temperature range 1250-1450°C at an oxygen fugacity 1.8 log units below the quartz-fayalite-magnetite buffer in basaltic starting compositions. The partitioning is temperature sensitive and experimental data can be fitted to the relation:

$$T_{Al}(K) = -10500 / \{\ln([Al_2O_3]^{ol}/[Al_2O_3]^{sp}) - 0.98*(Cr\#\text{-}sp-0.5) - 0.75\}$$

where $[Al_2O_3]^{ol}$ and $[Al_2O_3]^{sp}$ are concentrations of Al_2O_3 in olivine and spinel (wt%), and Cr#-sp is $Cr/(Cr+Al+Fe^{3+})$ in spinel. This thermometer is calibrated for olivine with Mg/(Mg+Fe) between 0.87 and 0.93, and spinel with $Cr/(Cr+Al+Fe^{3+})$ between 0.07 and 0.63 and $Fe^{3+}/(Cr+Al+Fe^{3+})$ between 0.02 and 0.05, and it reproduces experimental conditions to ±20°C.

This thermometer generally yields temperatures lower than the two pyroxene thermometer when applied to natural mantle peridotites. The difference may be caused by inaccuracy in both thermometers or by faster Al diffusion in olivine than Ca diffusion in the pyroxenes.

Preliminary investigations of the potential of Cr and Si exchange between olivine and spinel as further geothermobarometers are also presented.

TABLE OF CONTENTS

LIST OF TABLES

LIST OF FIGURES

ACKNOWLEDGEMENTS

I wish to thank first and foremost Dr. Dante Canil and Dr. Laurence Coogan for their wisdom, patience, support, understanding, encouragement and guidance through the course of this work. I am extremely grateful for their help. I also wish to thank Dr. Jody Spence and Dr. Mati Raudsepp for assistance with ICPMS and EMP analyses, respectively, and Jean-Philippe Gagnon and Michael Shelley for helpful discussions on spinel digestion. I also would like to thank Jason Mackenzie and Jeff Larocque for their help with my study. I thank Alice Chang for the help on Microwave spinel digestion and especially for her friendship and support.

Chapter 1

Introduction

1.1 Importance of pressures and temperatures of mantle rocks

When the partition of element(s) between two minerals reaches equilibrium, the exchange coefficients have a fixed relationship with pressure, temperature, and mineral composition (e.g. Köhler and Brey, 1990). Therefore, for natural rocks, the pressure and temperature of equilibrium can be calculated according to the exchange coefficient of the element (e.g. Köhler and Brey, 1990). Mantle-derived rocks have been found in mid-ocean rift zones, in ophiolites, in orogenic belts, and as fragments (xenoliths) carried up by magmas (Arai, 1994; Bodinier and Godard, 2003). The equilibrium pressure and temperature recorded by the element(s) exchange between mineral pairs in these rocks are important parameters in petrology study. For example, the equilibrium pressure and temperature for xenolith samples may represent the pressure and temperature conditions of derivation, and they offer direct evidence for the physical conditions of the upper mantle. The equilibrium pressure and temperature of xenoliths are commonly used to determine the lithosphere geotherm (Arai, 1994; Xu et al, 1999; Nasir et al, 2000).

In mantle-derived rocks, the pressures and temperatures recorded by different equilibria between minerals in a rock sample may be different due to the thermal events and different element diffusion rates within the same mineral and among different minerals. Differences in equilibrium pressures and temperatures constrain the thermal history of the rock sample. For example, in mantle peridotites, Fe-Mg diffusion in olivine and spinel is faster than Ca-Mg diffusion in clinopyroxene and orthopyroxene (Mori,

1977). Therefore, Fe-Mg partitioning between olivine and spinel is more easily to be affected by later thermal events than Ca-Mg equilibrium between clinopyroxene and orthopyroxene. Thus, if a rock is heated (cooled), the temperatures recorded by Fe-Mg olivine-spinel exchange maybe higher (lower) than the temperatures recorded by Ca-Mg exchange between clinopyroxene and orthopyroxene. By comparing the temperatures recorded by different equilibria within the same rock sample, the thermal history of the rock can be determined.

The importance of being able to determine the equilibrium pressure and temperature of mantle samples makes it necessary to have the tool of calibrating the pressure and temperature conditions: geothermobarometry.

1.2 Introduction to geothermobarometry

Geothermobarometry is the discipline of estimating the equilibrium pressure and temperature conditions of a rock based on the chemical compositions and physical state (or both) of one or more minerals in a rock sample (Bohlen and Lindsley, 1987). Geothermobarometry relies on understanding the pressure or temperature dependence of various equilibria between minerals within a given assemblage (Bohlen and Lindsley, 1987). For example, we can consider a reaction of the type:

$$2A + 3B = C + 4D \qquad (1.1)$$

between components *A, B, C* and *D* in a rock. When the reaction reaches equilibrium,

$$\Delta G^0 = -RTln((a_C)(a_D)^4/(a_A)^2(a_B)^3) = -RTlnK \qquad (1.2)$$

where $K = (a_C)(a_D)^4/(a_A)^2(a_B)^3$, where a_x refers the activity of the end-member x, which is a function of the composition and the activity coefficients of the mineral; R is the gas

constant (8.31 $JK^{-1}mol^{-1}$); ΔG^0 is the Gibbs energy change of Reaction (1.1) at the standard state. In this case the standard state is defined as $P = 1\ bar$ and T of interest. Additionally, ΔG^0 can also be expressed as:

$$\Delta G^0 = \Delta H_{1bar,T} + (P\text{-}1)\,\Delta V^0 - T\Delta S^0 \qquad (1.3)$$

where $\Delta H_{1bar,T}$ is the enthalpy change of Reaction (1.1) at $P = 1\ bar$ and T of interest, ΔV^0 is the volume change of the reaction and is assumed to be independent of P and T, and ΔS^0 is the entropy change of the reaction (Wood and Fraser, 1976). Therefore,

$$-RT\ln K = \Delta H^0 + (P\text{-}1)\,\Delta V^0 - T\Delta S^0 \qquad (1.4)$$

Differentiating Equation (1.4) with respect to T at constant P and with respect to P at constant T derives the following equations (Wood and Fraser, 1976):

$$(d\ln K/dT)_P = (-\Delta H^0 - (P\text{-}1)\,\Delta V^0)/RT^2 \qquad (1.5)$$

$$(d\ln K/dP)_T = \Delta V^0/RT \qquad (1.6)$$

If ΔH^0 is large and ΔV^0 is small, K depends more on T than on P, and the reaction makes a good geothermometer. In contrast, if ΔV^0 is large and ΔH^0 is small, K is more sensitive to P than T, and the reaction makes a good geobarometer.

There are many types of geothermometers and geobarometers (e.g. Bohlen and Lindsley, 1987) including those based on trace element partitioning between two co-existing phases (Bohlen and Lindsley, 1987; White, 1995; Blundy and Wood, 2003). The distributions of trace elements (i) between co-existing phases (a and b) are represented by the partition coefficient:

$$D_i^{a/b} = [i]^a/[i]^b \qquad (1.7)$$

where $[i]^x$ is the concentration of element (or species) i in phase x. At low concentrations, the activity coefficient of the trace element is constant according to Henry's law. Thus,

$D_i^{a/b}$ can be used to represent K to develop geothermometer or geobarometer (White, 1995). Alternatively, some elements occur as trace elements in one phase but as major elements in others. In this case, because of the nonlinear relationship between the concentration and the activity of a non-trace element, a composition factor is usually contained in the final version of the geothermometer or geobarometer. (e.g. Stosch, 1981; Witt-Eickschen and O'Neill, 2005).

1.3 Limitation of the geothermobarometry for spinel peridotites

The upper mantle is composed mostly of spinel peridotite, a rock consisting of more than 60% (volume) olivine, with pyroxene and spinel (Figure 1.1; Winter, 2001). Spinel peridotites are stable in the low-pressure regions of the upper mantle (Figure 1.1; Kushiro and Yoder, 1966; Green and Ringwood, 1967). As pressure increases, spinel peridotite transforms into garnet peridotite (Figure 1.1; Klemme, 2004). At pressures less than 1 GPa, plagioclase, instead of spinel, can be the stable Al-rich phase and the peridotite is called plagioclase peridotite (Figure 1.1; Cohen et al, 1967).

The most widely used geothermometer for estimating the equilibrium temperature of spinel peridotites is the two pyroxene solvus thermometer (e.g. Brey and Köhler, 1990), which is based on Ca-Mg exchange between clinopyroxene and orthopyroxene (Figure 1.2). However, in some peridotite types, such as dunite, no pyroxene is present and many harzburgites contain no clinopyroxene (Bodinier and Godard, 2003). This makes the application of the two pyroxene solvus thermometer difficult. Olivine and spinel are always present in spinel peridotites (Kushiro and Yoder, 1966; Green and Ringwood, 1967). However, a thermometer based on Mg-Fe^{2+} exchange between olivine

and spinel (Irvine, 1965; Fabries, 1977; O'Neill and Wall, 1987; Ballhaus et al, 1991; Kretz, 1994) generally yields different temperatures from that of the two pyroxene solvus thermometer (Mori, 1977; Fabries, 1979; Smith, 1999). This is because $Mg\text{-}Fe^{2+}$ equilibrium between olivine and spinel is easily affected by late-stage thermal events due to the fast diffusion of Mg and Fe^{2+} in olivine and spinel (Mori, 1977; Fabries, 1979; Smith, 1999). Therefore, new geothermometers based on elements that have slow diffusion rates in olivine and spinel would have wide applicability to studies of the Earth's uppermost mantle.

The only geobarometer that exists for spinel peridotites is based on Ca partitioning between olivine and clinopyroxene (Köhler and Brey, 1990). However, the estimation of equilibrium pressure for spinel peridotites using this barometer is problematic (Xu et al, 1999) because of: 1) the large temperature dependence of this barometer, 2) the common disequilibrium in Ca partitioning between olivine and clinopyroxene due to rapid exchange of Ca between olivine and clinopyroxene during late thermal events, and 3) the difficulty in precise measurement of Ca content in olivine with an electron microprobe (Köhler and Brey, 1990). Therefore, new geobarometers are needed to better constrain the pressure at which spinel peridotites equilibrated.

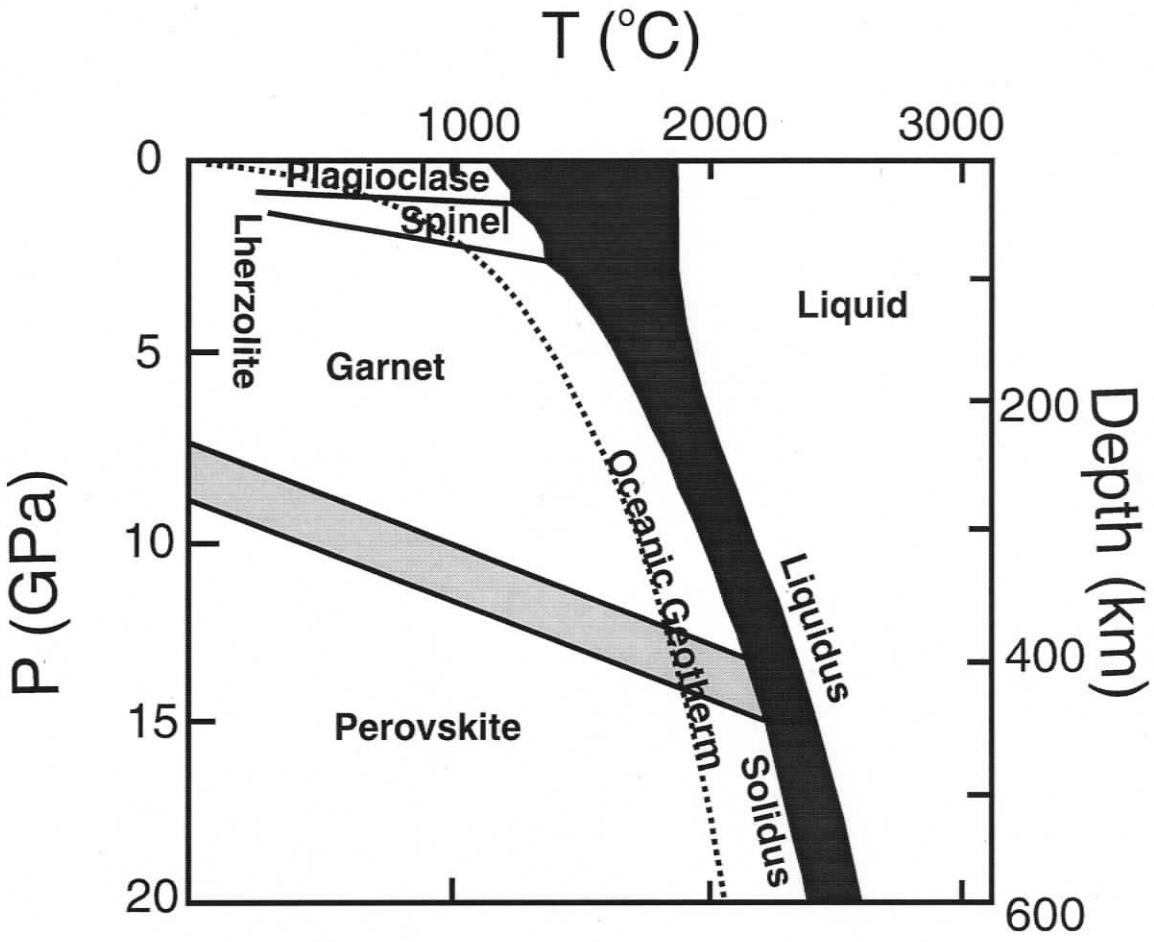

Figure 1.1 Stability fields of upper mantle rock types (plagioclase lherzolite, spinel lherzolite, and garnet lherzolite), with oceanic geotherm (dashed line) and the lherzolite solidus and liquidus (Modified after Winter, 2001). Lherzolite is the most common type of peridotite. The black area represents the melting interval.

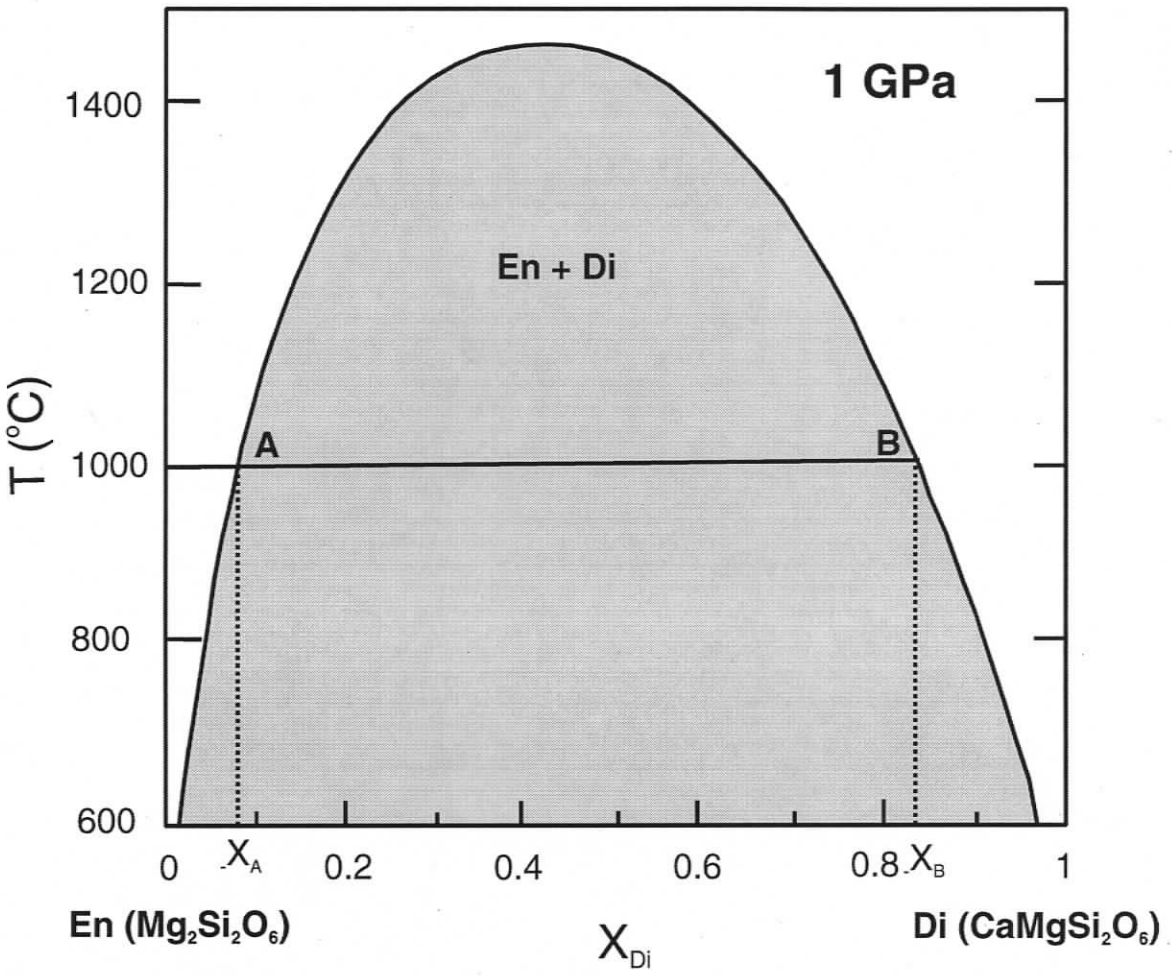

Figure 1.2 Illustration of phase relationships in the system $Mg_2Si_2O_6$ (enstatite: En) – $CaMgSi_2O_6$ (diopside: Di) (Modified after White, 1995). X_{Di} = Ca/(Mg+Ca). The grey area represents the region where two pyroxenes coexist. Compositions of pyroxenes A and B are dependent on T. For example, at T = 1000°C, the composition of the orthopyroxene A is $X_{Di} = X_A$, and the composition of the clinopyroxene B is $X_{Di} = X_B$.

1.4 Exchange of Al, Cr, and Si between olivine and spinel

The general formula for olivine is M_2TO_4. The M cations are normally Mg and Fe with a small amount of other divalent cations such as Ca, Mn, and Ni. The T cations are almost exclusively Si. The structure of olivine is shown in Figure 1.3. Most naturally occurring olivine in spinel peridotites can be treated as a solid solution between two end-members: Mg_2SiO_4 (forsterite) and Fe_2SiO_4 (fayalite).

The spinel group is composed of a series of minerals with the general formula AB_2O_4 (Deer et al, 1996). Spinel has two typical structural types: normal structure and inverse structure (see Figure 1.4). The most common end-members of spinel in peridotities are: spinel ($Mg^{2+}Al^{3+}{}_2O_4$), chromite ($Fe^{2+}Cr^{3+}{}_2O_4$), magnetite ($Fe^{2+}Fe^{3+}{}_2O_4$), and ulvospinel ($Fe^{2+}{}_2Ti^{4+}O_4$) (Deer et al, 1996).

Olivine and spinel can exchange cations by ionic substitution. For high valence cations such as Cr^{3+}, Al^{3+}, and Si^{4+}, substitutions between olivine and spinel require compensating charge balance substitutions. Thus, Cr^{3+} and Al^{3+} occur as trace elements in olivine, and Si^{4+} occurs in trace amounts in spinel.

Olivine is stable at low pressure and transforms into a denser spinel structure at elevated pressure (Sung and Burns, 1978). This transformation occurs in the transition zone of the Earth's mantle (Sung and Burns, 1978). It is generally accepted that olivine (α-Mg_2SiO_4) undergoes a phase transition to the wadsleyite (β-Mg_2SiO_4) at depths of about 410 km, and at about 520 km depth, wadsleyite transforms into the spinel-structured ringwoodite (γ-Mg_2SiO_4). The difference between the three structures is that oxygen atoms in the α structure are nearly hexagonally closed-packed, but in the β and γ

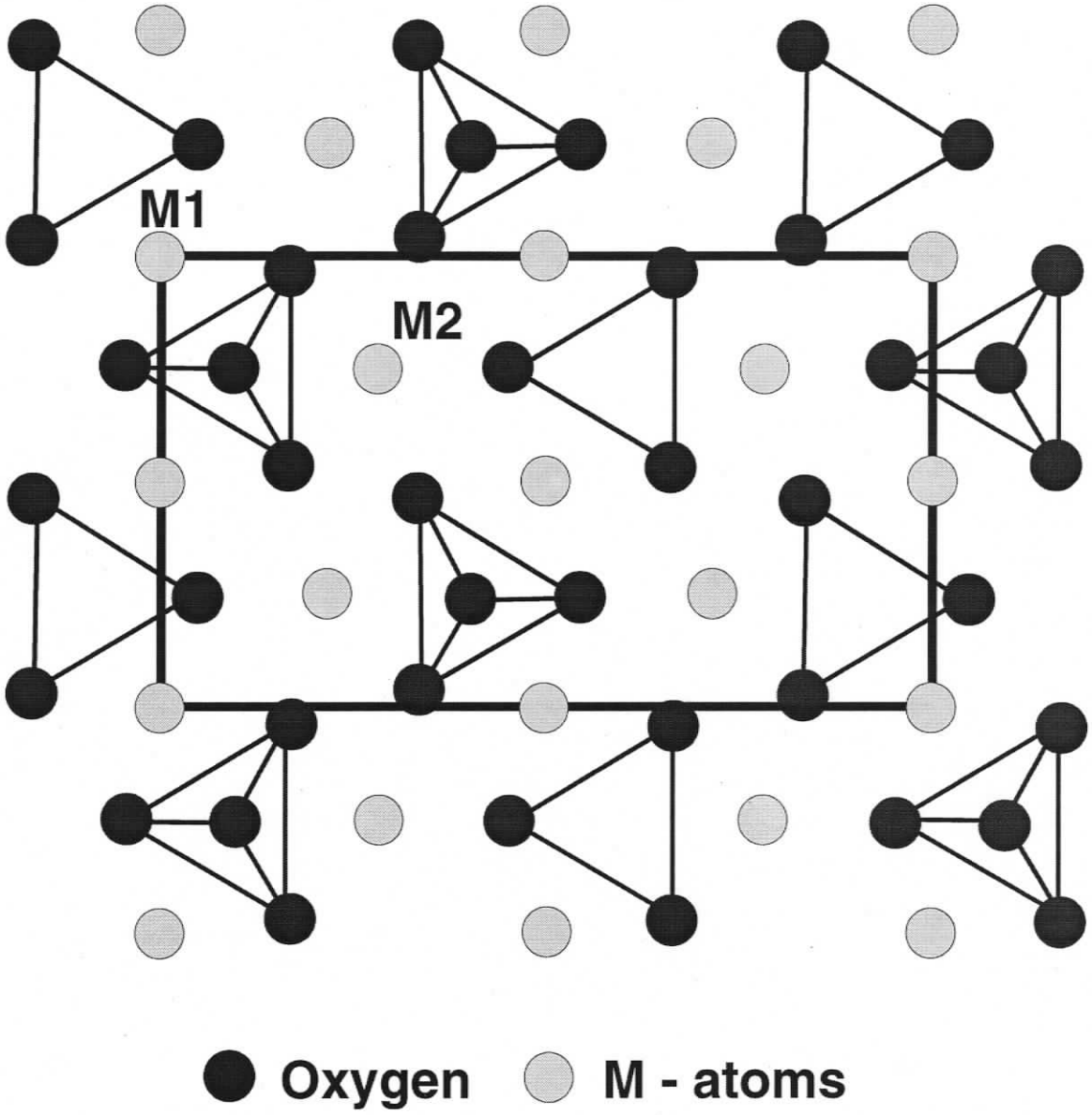

Figure 1.3 Atomic scale structure of olivine ($(Mg,Fe)_2SiO_4$) looking along the a-axis (modified after Deer et al, 1996). The M – atoms are mainly Mg and Fe atoms: M1 are at centers of symmetry and M2 are on reflection planes. Silicon atoms at the centers of the O-tetrahedra are not shown. A projection of the unit cell is shown by the black rectangle.

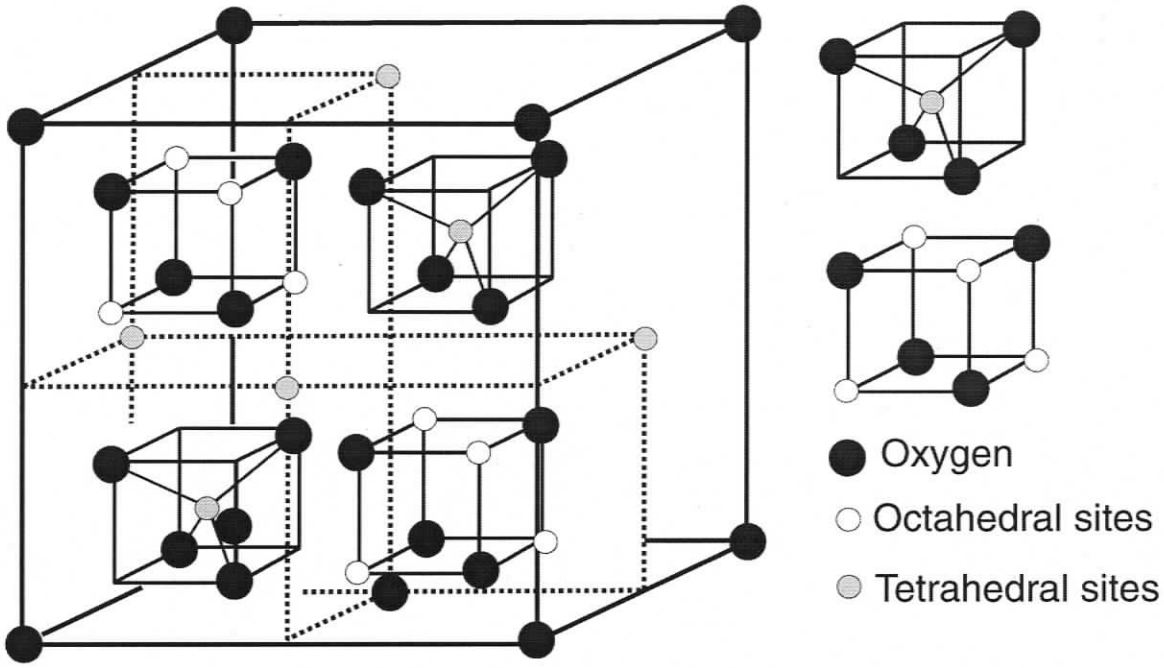

Figure 1.4 Spinel (AB_2O_4) unit cell (modified after Deer et al, 1996). The dashed lines are drawn to divide the front half of the unit cell into 4 equal parts to better visualize the spinel structure. The small cubes shown to the right side of the unit cell are also contained in the back half of the unit cell. The A cations are divalent and B cations are trivalent. Oxygen atoms have a cubic close-packed structure. In a normal spinel structure, all the A cations occupy the tetrahedral sites, and all the B cations occupy the octahedral sites (Deer et al, 1996). In an inverse spinel structure, 1/2 of the B cations occupy the tetrahedral sites, and all the A cations and 1/2 of the B cations occupy the octahedral sites (Deer et al, 1996).

structures they approximate cubic close-packing in the spinel structure (Sung and Burns, 1978). The transformation of olivine to spinel structure may be written as

$$Mg_2SiO_4 = Mg_2SiO_4 \qquad (1.8)$$

olivine spinel

The transformation from olivine to spinel at elevated pressure may be considered as Reaction (1.8) moves towards the spinel direction with increasing pressure. Thus, Si partitioning between olivine and spinel should increase with increasing pressure. Therefore, Si partitioning between olivine and spinel was studied with the aim of developing a geobarometer. However, due to problems in developing standards for Si in spinel analyses and time constraints, this project was not completed. A preliminary discussion on this subject is given in Chapter 2.

It has been suggested that Cr and Al substitution into the olivine structure is temperature and pressure sensitive (Agee and Walker, 1994; Taura et al, 1998). For this reason, the dependence of the partition coefficient of Al_2O_3 and Cr_2O_3 between olivine and spinel ($D_{Al}^{ol/sp}$ and $D_{Cr}^{ol/sp}$) on temperature was investigated in this study using experimental methods at 100 kPa (Chapter 3). Since Cr and Al occur as major elements in spinel, the activities of these two elements do not simply follow a linear relationship with concentration. Thus, the dependence of $D_{Al}^{ol/sp}$ and $D_{Cr}^{ol/sp}$ on spinel composition was also investigated experimentally (Chapter 3). The dependence of $D_{Al}^{ol/sp}$ and $D_{Cr}^{ol/sp}$ on pressure was studied by comparing the experimental results in the present study with published experimental results at high pressure (100 kPa – 2 GPa). Two thermometers applicable to spinel-bearing peridotites are provided in this study (Chapters 3).

Chapter 2

Pilot study of silicon partitioning between olivine and spinel

2.1 Introduction

As discussed in Chapter 1, olivine transforms into a denser spinel structure as pressure increases (Sung and Burns, 1978), which suggests that the Si partitioning between olivine and spinel may be pressure dependent. Thus, with the aim of developing a geobarometer for spinel-bearing peridotite, an empirical study of Si partitioning between olivine and spinel was carried out. Mantle rocks containing orthopyroxene, clinopyroxene, olivine, and spinel believed to have equilibrated at variable pressure and temperature conditions were collected. Silicon contents of spinel in these samples were analyzed using Laser Ablation Inductively Coupled Plasma Mass Spectrometry (LA-ICPMS). However, analytical challenges prevented complete calibration of Si concentrations in spinel. This chapter briefly outlines the progress made and suggests future work necessary to complete this project.

2.2 Sample suite studied

Samples chosen for this study (Table 2.1) included eight spinel peridotite samples from the oceanic lithosphere (seven samples from the Oman ophiolite and one sample from the Southwest Indian Ridge), five on-craton spinel-garnet peridotite xenoliths from

the Jericho Kimberlite in the Slave craton, and ten off-craton spinel peridotite xenoliths from the southern Canadian Cordillera (Table 2.1). For the spinel peridotite samples, the equilibrium pressures of the xenolith samples were assumed to be 1.5 GPa, the equilibrium pressures of samples from the Oman ophiolite were calculated according to the depth of the sample (personal communication, Coogan LA, University of Victoria, 2007), and the equilibrium pressure of the sample from the Southwest Indian Ridge was assumed to be 0.5 GPa (personal communication, Coogan LA, University of Victoria, 2007). The two pyroxene solvus thermometer (T_{BKN}; Brey and Köhler, 1990) was used to calculate the equilibrium temperatures of spinel peridotite samples. The equilibrium pressures and temperatures of spinel-garnet peridotites were calculated using the garnet-orthopyroxene Al exchange barometer of Brey and Köhler (1990) combined with T_{BKN} (Brey and Köhler, 1990).

Table 2.1 Natural samples for Si partitioning between olivine and spinel study

Sample	Type	Type	Location	Cr#-sp	Mg#-sp	P (GPa)	T_{BKN} (°C)	Reference
2001OL24	Ocea Lith	Sp Peri	Oman	0.51	0.52	0.48	986	PersCom Coogan, 2007
2001OL3	Ocea Lith	Sp Peri	Oman	0.53	0.57	0.24	808	PersCom Coogan, 2007
2001OL4	Ocea Lith	Sp Peri	Oman	0.55	0.56	0.24	886	PersCom Coogan, 2007
2001OL43	Ocea Lith	Sp Peri	Oman	0.51	0.57	0.54	846	PersCom Coogan, 2007
2001OL45	Ocea Lith	Sp Peri	Oman	0.65	0.47	0.57	765	PersCom Coogan, 2007
2001OL47	Ocea Lith	Sp Peri	Oman	0.38	0.66	0.63	797	PersCom Coogan, 2007
JR31-52-5	Ocea Lith	Sp Peri	SWIR	0.17	0.76	0.5	902	PersCom Coogan, 2007
22-1	On-C Xeno	Gt-sp lher	Jericho Kimberlite	0.40	0.69	2.6	674	Kopylova et al, 1999
22-4	On-C Xeno	Gt-sp lher	Jericho Kimberlite	0.80	0.43	4	824	Kopylova et al, 1999
22-5	On-C Xeno	Gt-sp lher	Jericho Kimberlite	0.84	0.46	4.1	930	Kopylova et al, 1999
25-4	On-C Xeno	Gt-sp lher	Jericho Kimberlite	0.81	0.42	5.5	993	Kopylova et al, 1999
26-11	On-C Xeno	Gt-sp lher	Jericho Kimberlite	0.81	0.44	4.5	947	Kopylova et al, 1999
JL1	Off-C Xeno	Sp lher	BC Jaques Lake	0.09	0.78	1.5	1001	Canil et al, 1990; Fujii & Scarfe, 1982
JL8	Off-C Xeno	Sp lher	BC Jaques Lake	0.14	0.77	1.5	836	Canil et al, 1990; Fujii & Scarfe, 1982
KLBR-1	Off-C Xeno	Sp lher	BC Kostal Lake	0.19	0.64	1.5	1122	Canil et al, 1990
KR1034	Off-C Xeno	Sp lher	BC West Kettle River	0.07	0.81	1.5	984	Canil et al, 1990
KR35	Off-C Xeno	Sp lher	BC West Kettle River	0.10	0.76	1.5	-	Canil et al, 1990
KR37	Off-C Xeno	Sp lher	BC West Kettle River	0.20	0.77	1.5	-	Canil et al, 1990
RR222	Off-C Xeno	Sp lher	BC Rayfield River	0.10	0.79	1.5	928	Canil et al, 1990
SL125	Off-C Xeno	Sp lher	BC Summit Lake	0.18	0.71	1.5	1099	Canil et al, 1990
SL32	Off-C Xeno	Sp lher	BC Summit Lake	0.13	0.73	1.5	1120	Canil et al, 1990
TKN15	Off-C Xeno	Sp lher	BC Boss Mountain	0.10	0.78	1.5	958	Canil et al, 1990; Fujii & Scarfe, 1982

Ocea Lith: oceanic lithosphere. On-C: On-craton. Off-C: Off-craton. Xeno: Xenolith. Sp: spinel. Gt: garnet. Lher: lherzolite. Peri: peridotite. SWIR: Southwest Indian Ridge. BC: British Columbia. Mg#-sp: Mg/(Mg+Fe) ratio of spinel. Cr#-sp: Cr/(Cr+Al) ratio in spinel. P: pressure. Pressure is described in the text. PersCom: Personal Communication. T_{BKN}: temperature calculated using the two pyroxene thermometer calibrated by Brey and Köhler (1990). The T_{BKN} values for samples KR35, and KR37 could not be calculated because of the lack of orthopyroxene compositions.

2.3 Analytical methods

2.3.1 Introduction

Spinel analyses were carried out using ICPMS. The ICPMS is a fast, precise and accurate analytical technique for the determination of trace elements (< 0.1 wt%) in liquid and solid samples (Thomas, 2001a). In ICPMS, the liquid or solid sample material is introduced to an inductively coupled Ar plasma, and ionized (Longerich and Diegor, 2001). Ions are then extracted from the Ar plasma into a high vacuum enclosure and focused by an ion lens system, and enter a mass spectrometer (Longerich and Diegor, 2001). Analyte isotopes are separated according to their mass/charge ratio by the mass spectrometer, and measured by a detector (Longerich and Diegor, 2001).

Although ICPMS is a powerful technique for measuring trace element contents, it is susceptible to spectral interference, instrument fluctuation and drift, and matrix effects (Longerich and Diegor, 2001). Spectral interference comes from ions that have the same mass to charge ratio as the analyte. In Si in spinel analyses using LA-ICPMS, N_2 from air is introduced to the plasma and can interfere with Si analyses due to the same mass to charge ratio of 28. Some of the LA-ICPMS analyses in this study were carried out using a VG PQ II S+ ICPMS and the others were carried out using a Thermo-Electron X7 ICPMS. For the VG PQ II S+ ICPMS, the interference caused severe background at mass 28, and a low RF power was employed in this study to reduce the background signal of mass 28. However, the interference of N_2 on mass 28 for the Thermo-Electron X7 ICPMS is not as problematic as that for the VG PQ II S+ ICPMS.

Another factor limiting the precision in LA-ICPMS is the instrument fluctuation (Ridder et al, 2002). The instrument fluctuation usually causes instrument drift, which is

an artificial pattern appearing in the raw signals of all analytes (Ridder et al, 2002). An internal standard is usually employed to normalize the signal of the analyte to overcome this limitation (Ridder et al, 2002). An external standard is essential to quantify the concentrations of the analyte in samples, and it provides a secondary correction to the instrument drift. The possible internal standards for Si in spinel analyses are ^{57}Fe, ^{55}Mn, and ^{54}Cr since these elements occur in sufficient amount in spinel, and these isotopes suffer from the least spectral interferences among all the isotopes of these elements. Although instrument drift also appears in the signal of the internal standard, the ideal internal standard should have the same signal sensitivity between spinel samples and the external standard after the effect of instrument drift on the signal being corrected using the external standard. In this study, isotopes ^{57}Fe, ^{55}Mn, and ^{54}Cr were investigated with the aim of finding an appropriate internal standard.

The "matrix effect" is the enhancement or suppression of the analyte signal sensitivity because of the presence of major elements or reagents (Iglesias, et al, 2004). Since matrix effects can be a problem in the ICPMS, external standards with a matrix as similar to the samples as possible should be employed to ensure the same signal sensitivity, especially for the internal standard, between samples and the standards. In this study, different external standards were tested. This is discussed in detail in the next section.

2.3.2 Standards

To fully quantify the Si contents of spinel samples, external standards with known Si contents are needed. There are a few options for external standards: natural spinels,

synthetic spinels, or metallic standard reference materials. Natural and synthetic spinel standards were developed with Si contents analyzed by solution ICPMS. The major and minor element contents (including Si) in these standards were analyzed using an Electron Microprobe (EMP). Natural and synthetic spinels were also tested on LA-ICPMS. The standard reference material should have similar Si contents to samples. Steel standard 2175 was chosen and purchased from the US National Institute of Standards and Technology (NIST).

The three natural spinels used in this study are two gem-quality spinels from Mogok and Vietnam and one spinel from India (Supplied by Canil D and Coogan LA, University of Victoria). These natural spinel standards range in size from 1 mm to 2 mm. They were carefully crushed, and examined under the binocular microscope. Pieces that were free of inclusions were hand-picked. One partion of the picked natural spinel standard pieces were mounted in epoxy and polished for LA-ICPMS analysis. A second part was digested for solution ICPMS analysis.

Synthetic spinels were sintered from mixtures of reagent grade oxides at the same ratio as that for the oxide compositions of $Mg_{0.545}Fe_{0.455}(Al_{0.4}Cr_{0.6})_2O_3$ (synthetic spinel standard 1), $Mg_{0.435}Fe_{0.565}(Al_{0.1}Cr_{0.9})_2O_3$ (synthetic spinel standard 2), and $Mg(Al_{0.6}Cr_{0.4})_2O_3$ (synthetic spinel standard 3). Reagent grade oxides (MgO, Fe_2O_3, Al_2O_3, and Cr_2O_3) were weighed, mixed, and transferred into a 1 cm platinum crucible and sintered at 1375°C and quartz-fayalite-magnetite (QFM) oxygen fugacity for 24 hours. The sintered mix was then drilled out of the Pt crucible using a steel drill, and crushed in an agate mortar. The sintering process was repeated three times. Part of the powder was digested for solution ICPMS analysis. A second part of the powder was hot-

pressed in a piston-cylinder apparatus at 1 GPa and 1000°C for 24 hours in a Au capsule to produce a pellet. The synthetic spinel pellets were mounted in epoxy and polished for LA-ICPMS analysis.

The steel standard 2175 is in the form of 0.1-0.2 mm thick pieces. It contains 20.5wt% Cr, 33.4wt% Co, 0.9wt% Fe, 9.5wt% Mo, 34.9wt% Ni, 0.7wt% Ti, 0.012wt% Mn, and 0.02% Si. As with the natural and synthetic standards, this standard was mounted in epoxy and polished for LA-ICPMS analysis.

2.3.3 Silicon in natural and synthetic spinel analyses: EMP and solution ICPMS

The major and minor element (including Si) contents in natural spinel standards and synthetic spinel standards 1 and 2 were analyzed using EMP. The EMP analyses were carried out with a CAMECA SX50 EMP at the University of British Columbia at a 15.0 kV acceleration voltage and a beam current of 39.8 nA with a 1-2 μm beam. Analytical conditions were 20 s counting time on peak and background for all elements except for Al (60 s) and Cr (60 s). Analysis spots were distributed widely across the grains for natural spinel standards. Synthetic spinel standards were found to be inhomogeneous under the Scanning Electron Microscope. Spinel crystals 1-5 μm in size are spread evenly across individual grain, and unidentified materials exist between the crystals. Both the spinel crystals and the unidentified materials were analyzed using EMP for synthetic spinel standard 2. Only the spinel crystals were analyzed using EMP for synthetic spinel standard 1.

To determine the Si concentrations in spinel standards accurately, complete digestion of the standard followed by solution ICPMS analysis was required. Spinel

dissolution, however, is well known to be difficult. The solubility of spinels in acids decreases with increasing Cr# (e.g Jurczyk et al, 1993; Eggins et al, 1997). Previously, spinel digestion has been carried out at elevated temperature, elevated pressure (e.g. microwave), long duration, high concentration of reagent by acid decomposition and/or the help of flux, and combining the microwave method with the ultrasound apparatus (Appendix 1).

Different methods of spinel digestion were tested in this study (Appendices 1 and 2). The best method of spinel digestion proved to be in phosphoric acid (H_3PO_4) at high temperature (290°C). Phosphoric acid (H_3PO_4) dehydrates upon heating (Lagasse et al, 2001). The acid converts to pyrophosphoric acid ($H_4P_2O_7$), and then to triphosphoric acid ($H_5P_3O_{10}$) as it condenses further (Lagasse et al, 2001). Eventually it becomes phosphorous pentoxide: P_2O_5 (Lagasse et al, 2001). Since the only volatile is water in this process, no special precautions other than a fume hood and cautious initial heating is required (personal communication, Shelley M, The Australian National University, 2006). For this procedure, 15 mg of Cr-free spinel and 15 mg of Cr-rich spinel were digested in 3 ml and 5 ml ULTREX II ultrapure reagent phosphoric acid on a hotplate at about 250°C over a period of 7 days. Samples were shaken twice a day to increase digestion efficiency. The solutions were transferred into high density polyethylene (HDPE) bottles and diluted with deionized water to a dilution factor of 600 to reduce the viscosity of the solution for ICPMS analysis. To avoid matrix effects, standard addition was used for solution ICPMS analyses. The final solution for each sample was divided into three aliquots and spiked with 0, 200, and 400 ppb Si, respectively. By comparing the signal and concentration differences of Si in the three aliquots, Si contents in the

aliquots with zero Si spike can be calculated. Therefore, the Si contents in the spinel samples can be quantified.

Solution ICPMS analyses were carried out using a Thermo-Electron X7 ICPMS. Data acquisition was performed in peak-jumping mode, acquiring individual intensity data for each analyte isotope during each mass spectrometer sweep. Isotopes of ^{10}B, ^{27}Al, ^{28}Si, ^{29}Si, ^{30}Si, ^{55}Mn, and ^{56}Fe were monitored. The dwell time was 10 ms on ^{10}B, ^{27}Al, ^{29}Si, ^{30}Si, ^{55}Mn, and ^{56}Fe and 100 ms on ^{28}Si. The acquisition time for each sample was 17 seconds in total with a 2.5 minute rinse of 1% environmental grade Nitric acid between each of three aliquots and a 0.5 minute break between two aliquots. All data manipulation was done manually off-line. Operating conditions employed for the solution ICP-MS instrument are listed in Table 2.3.

2.3.4 Testing natural and synthetic spinel standards: LA-ICPMS

The Mogok spinel, Vietnam spinel, and three natural and three synthetic spinel standards were also analyzed using LA-ICPMS. The analyses were carried out using a Thermo-Electron X7 ICPMS and a Merchantek UV LA Microprobe. Spot analysis with 100 μm spot size was employed. Isotopes of ^{10}B, ^{25}Mg, ^{27}Al, ^{28}Si, ^{53}Cr, and ^{57}Fe were monitored. Data acquisition was performed in peak-jumping mode, acquiring individual intensity data for each analyte isotope during each mass spectrometer sweep. The dwell time was 10 ms on ^{10}B, ^{25}Mg, ^{27}Al, ^{53}Cr, and ^{57}Fe, and 30 ms for ^{28}Si. The Mogok spinel was analyzed at the beginning and the end of the run as a drift correction standard. Operating conditions employed are listed in Table 2.2.

2.3.5 Analysis of spinel samples: LA-ICPMS

Natural peridoite samples were carefully crushed, minerals were separated, and spinel crystals were hand-picked under a binocular microscope. Each spinel grain was mounted in epoxy and polished. For each sample, about five spinel grains were analyzed by LA-ICPMS with one analysis at the center of each grain. The analyses were carried out using a VG PQ II+ ICPMS and a Merchantek UV LA Microprobe. Spot analyses with spot size of 100 μm were employed. Low RF power (900 Watts) was used to reduce the background of ^{28}Si. Data acquisition was performed in peak-jumping mode, acquiring individual intensity data for each analyte isotope during each mass spectrometer sweep. The dwell time on each mass was 10 ms. Steel 2175 was used as the external standard. Three analyses on the external standard were carried out at the beginning and the end of each set of sample analysis and between every 10 analyses. The external standard was also analyzed before and after changing samples. Operating conditions employed for these analyses are listed in Table 2.2.

Table 2.2 Optimized instrumental measurement settings for the ICPMS instrument

Instrumental settings	LA-ICPMS for spinel samples	Solution ICPMS for natural and synthetic spinel standards	LA-ICPMS for natural and synthetic spinel standards
ICPMS	VG PQ II+ ICPMS	Thermo-Electron X7 ICPMS	Thermo-Electron X7 ICPMS
Forward RF power (Watts)	900	1400	1435
Nebuliser gas flow (L/min)	0.58	0.9	0.84
Carrier He gas flow (L/min)	1.25	1.9	1.02
Auxiliary Ar gas flow (L/min)	0.92	0.8	0.8
Cooling Ar gas flow (L/min)	15	13	13
Isotopes monitored	^{10}B, ^{27}Al, ^{28}Si, ^{29}Si, ^{54}Cr, ^{55}Mn, ^{57}Fe	^{10}B, ^{27}Al, ^{28}Si, ^{29}Si, ^{30}Si, ^{55}Mn, ^{56}Fe	^{10}B, ^{25}Mg, ^{27}Al, ^{28}Si, ^{53}Cr, ^{57}Fe

2.4 Results

2.4.1 Silicon contents in natural and synthetic spinel standards

Major and minor element contents in spinel standards analyzed by EMP are shown in Table 2.3. The unidentified material in synthetic spinel standard 2 contains 46% SiO_2 and 51wt% Al_2O_3, while spinel crystals contain only 0.04±0.08wt% SiO_2 and 5.60±0.57wt% Al_2O_3 (Table 2.3). This demonstrates the inhomogeneity of the synthetic spinel standards at the scale of 1-2 μm. The unidentified materials might be mixtures of the oxides Al_2O_3 and SiO_2. Oxide SiO_2 might come from the agate mortar when the standards were crushed. The natural spinel standards are homogeneous at the scale of 1-2 μm since one standard deviation of the major element concentrations is always less than 0.5wt%, and the difference between the minor element concentrations from each analysis for the same sample is within the analytical precision of EMP (Table 2.3).

Solution ICPMS analyses was undertaken by standard addition. The signals of ^{28}Si from ICPMS for three aliquots from each sample were regressed against the spiked Si content (e.g. Figure 2.1). The intercept of the extrapolated line with the Si spike axis is the position of zero Si concentration. Once the position of zero Si concentration is known, Si concentration at zero Si spike can be calculated (Figure 2.1). Silicon contents in spinel standards obtained in this way and those analyzed by EMP analyses are shown in Table 2.4. Silicon contents in natural spinel standards analyzed by ICPMS are almost all at the detection limit and those measured by EMP (36-66 ppm) are close to the detection limit. Silicon contents in synthetic spinel standards obtained from solution ICPMS are 800-2000 ppm. This high Si concentration must come from the unidentified materials because they are so much greater than Si concentrations measured by EMP.

Table 2.3 Major and minor element concentrations (wt%) for natural and synthetic spinel standards.

Label	Mogok sp		Vietnum sp		ZnMg-Al sp		Syn-sp-std-2-sp		Syn-sp-std-2-um		Syn-sp-std-1	
No	12		10		11		5		2		7	
	ave	1σ	ave	1σ	ave	1σ	ave	1σ	ave	1σ	ave	1σ
MgO	28.34	0.16	28.73	0.15	28.63	0.15	7.61	3.21	1.10	0.06	11.91	0.17
Al_2O_3	70.15	0.30	70.34	0.23	70.51	0.34	5.60	0.57	51.30	0.63	21.67	0.24
SiO_2	0.01	0.01	0.01	0.01	0.02	0.01	0.04	0.08	45.91	0.46	0.01	0.01
CaO	0.00	0.00	0.00	0.00	0.01	0.01	0.00	0.00	0.09	0.00	0.01	0.00
TiO_2	0.05	0.02	0.03	0.02	0.07	0.01	0.01	0.01	0.09	0.03	0.00	0.01
V_2O_3	0.15	0.02	0.14	0.02	0.28	0.12	0.01	0.01	0.05	0.05	0.02	0.01
Cr_2O_3	0.35	0.14	0.55	0.06	0.31	0.11	68.87	6.09	0.85	0.10	47.98	1.10
MnO	0.00	0.01	0.01	0.01	0.01	0.02	0.00	0.00	0.02	0.01	0.00	0.00
*FeO	0.31	0.03	0.17	0.03	0.32	0.05	17.43	3.86	0.22	0.04	17.22	0.67
NiO	0.02	0.02	0.02	0.02	0.01	0.02	0.01	0.01	0.00	0.00	0.02	0.01
total	99.40		99.99		100.17		99.58		99.63		98.83	99.40

* represents total Fe as FeO. Syn-sp-std: synthetic spinel standard. Sp: spinel. um: unidentified material. No: number of analyses. 1 σ: one standard deviation of all the analyses. Data for all spinel standards are acquired from EMP analyses. Synthetic spinel standard 3 was not analyzed by EMP due to time constraints.

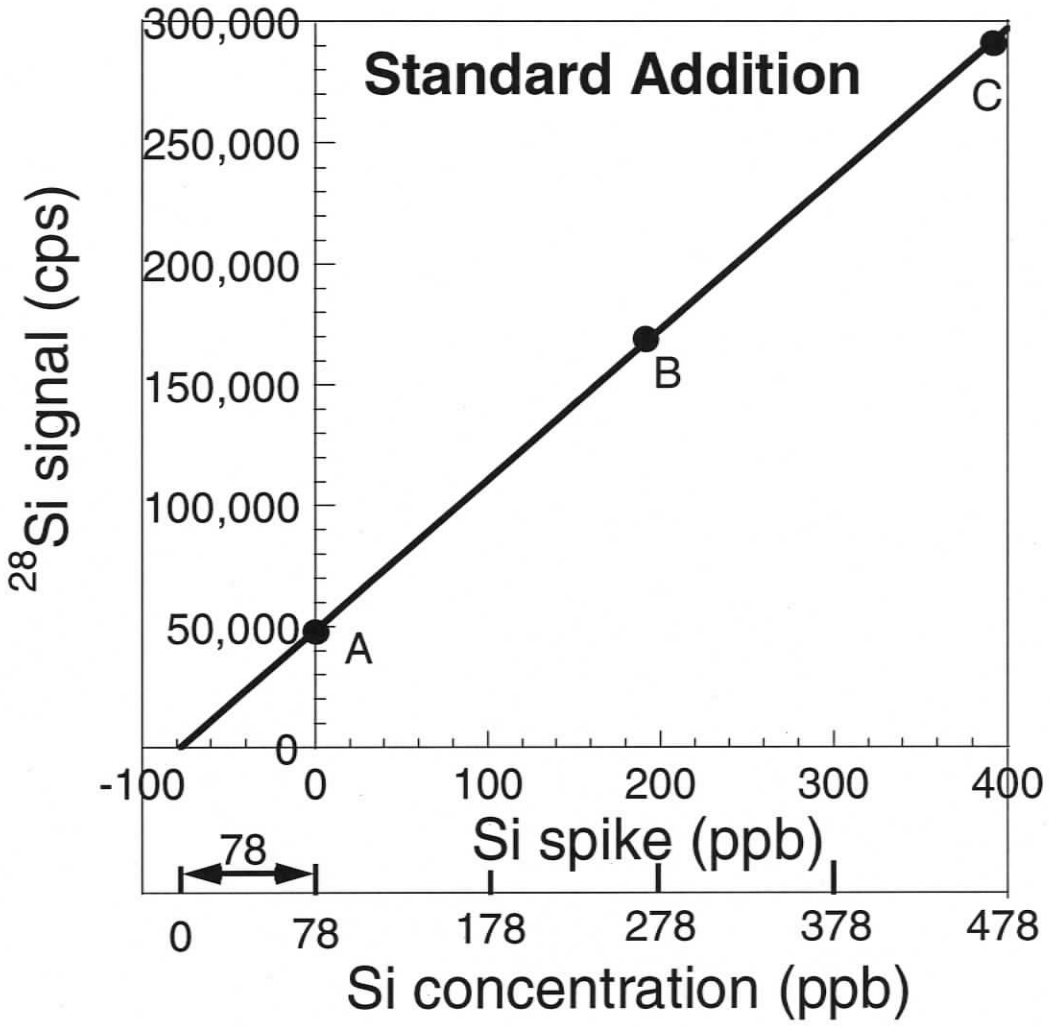

Figure 2.1 Standard addition method for silicon concentration in the Vietnam spinel solution. "A", "B", and "C" represent three aliquots A, B, and C. Silicon spike axis is the concentration of added Si after it has been mixed with sample. Silicon concentration axis is also shown. The solid line is the linear regression of three data points. The solid line intersects the Si spike axis at -78. At $x_{Si\ spike}$ = -78, the signal of ^{28}Si is zero, which suggests that the Si concentration is zero. This indicates that the Si concentrations in solutions A, B, and C are 78 ppb higher than the spiked Si contents. Therefore, at $x_{Si\ spike}$ = 0, the Si concentration in solution A is 78 ppb.

Table 2.4 Silicon contents in spinel standards analyzed using solution ICPMS and EMP

Sample	Si (ppm) - solution ICPMS	Si (ppm) - EMP
Mogok sp	0	66 ± 35
Vietnam sp	2.66	33 ± 24
ZnMg-Al sp	0	55 ± 13
Syn-sp-std-1	2003	177 ± 356
Syn-sp-std-2	798	25 ± 28
Syn-sp-std-3	1932	-

Syn-sp-std: synthetic spinel standard. Synthetic spinel standard 3 was not analyzed by EMP. For Si (ppm) – EMP column, the concentration is the average of the analyses and the error represents the one standard deviation of the analyses.

2.4.2 Homogeneity of the spinel standards at the scale of 100 μm: LA-ICPMS results

To test the homogeneity of the natural and synthetic spinel standards in the scale of 100 μm, the raw signals for isotopes ^{25}Mg, ^{27}Al, ^{53}Cr, and ^{57}Fe from LA-ICPMS were collected and corrected for the effect of instrument drift.

Drift correction is accomplished by assuming linear changes in instrument response, and interpolating the linear change for the samples bracketed by the drift standard (in this case Mogok spinel). For example, for a total of 50 analyses and a change of 100% in the measured signal of ^{57}Fe in the Mogok spinel, the signal of ^{57}Fe would be adjusted by 2% in the first sample, by 4% in the second sample, by 6% in the third sample, etc.

One standard deviation of corrected signals of ^{25}Mg, ^{27}Al, ^{53}Cr, and ^{57}Fe in the spinel standards is used to test their homogeneity. One standard deviation of the signal of the four isotopes for Vietnam spinel and synthetic spinel standards 1, 2, and 3 is between 5% and 15%. One standard deviation of the signal of the four isotopes for Mogok spinel is higher: between 21% and 37%. This suggests that Vietnam spinel and synthetic spinel standards 1, 2, and 3 are homogeneous in the scale of 100 μm, and they are suitable to be used as external standards for Si in spinel analyses by laser ablation provided a large spot size is used. The Mogok spinel is not a suitable external standard for Si in spinel analyses in the present study.

2.4.3 Matrix effect: Isotope signal sensitivities are different in different matrices

Matrix effects are found to be a severe problem in the present study. This is shown by the different signal sensitivities of ^{57}Fe, ^{54}Cr, and ^{55}Mn (after instrument drift

correction) between different spinel samples and the steel standard. It is also shown by the different signal sensitivities of ^{25}Mg, ^{27}Al, ^{53}Cr, and ^{57}Fe (after instrument drift correction) between natural and spinel standards with different matrices. Signal sensitivity is calculated using the signal of the monitored isotope divided by the concentration (wt%) of the element in spinel for each analysis.

Drift corrections for signal sensitivities of ^{57}Fe, ^{54}Cr, and ^{55}Mn from the spinel sample analyses are the same as for the natural and spinel standards discussed in Section 2.4.2. Corrected signal sensitivities of ^{57}Fe, ^{54}Cr, and ^{55}Mn in spinel samples and the steel standard are plotted against the contents of Fe, Cr, and Mn in spinel samples and the steel standard (Figures 2.2a, b, and c). As the spinel samples and the steel standard do not have the same matrix, signal sensitivities for ^{57}Fe, ^{54}Cr, and ^{55}Mn are not the same for the steel standard and spinel samples (Figures 2.2a, b, and c). The dependence of signal sensitivities of ^{57}Fe, ^{54}Cr on Fe and Cr concentrations is not clear (Figure 2.2 a and b). The signal sensitivity of ^{55}Mn decreases with increasing Mn contents in spinel samples, but this trend does not apply to the steel standard (Figure 2.2c). In addition, the steel standard does not produce stable signals for ^{57}Fe, ^{54}Cr, and ^{55}Mn in LA-ICPMS analyses. This is shown by the relatively large one standard deviation of the corrected signal sensitivities of these isotopes (Figure 2.2). For the above reasons, the steel standard 2175 cannot be used as an external standard to calibrate Si concentration in spinel. Therefore, Si contents in spinel samples cannot be quantified at present.

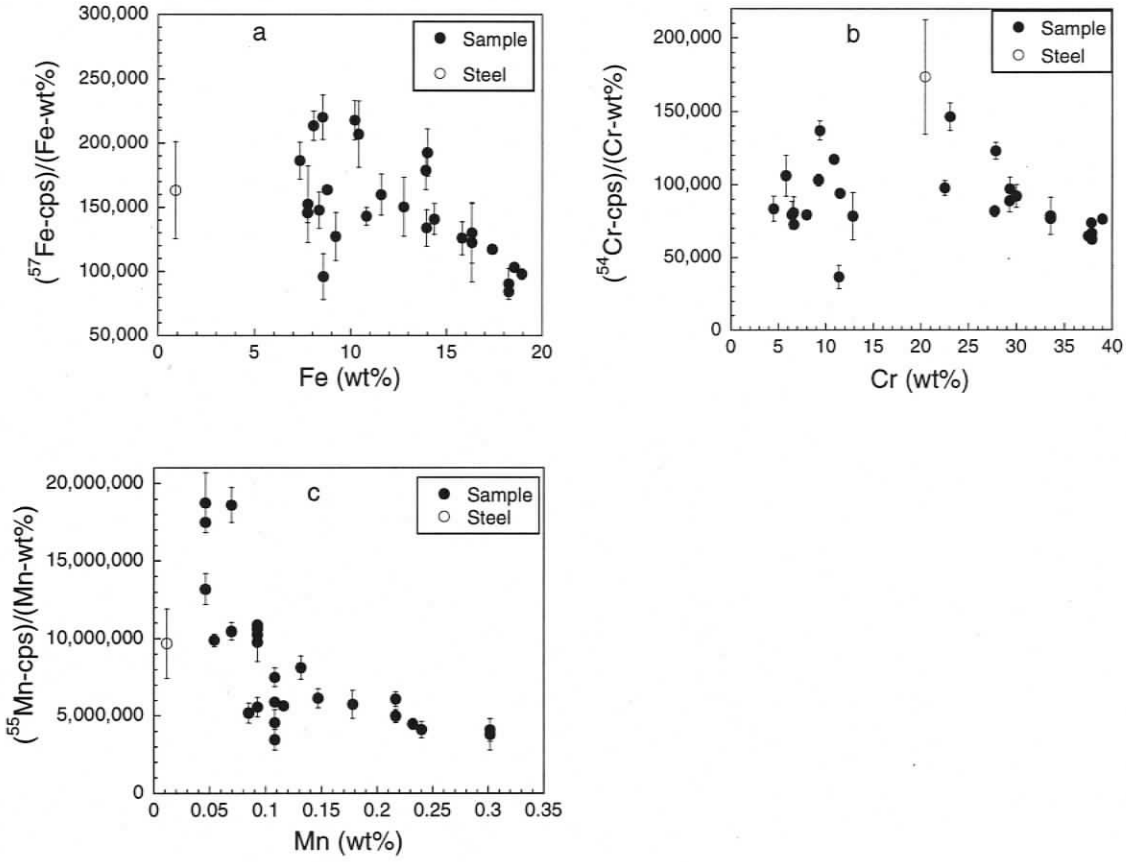

Figure 2.2 Matrix effects in spinel analyses using LA-ICPMS. Signal sensitivities of isotopes ^{57}Fe (a), ^{54}Cr (b), and ^{55}Mn (c) are the values after the drift correction. "Steel" in the label represents the standard reference material 2175 from the US National Institute of Standards and Technology. Symbols represent the average corrected signal sensitivities for each sample, and error bars represent one standard deviation of the corrected signal sensitivities for corresponding samples.

The effect of the matrix on signal sensitivities for potential internal standards is also shown in the results of LA-ICPMS analyses on natural and synthetic spinel standards (Figure 2.3). The signal sensitivity of ^{25}Mg, ^{27}Al, ^{53}Cr, and ^{57}Fe varies amongst different spinel standards. The wide range of the matrix of these standards gives the opportunity to study the matrix effect. The Mogok spinel, Vietnam spinel, and synthetic spinel standard 3 all have Mg# (Mg/(Mg+Fe)) = 1 and can be used to study the effect of Cr# (Cr/Cr+Al+Fe^{3+}) on signal sensivities of ^{25}Mg, ^{27}Al, ^{53}Cr, and ^{57}Fe. As shown in Figures 2.3a, c, e, and g, signal sensitivities of these four isotopes for Cr-free spinel standards (Mogok spinel and Vietnum spinel) are the same and signal sensitivities of the four isotopes for the synthetic spinel standard 3 (Cr# = 0.4) are always higher than those for Cr-free natural spinel standards. This might suggest that Al in spinel suppresses the signal sensitivities of analytes. The signal sensitivities of ^{25}Mg, ^{53}Cr, and ^{57}Fe are similar for the Cr-bearing synthetic spinel standards 1 and 2. The signal sensitivity of ^{27}Al for synthetic spinel standard 1 is higher than that for synthetic spinel standard 2. The reason for the difference between the signal sensitivities of ^{25}Mg, ^{27}Al, ^{53}Cr, and ^{57}Fe between synthetic spinel standards 1 and 2 and Cr-free spinel standards is not well constrained because both Cr# and Mg# vary in synthetic spinel standards 1 and 2. Because the signal sensitivity for potential internal standards appears to be matrix dependent, this study was unable to quantify Si concentrations in spinel samples.

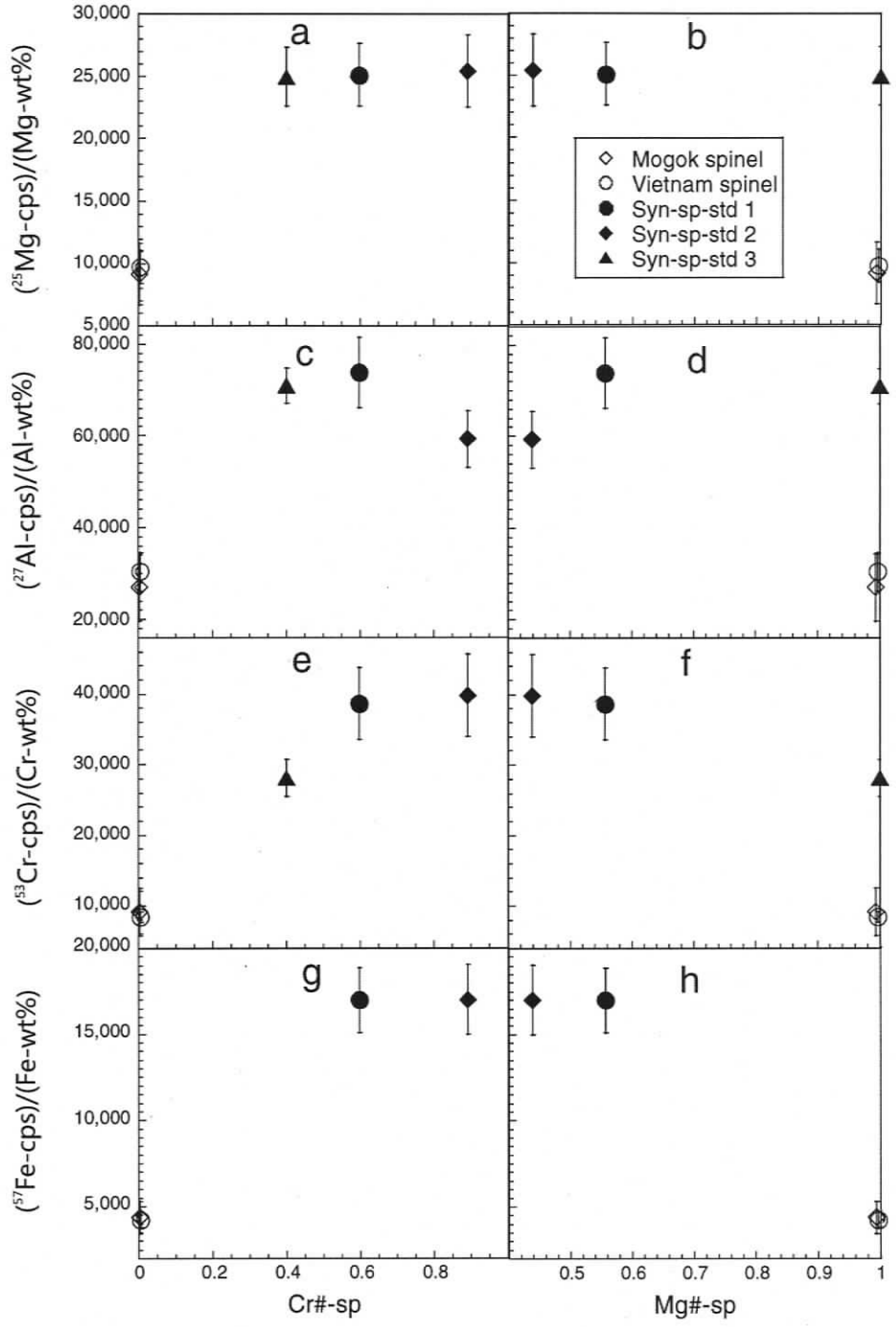

Figure 2.3 Matrix effect investigation by LA-ICPMS. The y axes are signal sensitivities (after drift correction) of monitored isotopes. Symbols represent the average of signal sensitivities for all the analyses. Error bars represent one standard deviation. The ZnMg-Al spinel was not analyzed.

2.5 Summary and future work

In order to study Si partitioning between olivine and spinel, the Si contents in spinel need to be analyzed accurately and precisely. External and internal standards need to be employed to quantify the Si contents in spinel. Natural spinel standards and synthetic spinel standards are developed in this study and synthetic spinel standards are suggested to have the potential for providing external standards for spinel analyses. Matrix effects are found to be problematic. The signal sensitivity of possible internal standards varies between samples and a NIST steel standard. The LA-ICPMS analyses on natural and synthetic spinel standards with different Cr# and Mg# give some insight into the matrix effect, but are not sufficient enough to fully understand the problem. Therefore, silicon contents in spinel samples are not able to be quantified.

Future work should attempt to understand the effect of major element concentrations in spinel on signal sensitivities of the chosen internal standard (e.g. ^{25}Mg, ^{57}Fe, ^{54}Cr, and ^{55}Mn). Synthetic spinel standards with a range of Cr# from 0 to 1 with constant Mg# and with a range of Mg# from 0.4 to 1 with constant Cr# should be developed to investigate the effect of Cr# and Mg# on signal sensitivities of the internal standard. Synthetic spinel standards should be only crushed in a steel mortar to avoid Si contamination. The sinter process should be repeated more than three times to improve the homogeneity of the synthetic spinel standards. To improve the precision of Si in spinel analyses, the background at mass 28 in LA-ICPMS needs to be reduced, probably by using the collision cell technique.

Chapter 3

Experimental study of aluminum and chromium partitioning between olivine and spinel

3.1 Introduction

Chromium and Al substitutions into the olivine structure were suggested to be temperature and pressure sensitive by previous work (e.g. Agee and Walker, 1994; Taura et al, 1998). In this chapter, an investigation on previous experimental studies that have both olivine and spinel in the experimental result (e.g Gaetani and Grove, 1998; Schwab and Johnston, 2001) for Al and Cr partitioning between olivine and spinel is carried out and the investigation shows that the partition coefficients of Al and Cr between olivine and spinel ($D_{Al}^{ol/sp}$ and $D_{Cr}^{ol/sp}$) are temperature sensitive. A preliminary thermodynamic study on Al partitioning between olivine and spinel is also performed in this chapter and it suggests that $D_{Al}^{ol/sp}$ is dependent on both the temperature and the Cr# of spinel. In order to precisely calibrate the thermometers based on Al and Cr partitioning between olivine and spinel, a series of experiments at 100 kPa over a temperature range of 1250°C to 1450°C and at an oxygen fugacity (fO_2) of 1.8 log units below the quartz-fayalite-magnetite (QFM) oxygen fugacity buffer are carried out. The relationship between the partition coefficient of Al between olivine and spinel ($D_{Al}^{ol/sp}$) and Cr# of spinel is investigated at constant temperature (1350°C), and the relationship between $D_{Al}^{ol/sp}$ and temperature is studied at constant Cr# of spinel (0.5). Combining the two relationships gives a thermometer based on Al partitioning between olivine and spinel (the Al thermometer). The developed Al thermometer can be applied to any rock that has

coexisting olivine and spinel of which the compositions are within the calibration range. The same method for calibrating the Al thermometer is used to calibrate a thermometer based on Cr partitioning between olivine and spinel. However, the dependence of $D_{Cr}^{ol/sp}$ on Cr# of spinel is not well constrained by the data. A preliminary thermometer based on Cr partitioning between olivine and spinel is proposed. Additionally, the effect of pressure on Al and Cr partitioning between olivine and spinel is investigated by comparing the experimental results from the present study and previous experiments at elevated pressures. The effect of Fe^{3+}# (Fe^{3+}/(Fe^{3+}+Al+Cr)) of spinel on Al and Cr partitioning between olivine and spinel is also studied by comparing the experimental results for calibrating thermometers at $\log(fO_2)$ = QFM – 1.8 and the results of another series of experiments at high fO_2 (QFM + 3.5-5). Finally, using the present study and previous experimental studies, different versions of the Mg-Fe exchange between olivine and spinel thermometer are tested as this is the only other thermometer that is applicable for olivine and spinel.

3.2 Previous work on aluminum and chromium substitution into the olivine structure

In this section, the dependence of Al and Cr partitioning between olivine and coexisting liquid on temperature and pressure is investigated based on previous studies (e.g. Taura et al, 1998). The dependence of Al and Cr partitioning between olivine and spinel on temperature is investigated based on a collection of published experimental studies that have both olivine and spinel in the experimental results. These investigations suggest that Al and Cr partitioning between olivine and spinel are promising thermometers.

3.2.1 Pressure and temperature dependence of Al and Cr partitioning between olivine and liquid

Published experimental results on Al and Cr partitioning between olivine and coexisting liquid are employed to study the pressure and temperature dependence of Al and Cr substitution into the olivine structure (Figure 3.1). These experimental results show that at pressures higher than 0.5 GPa, the olivine/liquid partition coefficient for Al_2O_3 ($D_{Al}^{ol/L}$) increases with increasing pressure (Figure 3.1a), but the effect of temperature on $D_{Al}^{ol/L}$ is difficult to isolate because the experimental pressure generally increases with increasing temperature in these experiments. Because the pressure conditions of most published experimental results are at 100 kPa and 1 GPa, the effect of temperature on $D_{Al}^{ol/L}$ is studied at 100 kPa and 1 GPa (Figure 3.1b). These data show large scatter and no clear temperature dependence for $D_{Al}^{ol/L}$ is observed (Figure 3.1b). The scatter of the data is probably due to: 1) the effect of liquid composition on $D_{Al}^{ol/L}$, and 2) poor precision of Al_2O_3 analysis in olivine by electron microprobe under standard operating conditions. In most of the experimental results, Al_2O_3 content in olivine is less than 0.2%.

For the olivine/liquid partition coefficient for Cr_2O_3 ($D_{Cr}^{ol/L}$), the effect of pressure on $D_{Cr}^{ol/L}$ is difficult to isolate because most of the published data are from experiments at pressures less than 3 GPa and these data show large scatter on the P - $D_{Cr}^{ol/L}$ diagram (Figure 3.1c). The effect of temperature on $D_{Cr}^{ol/L}$ is studied at 100 kPa and 1 GPa which are the pressure conditions of most published experimental results (Figure 3.1d). At 100 kPa and 1 GPa, $D_{Cr}^{ol/L}$ generally decreases with increasing temperature (Figure 3.1d). The observed scatter is likely caused by the same reasons

stated above for $D_{Al}^{ol/L}$. In most of the experimental results, Cr_2O_3 content in olivine is less than 0.6wt%.

Due to the low precision of Al and Cr analyses in olivine in most studies, the published data do not fully constrain the effect of pressure and temperature on $D_{Al}^{ol/L}$ and $D_{Cr}^{ol/L}$. However, two experimental studies (Agee and Walker, 1990; Taura et al, 1998) with highly precise Al and Cr contents in olivine due to the special analytical condition exist and are investigated next.

The experimental studies of Agee and Walker (1990) and Taura et al (1998) show that over limited temperature ranges (1500-1700°C; 1700-1900°C), $D_{Al}^{ol/L}$ increases with increasing pressure (Figure 3.2a), and at 100 kPa and 2-4 GPa, $D_{Al}^{ol/L}$ increases with increasing temperature (Figure 3.2b). For the dependence of $D_{Cr}^{ol/L}$ on temperature, at 100 kPa, $D_{Cr}^{ol/L}$ decreases with increasing temperature (Figure 3.2d), but at higher pressures, the dependence $D_{Cr}^{ol/L}$ on temperature is less clear (Figure 3.2d). The effect of pressure on $D_{Cr}^{ol/L}$ is also not clear in these two studies. Over a temperature range of 1500-1700°C, $D_{Cr}^{ol/L}$ seems to increases with increasing pressure, but over a temperature range of 1700-1900°C, $D_{Cr}^{ol/L}$ decreases with increasing pressure (Figure 3.2c).

The temperature and pressure dependence of $D_{Al}^{ol/L}$ suggests that Al substitution into the olivine structure is sensitive to pressure and temperature (Taura et al, 1998). This allows for the possibility of developing a geothermometer based on Al partitioning between olivine and Al-rich minerals in mantle peridotites such as spinel. An investigation of the dependence of $D_{Al}^{ol/sp}$ on temperature based on a collection of previous experimental studies is carried out next. Despite the unknown dependence of $D_{Cr}^{ol/L}$ on pressure and temperature, similar investigation on $D_{Cr}^{ol/sp}$ is also carried out.

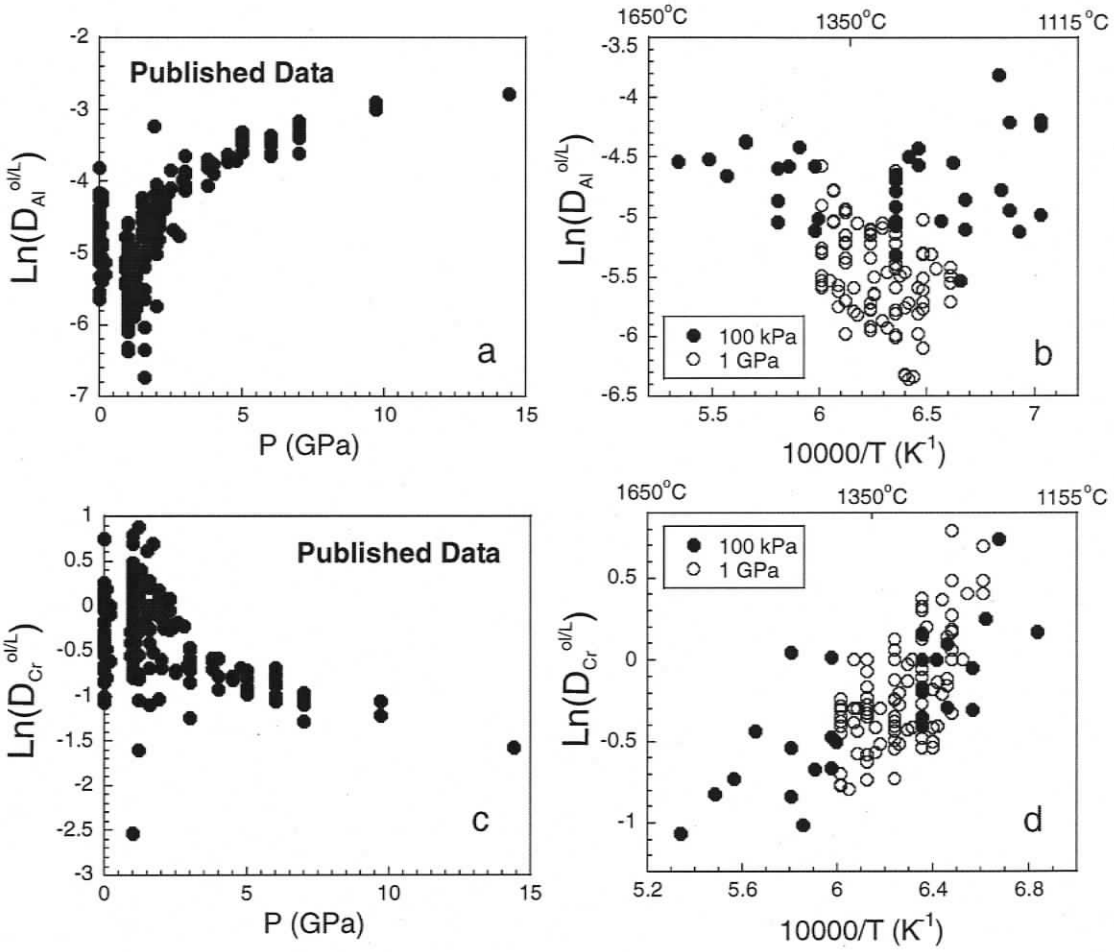

Figure 3.1 Compilation of published data showing the pressure dependence (a and c) and temperature dependence (b and d) of Al and Cr partitioning between olivine and melt. $D_{Al}^{ol/L}$: $[Al_2O_3]^{ol}/[Al_2O_3]^{L}$, where $[a]^{b}$ is the concentration of component a in phase b (wt%). ol: olivine. L: liquid. P: pressure. The SiO_2 content in the liquid ranges from 43wt% to 53wt%. The Mg/(Mg+Fe) of olivine ranges from 0.80 to 0.98. Data sources: Shimizu et al, 1982; Agee and Walker, 1990; Kinzler and Grove, 1992; Nielsen et al, 1992; Baker and Stolper, 1994; Beattie, 1994; Yang et al, 1996; Kinzler, 1997; Parman et al, 1997; Gaetani and Grove, 1998; Taura et al, 1998; Walter, 1998; Pickering-Witter and Johnston, 2000; Canil and Fedortchouk, 2001; Schwab and Johnston, 2001; Elkins-Tanton and Grove, 2003; Wasylenki et al, 2003; Laporte et al, 2004; Righter et al, 2004.

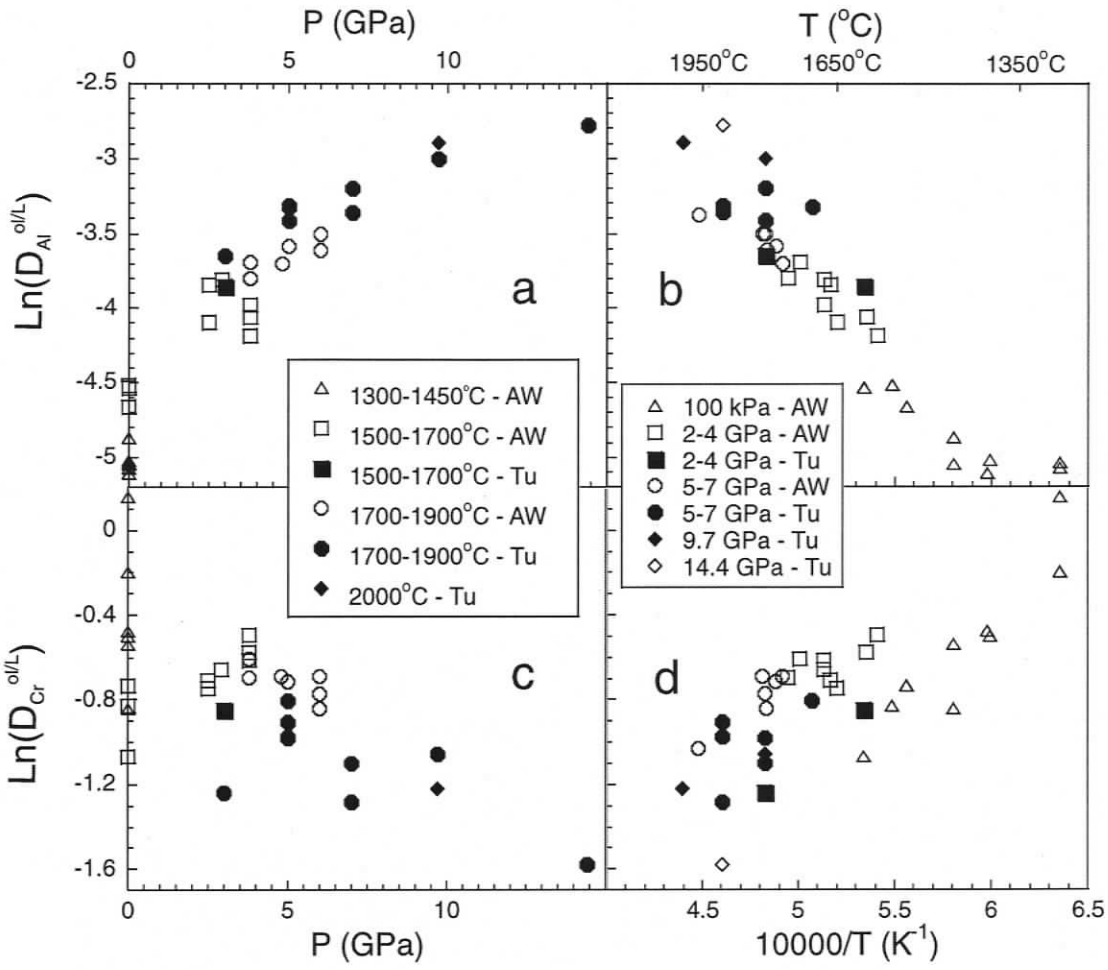

Figure 3.2 Temperature and pressure dependence of Al partitioning between olivine and melt based on the study of Agee and Walker (1990) and Taura et al (1998). AW: Agee and Walker, 1990. Tu: Taura et al, 1998. (a) and (b) shows that $D_{Al}^{ol/L}$ increases with increasing temperature at constant pressure, and increases with increasing pressure at constant temperature. (d) shows that $D_{Cr}^{ol/L}$ decreases with increasing temperature at 100 kPa.

3.2.2 Temperature dependence of Al and Cr partitioning between olivine and spinel

To investigate the temperature and pressure dependence of Al and Cr partitioning between olivine and spinel, published experimental results of mantle peridotite melting and two studies on natural mantle spinel peridotites, which are considered to represent equilibrium assemblages, were compiled. Most mantle peridotites contain olivine with Mg# (Mg/(Mg+Fe)) in the range from 0.80 to 0.96 (Gaul et al, 2000). Over 92% of the spinels in mantle peridotites contain TiO_2 < 2wt% (Figure 3.3a), and 82% of the spinels in mantle peridotites contain Fe^{3+}# less than 0.2 (Figure 3.3b). Thus, the compiled published results were screened using the following limits: 1) Fe^{3+}# of spinel of less than 0.2; 2) Mg# of olivine of 0.80 to 0.96; 3) TiO_2 contents in spinel of less than 2wt%. The pressure for spinel peridotite xenoliths was assumed to be 1.5 GPa and temperatures were calculated using the two pyroxene geothermometer calibrated by Brey and Köhler (1990).

The pressures for the published experimental data are in the range of 0.35-8 GPa but most data are within a narrow range (1.2-1.6 GPa), which is not sufficient to study the effect of pressure on $D_{Al}^{ol/sp}$ and $D_{Cr}^{ol/sp}$. The temperatures of published experimental results are 900-1500°C and these results are used to study the effect of temperature on $D_{Al}^{ol/sp}$ and $D_{Cr}^{ol/sp}$. Despite the unknown effect of pressure, the published results show a general increase in $D_{Al}^{ol/sp}$ and $D_{Cr}^{ol/sp}$ with increasing temperature (Figures 3.4a and 3.4b). This suggests that Al and Cr partitioning between olivine and spinel is dependent on temperature and may make potential thermometers. The scatter of the data in Figure 3.4 is caused by 1) poor precision of Al_2O_3 and Cr_2O_3 analysis in olivine by electron microprobe under standard operating conditions because of the low concentration of Al_2O_3 and Cr_2O_3 in olivine (< 0.2wt% and < 0.6wt%, respectively), and 2) the unknown effect of Cr# of spinel on $D_{Al}^{ol/sp}$ and $D_{Cr}^{ol/sp}$.

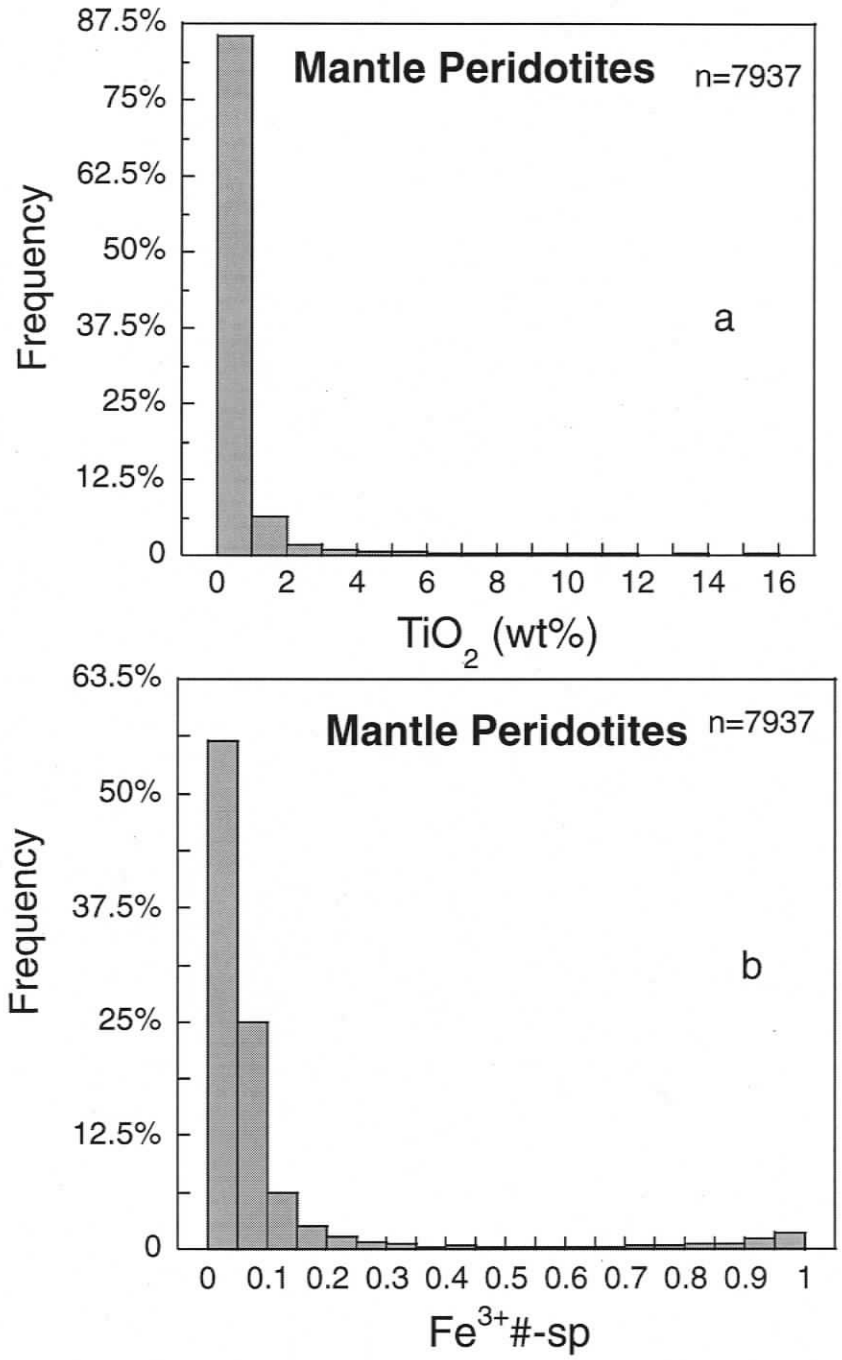

Figure 3.3 The content of TiO_2 (a) and Fe^{3+}# ($Fe^{3+}/(Fe^{3+}+Al+Cr)$) value (b) of spinels from global mantle samples. The total number (n) of analyses is 7937. As shown in these diagrams, over 92% of spinels have $TiO_2 < 2$wt% (a) and over 82% of the spinels from global mantle samples have $Fe^{3+}\# < 0.1$ (b). Data source: Barnes and Roeder, 2004.

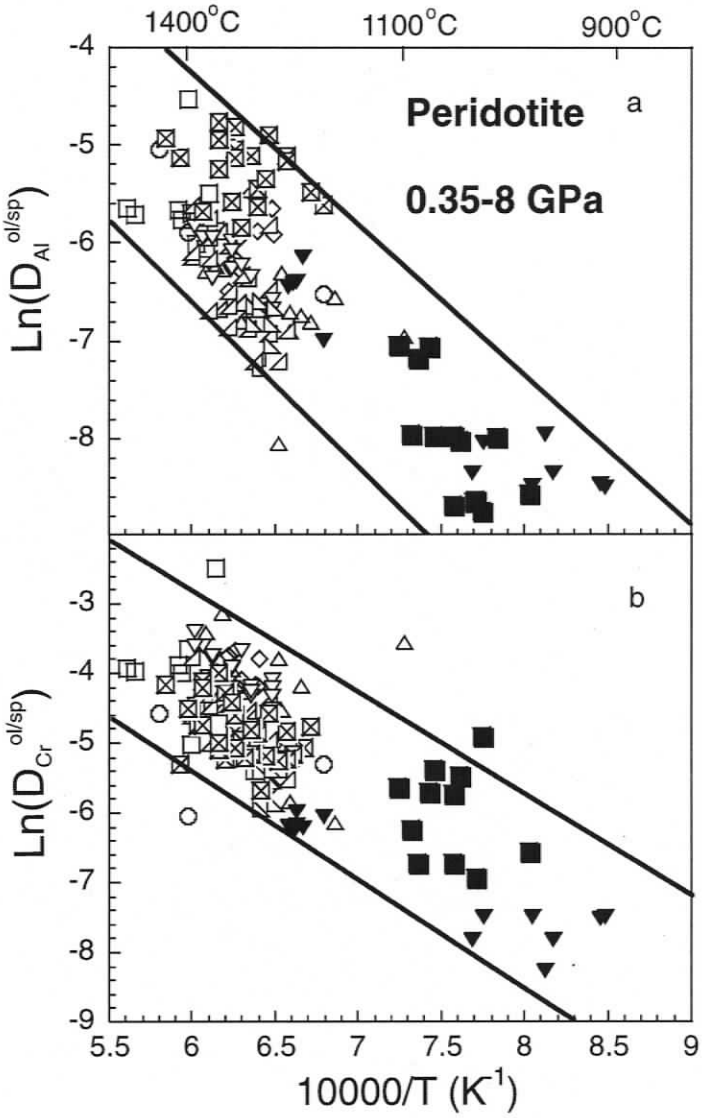

Figure 3.4 Compilation of published experimental results showing $D_{Al}^{ol/sp}$ and $D_{Cr}^{ol/sp}$ increase with increasing temperature. Solid lines are drawn by hand for boundaries of the data for references. Data are from experimental studies on mantle peridotite melting (open symbols) and two studies on mantle spinel peridotites (solid symbols) that are believed to represent equilibrium assemblages. Data sources: ○ Canil and Wei, 1990; □ Kinzler, 1997; △ Gaetani and Grove, 1998; ◇ Robinson et al, 1998; ▽ Pickering-Witter and Johnston, 2000; ◿ Schwab and Johnston, 2001; ☒ Bulatov et al, 2002; ▼ Witt-Eickschen and O'Neill, 2005; ■ Ying et al, 2006; ◺ Wasylenki et al, 2003.

3.3 Thermodynamic background

A preliminary thermodynamic model for Al exchange between olivine and spinel is developed in this section to better understand the Al partitioning between olivine and spinel. The exchange reaction describing the distribution of Al between olivine and spinel may be written as:

$$MgAl_2O_4 = MgAl_2O_4 \qquad (3.1)$$

spinel *olivine*

The condition of equilibrium of Reaction (3.1) is

$$\mu_{MgAl2O4}^{sp} = \mu_{MgAl2O4}^{ol} \qquad (3.2)$$

where μ_a^b is the chemical potential of component a in phase b. μ can be expressed as

$$\mu = \mu^0 + RTln\alpha \qquad (3.3)$$

where μ^0 is the standard state chemical potential of a phase, R is the gas constant and $R = 8.31\ JK^{-1}mol^{-1}$, $T\ (K)$ is the absolute temperature, and α is the activity of the component.

Because of the low concentration of Al in olivine, the $MgAl_2O_4$ component in olivine can be expected to obey Henry's Law. Thus,

$$\alpha_{MgAl2O4}^{ol} = k*[MgAl_2O_4]^{ol} \qquad (3.4)$$

where k is the Henry's Law constant and $[MgAl_2O_4]^{ol}$ is the concentration of $MgAl_2O_4$ in olivine. Assuming that all Al in olivine is as the $MgAl_2O_4$ component, the concentration of $MgAl_2O_4$ in olivine is proportional to the concentration of Al_2O_3 in olivine. Thus, Equation (3.4) can be written as

$$\alpha_{MgAl2O4}^{ol} = k'*[Al_2O_3]^{ol} \qquad (3.5)$$

where k' is a constant and $k' = k*(MW_{MgAl2O4}/MW_{Al2O3})$. MW represents Molecular Weight.

Thus, according to Equation (3.3), the following equation is derived:

$$\mu_{MgAl2O4}^{ol} = \mu^{0}_{MgAl2O4}{}^{ol} + RTln(k'*[Al_2O_3]^{ol}) \quad (3.6)$$

Assuming that the mixing of Mg and Fe is ideal (Oak et al, 1984), spinel can be considered as a solid solution between $MgAl_2O_4$ and $MgCr_2O_4$. Assuming that this binary solid solution can be treated in terms of the asymmetric Margules relation (Oak et al, 1984), which suggests that the activity coefficient of $MgAl_2O_4$ in spinel is dependent on Al and Cr contents in spinel and the asymmetric Margules mixing parameters $W_{MgAl2O4}$ and $W_{MgCr2O4}$ (Mukhopadhyay et al, 1993), the chemical potential of $MgAl_2O_4$ in spinel can be expressed by the following equation:

$$\begin{aligned}
\mu_{MgAl2O4}^{sp} &= \mu^{0}_{MgAl2O4}{}^{sp} + RTln(\alpha_{MgAl2O4}{}^{sp}) \\
&= \mu^{0}_{MgAl2O4}{}^{sp} + RTln(\gamma[MgAl_2O_4]^{sp}) \\
&= \mu^{0}_{MgAl2O4}{}^{sp} + RTln([MgAl_2O_4]^{sp}) + RTln\gamma \\
&= \mu^{0}_{MgAl2O4}{}^{sp} + RTln([MgAl_2O_4]^{sp}) + 2X_{Al}X_{Cr}W_{MgAl2O4} + (X_{Cr})^2W_{MgCr2O4} - \\
&\quad 2X_{Al}X_{Cr}(X_{Cr}W_{MgCr2O4}+X_{Al}W_{MgAl2O4}) \\
&= \mu^{0}_{MgAl2O4}{}^{sp} + RTln([Al_2O_3]^{sp}*(MW_{MgAl2O4}/MW_{Al2O3})) + 2X_{Al}X_{Cr}W_{MgAl2O4} + \\
&\quad (X_{Cr})^2W_{MgCr2O4} - 2X_{Al}X_{Cr}(X_{Cr}W_{MgCr2O4}+X_{Al}W_{MgAl2O4}) \quad (3.7)
\end{aligned}$$

where $X_{Al} = Al/(Al+Cr)$, $X_{Cr} = Cr/(Al+Cr)$, $[a]^{sp}$ is the concentration of component a in spinel, γ is the activity coefficient, and W_a is the asymmetric Margules mixing parameter for the component a in spinel. Defining $m = MW_{MgAl2O4}/MW_{Al2O3}$ and substituting $X_{Al} = 1 - X_{Cr}$ into Equation (3.7), Equation (3.7) can be written as:

$$\begin{aligned}
\mu_{MgAl2O4}^{sp} &= \mu_{MgAl2O4}^{sp0} + RTln([Al_2O_3]^{sp}) + RTln(m) + 4X_{Cr}W_{MgAl2O4} - \\
&\quad X_{Cr}^2(6W_{MgAl2O4} - W_{MgCr2O4}) + 2X_{Cr}^3(W_{MgAl2O4} - W_{MgCr2O4}) \quad (3.8)
\end{aligned}$$

Substituting Equations (3.6) and (3.8) into Equation (3.2), the following equation is derived:

$$\mu^0_{MgAl2O4}{}^{ol} + RTln(k'*[Al_2O_3]^{ol}) = \mu^0_{MgAl2O4}{}^{sp} + RTln([Al_2O_3]^{sp}) + RTln(m) + 4X_{Cr}W_{MgAl2O4} - X_{Cr}{}^2(6W_{MgAl2O4} - W_{MgCr2O4}) + 2X_{Cr}{}^3(W_{MgAl2O4} - W_{MgCr2O4}) \quad (3.9)$$

Thus,

$$RTln(D_{Al}{}^{ol/sp}) = RTln([Al_2O_3]^{ol}/[Al_2O_3]^{sp}) = \mu^0_{MgAl2O4}{}^{sp} - \mu^0_{MgAl2O4}{}^{ol} + RTln(m/k') + 4X_{Cr}W_{MgAl2O4} - X_{Cr}{}^2(6W_{MgAl2O4} - W_{MgCr2O4}) + 2X_{Cr}{}^3(W_{MgAl2O4} - W_{MgCr2O4}) \quad (3.10)$$

Since $\mu^0_{MgAl2O4}{}^{sp}$, $\mu^0_{MgAl2O4}{}^{ol}$, *and* m/k' are all constant, Equation (3.10) can be written as

$$RTln(D_{Al}{}^{ol/sp}) = M + K_1X_{Cr} + K_2X_{Cr}{}^2 + K_3X_{Cr}{}^3 \quad (3.11)$$

where $M = \mu^0_{MgAl2O4}{}^{sp} - \mu^0_{MgAl2O4}{}^{ol} + RTln(m/k')$, $K_1 = 4W_{MgAl2O4}$, $K_2 = -6W_{MgAl2O4} + W_{MgCr2O4}$, and $K_3 = 2(W_{MgAl2O4} - W_{MgCr2O4})$.

Equation (3.11) suggests that at constant temperature, $\ln(D_{Al}{}^{ol/sp})$ has a polynominal relation with X_{Cr}, and at constant X_{Cr}, $\ln(D_{Al}{}^{ol/sp})$ has a linear relationship with inverse temperature. However, the values of the interaction parameters in Equation (3.11) are not well known, and spinels include not only Al and Cr, but also Fe^{3+}, Ti, V, etc. Thus, Equation (3.11) cannot be treated as a completely accurate relationship between $D_{Al}{}^{ol/sp}$ and X_{Cr} and temperature, but is useful as a guide to the calibration of the thermometer. Equation (3.11) suggests that the relationship between X_{Cr} and $\ln(D_{Al}{}^{ol/sp})$ should be investigated at constant temperature and should be expected to be polynominal, the relationship between inverse temperature and $\ln(D_{Al}{}^{ol/sp})$ should be investigated at

constant X_{Cr} and be expected to be linear, and combination of the two relations will make a thermometer.

The oxygen fugacity in the spinel lherzolite phases of the upper mantle varies from QFM – 2 to QFM + 4 (e.g. Ionov and Wood, 1992; Woodland et al, 1992; Canil et al, 1994). At these oxygen fugacity conditions, Cr^{2+} and Cr^{3+} coexist in olivine (Hanson and Jones, 1998). This makes the partitioning of Cr between olivine and spinel complicated. No thermodynamic investigation on this subject was performed.

3.4 Experimental approach

3.4.1. Introduction

The main purpose of this experimental study is to quantify the effect of temperature and Cr# of spinel on Al and Cr partitioning between olivine and spinel at 100 kPa. The stability of spinel is strongly dependent on the Cr_2O_3 and Al_2O_3 concentrations of the parent magma (Roeder and Reynolds, 1991). Thus, a powdered pillow basalt (MIC-99-13) from southern Vancouver Island, British Columbia (Timpa et al, 2005; Table 3.1) doped with different amounts of spinel ($MgAl_2O_4$) and chromite ($FeCr_2O_4$) components was first tested as the starting material. Only those conditions that saturated with spinel crystals larger than 2 μm in diameters were chosen for further experiments.

In the experiments, different amounts of Fo_{90} ($(Mg_{0.9}Fe_{0.1})_2SiO_4$) and MgO components were added to the basalt starting material to vary the temperature range over which olivine and spinel co-crystallize. The MgO/FeO ratios in the starting materials were kept constant to ensure the growth of olivine with approximately constant Mg#. The Cr#-sp (Cr# of spinel) was varied by changing the Cr_2O_3/Al_2O_3 ratio in the starting

material while keeping other experimental parameters (e.g. fO_2, temperature, FeO/MgO of the starting material) constant. The compositions of starting materials and experimental products were analyzed by electron microprobe (see Section 3.4.4).

3.4.2. Starting materials

The Fo_{90}, spinel and chromite components that were used to make the starting composition were mixtures of reagent grade oxides at the same ratio as that for the oxide compositions of $(Mg_{0.9}Fe_{0.1})_2SiO_4$, $MgAl_2O_4$ and $FeCr_2O_4$. The procedures for making the Fo_{90}, spinel and chromite components were as follows: reagent grade oxides were dried at 120°C for at least 24 hours, weighed, and well mixed by being shaken in a plastic bottle for about 30 minutes. The compositions for the basalt MIC-99-13, spinel component, and chromite component are shown in Table 3.1. The spinel component, chromite component, and basalt MIC-99-13 were weighed in different ratios and transferred into an agate mortar. Each mixture was ground under alcohol, dried, fused in a platinum (Pt) crucible for 24 hours at 1500°C in a box furnace at 100 kPa and quenched in water. Pieces of quenched glass were mounted in oil and examined under transmitted light to ensure that no chromite crystals had grown. Crystal-free quenched glass was then extracted from the crucible. Large chips of the fused starting glasses were mounted in epoxy, polished, and analyzed by EMP for major and minor elements (Table 3.2). The rest of the glass was crushed and ground under alcohol in an agate mortar to a grain size of less than 100 μm. The ground glass starting materials were diluted into a slurry with alcohol, then loaded on loops of 0.15 mm diameter Pt wire and after drying, were sintered using a torch for further experiments.

Table 3.1 Compositions (wt%) of basalt MIC-99-13, spinel component, and Fo_{90} component used to make the starting material.

Component	MIC-99-13	Fo_{90}	Chromite	Spinel
Description	Pillow Basalt	$(Mg_{0.9}Fe_{0.1})_2SiO_4$	$FeCr_2O_4$	$MgAl_2O_4$
SiO_2	49.53	40.87		
TiO_2	1.28			
Al_2O_3	14.23			71.66
FeO*	12.45	9.77	32.10	
MnO	0.18			
MgO	7.83	49.35		28.34
CaO	12.40			
Na_2O	1.93			
K_2O	0.05			
P_2O_5	0.10			
Cr_2O_3			67.90	
total	99.99	100	100	100

* represents total Fe as FeO.

Table 3.2 Starting compositions for experiments (wt%).

Oxide	1Cr	2Cr	3.5Cr	1Cr'	2Cr'	1Cr'+ 1Cr	2Cr'+ 1Cr	0.5Cr +5sp	1Cr+ 2sp	1Cr+ 4sp
SiO_2	45.70	45.94	44.12	40.53	44.63	40.74	44.55	40.84	42.39	41.60
TiO_2	0.96	0.96	0.77	1.07	0.81	1.08	0.83	1.09	1.13	1.11
Al_2O_3	11.05	10.95	10.56	11.65	9.65	11.39	9.58	15.41	13.68	14.90
*FeO	11.82	11.92	11.57	11.00	11.85	11.25	12.17	10.63	11.23	11.07
MnO	0.12	0.13	0.10	0.18	0.13	0.14	0.10	0.15	0.16	0.17
MgO	18.39	18.55	23.00	22.75	22.71	22.53	22.45	18.84	17.48	17.75
CaO	8.85	8.77	7.49	10.04	7.63	10.03	7.60	10.05	10.49	10.30
Na_2O	1.32	1.31	1.10	1.38	1.10	1.29	0.99	1.48	1.43	1.42
K_2O	0.06	0.05	0.04	0.04	0.04	0.03	0.04	0.05	0.05	0.05
P_2O_5	0.11	0.11	0.07	0.10	0.10	0.11	0.11	0.11	0.09	0.12
Cr_2O_3	0.45	0.43	0.33	0.27	0.31	0.35	0.52	0.15	0.35	0.26
V_2O_3	0.03	0.03	0.04	0.03	0.02	0.03	0.03	0.05	0.05	0.07
NiO	0.00	0.03	0.02	0.01	0.03	0.02	0.01	0.01	0.03	0.03
total	98.86	99.18	99.21	99.05	99.01	98.99	98.98	98.86	98.56	98.85

* represents total Fe as FeO

The contents of the basalt MIC-99-13, Fo_{90} component, MgO component, spinel component, and chromite component in each starting material are as follows:

1Cr: 89% MIC-99-13 + 1% chromite + 10% MgO

2Cr: 73% MIC-99-13 + 1% chromite + 25% Fo_{90} + 1% spinel

3.5Cr: 61.5% MIC-99-13 + 1% chromite + 35% Fo_{90} + 2.5% spinel

1Cr': 83% MIC-99-13 + 1% chromite + 16% MgO

2Cr': 63% MIC-99-13 + 1% chromite + 35% Fo_{90} + 1% spinel

1Cr'+1Cr: 82% MIC-99-13 + 2% chromite + 16% MgO

2Cr'+1Cr: 62% MIC-99-13 + 2% chromite + 35% Fo_{90} + 2.5% spinel

0.5Cr+5sp: 83.5% MIC-99-13 + 0.5% chromite + 11% MgO + 5% spinel

1Cr+2sp: 87% MIC-99-13 + 1% chromite + 10% MgO + 2% spinel

1Cr+4sp: 85% MIC-99-13 + 1% chromite + 10% MgO + 4% spinel

3.4.3. Experimental conditions

All experiments were performed in a vertical tube gas mixing furnace at 100 kPa and at temperature of 1200-1450°C (Table 3.3). The fO_2 condition for most experiments was 1.8 log units below the QFM buffer. Additionally, a series of experiments were performed 3.5-5 log units above the QFM buffer (Table 3.3). For each experiment, a sample of the same starting composition was run at the same temperature and fO_2 for 24 hours to pre-saturate the Pt loops with Fe to avoid Fe-loss to the Pt wire. When pre-saturation was complete, the glass bead was dissolved in HF and a new slurry was sintered to the Fe pre-saturated Pt loop and run at the same T - fO_2 conditions for the final experiment. Temperatures were measured with a Pt - $Pt_{90}Rh_{10}$ thermocouple calibrated to the melting point of gold. Oxygen fugacity was controlled by CO - CO_2 gas mixing with a total flow of 100 standard cubic centimetres per minute (sccm) and measured in each experiment with a solid zirconia electrolyte cell. Run durations varied from 24 hours at 1300-1450°C, 96 hours at 1250°C, to 120 hours at 1200°C. At the end of each experiment, the samples were quickly pulled out of the furnace and quenched to a glass within seconds in a stream of air. Run products were mounted in epoxy and polished for analysis by electron microprobe (EMP).

Table 3.3 Experimental run conditions and phase assemblages

Run#	Starting Material	T(°C)	Duration (h)	Log(fO_2) (bars)	ΔQFM	phases
w21-1	1Cr	1200	120	-3.2	5	sp, ol, L
w21-2	2Cr	1200	120	-3.2	5	sp, ol, L
w17-1	1Cr	1300	48	-3.2	3.9	sp, ol, L
w17-2	2Cr	1300	48	-3.2	3.9	sp, ol, L
w19-1	1Cr	1300	24	-3.2	3.9	sp, ol, L
w19-2	2Cr	1300	24	-3.2	3.9	sp, ol, L
w20-1	1Cr	1350	48	-3.2	3.5	sp, ol, L
w20-2	2Cr	1350	48	-3.2	3.5	sp, ol, L
w40-1	1Cr	1200	142	-9.8	-1.6	sp, ol, pl, L
w40-2	2Cr	1200	142	-9.8	-1.6	sp, ol, pl, L
w39-1	1Cr	1250	96	-9.6	-1.9	sp, ol, L
w39-2	2Cr	1250	96	-9.6	-1.9	sp, ol, L
w35-1	1Cr	1300	24	-9	-1.8	sp, ol, L
w35-2	2Cr	1300	24	-9	-1.8	sp, ol, L
w36-1	1Cr	1350	24	-8.4	-1.7	sp, ol, L
w36-2	2Cr	1350	24	-8.4	-1.7	sp, ol, L
w55-1	1Cr'	1350	48	-8.4	-1.7	sp, ol, L
w55-2	2Cr'	1350	48	-8.4	-1.7	sp, ol, L
w55-3	3.5Cr	1350	48	-8.4	-1.7	sp, ol, L
w62-1	1Cr'+1Cr	1350	24	-8.4	-1.7	sp, ol, L
w62-2	2Cr'+1Cr	1350	24	-8.4	-1.7	sp, ol, L
w66-1	0.5Cr+5Sp	1350	48	-8.4	-1.7	sp, ol, L
w66-3	1Cr+4Sp	1350	48	-8.4	-1.7	sp, ol, L
w61-1	1Cr'+1Cr	1400	24	-7.9	-1.6	sp, ol, L
w61-2	2Cr'+1Cr	1400	24	-7.9	-1.6	sp, ol, L
w60-1	1Cr'+1Cr	1450	24	-7.4	-1.7	sp, ol, L
w60-2	2Cr'+1Cr	1450	24	-7.4	-1.6	sp, ol, L

Sp: spinel; ol: olivine; L: liquid; pl: plagioclase; h: hour; ΔQFM: the difference between log(fO_2) of the experiments and log(fO_2) of the Quartz-Fayalite-Magnetite oxygen fugacity buffer at the same temperature and pressure conditions.

3.4.4. Analytical methods

Run products were analyzed using a CAMECA SX50 EMP at the University of British Columbia. Major and minor elements for spinels were determined at a 15.0 kV acceleration voltage using a beam current of 20.1 nA with a 1 μm beam. Major and minor elements for olivine and spinel were determined at a 15.0 kV acceleration voltage and a beam current of 39.8 nA with a 1-2 μm beam. Major and minor elements for glasses were determined using a 15.0 kV acceleration voltage and a beam current of 20.1 nA with a 5 μm beam. Analytical conditions were 20 s counting time on peak and background for all major elements except for Al (60 s) and Cr (60 s) in olivine. Natural and synthetic minerals were used for calibration. In each run product, about five analysis points were measured for spinels, ten analysis points were measured for olivines, and five analysis points were measured for glass. The core and rim of the olivine were analyzed. The core and rim of the spinel were analyzed if the spinel grain was large enough; otherwise, only one analysis was carried out on each spinel grain. San Carlos olivine with known Al content based on solution ICPMS (Chapter 4) was analyzed during each analytical session to ensure the accuracy of the electron microprobe data and the consistency of the data between each run. The Al content of San Carlos olivine based on solution ICPMS is 99±15 ppm, which is very close to the EMP results for Al content in San Carlos olivine from the three analytical sessions: 104±14 ppm, 107±14 ppm, and 93±22 ppm (the concentration is the average of the analyses and the analytical precision is represented by one standard deviation of the analyses). Major element contents of San Carlos olivine from three runs are within 1-1.8% of each other (Table 3.4). The Cr_2O_3 contents of San Carlos olivine from three runs are within 20% of each other (Table 3.4).

Table 3.4 Major and minor element concentrations (wt%) of San Carlos olivine obtained from three analytical sessions by electron microprobe.

Label	May		July		Sep	
n	2		5		15	
	ave	1σ	ave	1σ	ave	1σ
MgO	47.2	0.1	47.3	0.1	47.7	0.1
Al_2O_3	0.02	0.00	0.02	0.00	0.02	0.00
SiO_2	40.5	0.0	39.9	0.1	40.5	0.1
CaO	0.08	0.01	0.07	0.01	0.07	0.01
Cr_2O_3	0.01	0.01	0.01	0.02	0.01	0.01
MnO	0.16	0.01	0.15	0.02	0.15	0.02
*FeO	11.1	0.0	11.3	0.1	11.1	0.1
NiO	0.39	0.01	0.37	0.03	0.38	0.03
total	99.50		99.13			99.93

May, July, and Sep indicate the date of each analysis session. "n" represents the number of analysis in each session. * represents total Fe as FeO. "ave" represents the average of the analysis and "1σ" represents the one standard deviation of the analysis.

3.5 Experimental results

3.5.1 Olivine and spinel compositions

Olivine ranges in size from 5 μm to 180 μm in diameter. Spinel in the experimental results ranges in size from 1 μm to 18 μm in diameter. The major and minor element concentrations for each phase in each run product are shown in Table 3.5.

The Mg# of olivine ranges from 0.87 to 0.97. At $\log(fO_2)$ = QFM + 3.5 to QFM + 5, the Mg# of olivine ranges from 0.96 to 0.97 and at $\log(fO_2)$ = QFM – 1.8, the Mg# of olivine ranges from 0.87 to 0.93 which is close in composition to mantle olivine (Gaul et al, 2000). The Fe^{3+} contents of spinel were calculated assuming perfect stoichiometry (Droop, 1987). At $\log(fO_2)$ = QFM – 1.8, the Fe^{3+}# of spinel ranges from 0.02 to 0.05, and Cr# in spinel ranges from 0.07 to 0.63. At $\log(fO_2)$ = QFM + 3.5-5, the Fe^{3+}# of spinel is extremely high (0.62-0.79) compared to the Fe^{3+}# of most spinel from the upper mantle (Figure 3.3b), and Cr# in spinel ranges from 0.03 to 0.18.

3.4.2 Attainment of equilibrium

Since all experiments reported here are synthesis experiments, it is important to assess whether equilibrium compositions were produced. Equilibrium partitioning of Al and Cr between olivine and spinel in the experiments is supported by several observations. Firstly, the core and rim of the olivine and spinels were analyzed if the grains were large enough (> 4 μm) for each experiment and the difference between the core and rim compositions are always found to be within analytical precision. Secondly, time series experiments demonstrate no change in olivine and spinel compositions between 24 hour and 48 hour experiments at 1300°C (Figure 3.5a,b,c,d), suggesting that a close approach to equilibrium is attained in 24 hours.

Table 3.5 Major and minor element concentrations (wt%) determined by EMP in the experimental results.

Run	ΔQFM	T(°C)	ph	n	MgO	1σ	Al_2O_3	1σ	SiO_2	1σ	CaO	1σ	V_2O_3	1σ	Cr_2O_3	1σ	MnO	1σ	FeO	1σ	NiO	1σ	TiO_2	1σ	Na_2O	1σ	K_2O	1σ	SUM
w21-1	3.9	1200	ol	8	54.9	0.18	0.05	0.00	42.1	0.19	0.24	0.01	0.00	0.00	0.01	0.01	0.20	0.02	2.66	0.09	0.02	0.02							100.19
			sp	4	17.0	0.06	8.71	0.11	0.15	0.03	0.30	0.03	0.00	0.00	2.52	0.11	0.38	0.01	63.5	0.18	0.05	0.01	1.35	0.02					93.92
w21-2	3.9	1200	ol	7	54.9	0.21	0.05	0.01	42.0	0.24	0.25	0.01	0.01	0.01	0.03	0.01	0.14	0.01	2.69	0.12	0.03	0.02							100.14
			sp	2	17.1	0.03	9.3	0.10	0.10	0.01	0.16	0.03	0.00	0.00	4.86	0.24	0.24	0.01	61.7	0.43	0.07	0.02	0.77	0.02					94.32
w17-1	3.9	1300	ol	10	54.3	0.13	0.10	0.01	42.0	0.11	0.31	0.01	0.01	0.01	0.03	0.01	0.15	0.03	3.16	0.08	0.04	0.01							100.1
			sp	5	18.7	0.17	16.2	0.09	0.15	0.01	0.22	0.04	0.00	0.00	6.11	0.32	0.21	0.05	52.5	0.07	0.09	0.04	0.69	0.01					94.80
w17-2	3.9	1300	ol	9	54.2	0.10	0.08	0.01	41.9	0.08	0.20	0.01	0.01	0.01	0.03	0.02	0.11	0.01	3.57	0.05	0.03	0.02							100.10
			sp	5	17.1	0.12	11.2	0.16	0.13	0.01	0.15	0.06	0.00	0.00	9.10	0.38	0.18	0.02	56.1	0.49	0.06	0.03	0.59	0.04					94.65
w19-1	3.9	1300	ol	11	54.3	0.21	0.10	0.01	41.9	0.11	0.31	0.01	0.00	0.01	0.03	0.02	0.13	0.02	3.27	0.05	0.04	0.02							100.13
			sp	5	18.5	0.05	16.2	0.13	0.14	0.02	0.21	0.03	0.00	0.00	6.10	0.28	0.22	0.02	52.5	0.50	0.07	0.03	0.73	0.04					94.62
w19-2	3.9	1300	ol	9	54.0	0.24	0.08	0.01	41.8	0.32	0.22	0.01	0.01	0.01	0.04	0.01	0.11	0.02	3.74	0.04	0.02	0.02							100.01
			sp	2	17.3	0.18	11.9	0.07	0.42	0.31	0.20	0.03	0.00	0.00	8.77	0.18	0.16	0.02	55.2	1.07	0.01	0.01	0.61	0.05					94.58
w20-1	3.9	1350	ol	8	53.8	0.09	0.12	0.00	41.8	0.09	0.28	0.01	0.01	0.01	0.03	0.01	0.12	0.02	3.61	0.08	0.04	0.03							99.77
			sp	5	18.2	1.03	15.9	4.04	0.22	0.05	0.13	0.10	0.01	0.01	10.0	0.49	0.15	0.02	49.0	5.18	0.06	0.04	0.61	0.03					94.32
w20-2	3.9	1350	ol	9	53.5	0.13	0.09	0.01	41.8	0.10	0.21	0.01	0.01	0.01	0.04	0.01	0.10	0.02	3.98	0.05	0.04	0.02							99.78
			sp	4	17.2	0.07	12.7	0.08	0.14	0.03	0.09	0.04	0.00	0.00	14.0	0.37	0.11	0.02	49.6	0.28	0.05	0.02	0.56	0.02					94.48
w40-1	-1.6	1200	ol	6	42.3	0.20	0.05	0.00	38.8	0.13	0.52	0.05			0.09	0.02	0.26	0.02	17.1	0.08	0.10	0.01							99.26
			L	5	8.6	0.05	13.1	0.05	47.2	0.11	13.9	0.15			0.10	0.04	0.20	0.03	12.0	0.17			2.51	0.05	1.07	0.02	0.07	0.02	98.73
w40-2	-1.6	1200	ol	3	44.7	0.08	0.05	0.01	39.4	0.04	0.39	0.04			0.12	0.02	0.19	0.03	14.6	0.14	0.13	0.01							99.55
			L	5	8.6	0.03	14.1	0.07	50.9	0.09	12.4	0.03			0.10	0.02	0.14	0.03	9.38	0.14			1.61	0.02	1.46	0.05	0.07	0.01	98.74
w39-1	-1.9	1250	ol	8	47.0	0.32	0.08	0.02	40.1	0.14	0.42	0.01			0.10	0.01	0.19	0.03	11.6	0.19	0.07	0.01							99.52
			L	5	10.5	0.16	16.1	0.08	47.1	0.14	14.0	0.11			0.09	0.02	0.18	0.02	8.67	0.14			1.51	0.03	0.89	0.04	0.04	0.02	99.00
w39-2	-1.9	1250	ol	10	46.8	0.17	0.06	0.01	40.0	0.12	0.33	0.01			0.12	0.02	0.14	0.02	11.9	0.21	0.08	0.02							99.42
			sp	1	15.4	0.00	26.2	0.00	0.13	0.00	0.22	0.00	0.68	0.00	39.6	0.00	0.09	0.00	15.6	0.00	0.01	0.00	0.75	0.00					98.71
			L	5	10.6	0.12	14.7	0.15	50.2	0.29	12.0	0.09			0.12	0.02	0.13	0.03	8.93	0.10			1.30	0.03	1.08	0.04	0.06	0.01	99.18
w35-1	-1.8	1300	ol	7	47.3	0.17	0.09	0.02	40.2	0.15	0.45	0.01			0.10	0.01	0.18	0.02	11.5	0.19	0.03	0.02							99.81
			L	5	12.1	0.95	14.6	0.43	46.4	0.32	13.1	0.25			0.15	0.02	0.18	0.02	10.1	0.32			1.40	0.06	1.09	0.06	0.05	0.01	99.20

ph: phase; ol: olivine; sp: spinel; L: liquid; n: number of analyses; 1σ: one standard deviation.

Table 3.5 (continued) Major and minor element concentrations (wt%) determined by EMP in the experimental results.

Run	ΔQFM	T(°C)	ph	n	MgO	1σ	Al_2O_3	1σ	SiO_2	1σ	CaO	1σ	V_2O_3	1σ	Cr_2O_3	1σ	MnO	1σ	FeO	1σ	NiO	1σ	TiO_2	1σ	Na_2O	1σ	K_2O	1σ	SUM
w35-2	-1.8	1300	ol	9	46.7	0.23	0.06	0.00	39.9	0.14	0.34	0.01			0.15	0.01	0.13	0.02	12.2	0.13	0.03	0.02							99.58
			sp	2	15.3	0.08	25.0	0.19	0.20	0.05	0.29	0.02	0.52	0.10	40.7	0.69	0.07	0.06	15.5	0.15	0.02	0.02	0.95	0.20					98.53
			L	5	12.2	0.11	14.1	0.05	48.7	0.18	11.2	0.05			0.14	0.04	0.12	0.01	10.4	0.16			1.24	0.02	1.19	0.02	0.07	0.01	99.44
w36-1	-1.7	1350	ol	9	48.6	0.16	0.10	0.01	40.4	0.14	0.40	0.02			0.15	0.01	0.14	0.01	9.75	0.10	0.02	0.02							99.62
			sp	4	18.2	0.09	32.1	1.16	0.17	0.02	0.25	0.02	0.43	0.04	35.6	1.23	0.03	0.04	12.1	0.17	0.01	0.01	0.65	0.01					99.53
			L	5	14.9	0.24	13.9	0.11	45.6	0.12	12.1	0.14			0.20	0.04	0.17	0.05	10.5	0.26			1.28	0.02	0.57	0.02	0.03	0.01	99.25
w36-2	-1.7	1350	ol	10	48.2	0.15	0.07	0.01	40.4	0.14	0.28	0.02			0.18	0.02	0.12	0.02	10.4	0.13	0.01	0.02							99.68
			sp	3	16.0	0.13	22.1	0.51	0.14	0.01	0.19	0.04	0.43	0.01	45.6	1.05	0.03	0.03	13.8	0.22	0.01	0.01	0.64	0.02					98.90
			L	5	15.1	0.11	12.9	0.10	48.3	0.18	10.4	0.06			0.27	0.05	0.12	0.03	10.4	0.23			1.13	0.03	0.67	0.03	0.05	0.00	99.36
w55-1	-1.7	1350	ol	11	49.7	0.14	0.12	0.00	41.1	0.06	0.45	0.02			0.10	0.01	0.14	0.02	8.18	0.13	0.01	0.01							99.77
			sp	6	21.5	0.20	47.9	1.29	0.18	0.03	0.18	0.01	0.39	0.02	20.0	1.39	0.05	0.04	8.86	0.18	0.02	0.02	0.40	0.02					99.51
			L	5	15.3	0.27	15.4	0.10	43.5	0.14	13.8	0.15			0.13	0.01	0.18	0.03	9.07	0.09			1.48	0.04	0.12	0.01	0.01	0.01	98.98
w55-2	-1.7	1350	ol	10	48.8	0.19	0.08	0.01	40.9	0.12	0.27	0.03			0.20	0.02	0.11	0.02	9.51	0.13	0.01	0.01							99.87
			sp	5	16.3	0.17	22.0	1.01	0.11	0.02	0.08	0.03	0.41	0.04	46.7	1.17	0.01	0.02	13.3	0.20	0.02	0.01	0.69	0.07					99.55
			L	5	15.7	0.04	12.9	0.07	48.4	0.11	10.2	0.08			0.29	0.02	0.14	0.01	10.2	0.27			1.11	0.03	0.32	0.01	0.03	0.01	99.18
w55-3	-1.7	1350	ol	12	49.1	0.07	0.09	0.01	40.8	0.10	0.26	0.03			0.18	0.01	0.10	0.01	9.05	0.07	0.01	0.01							99.61
			sp	5	17.7	0.17	28.6	0.49	0.13	0.02	0.15	0.04	0.35	0.03	40.4	0.67	0.02	0.02	11.7	0.21	0.01	0.01	0.55	0.02					99.63
			L	5	16.2	0.08	13.8	0.09	47.4	0.14	10.0	0.08			0.25	0.03	0.11	0.01	10.2	0.17			1.04	0.01	0.27	0.02	0.02	0.01	99.31
w62-1	-1.7	1350	ol	12	48.95	0.15	0.12	0.01	40.87	0.11	0.49	0.02		0.00	0.11	0.01	0.14	0.01	9.07	0.09	0.01	0.01		0.00					99.75
			sp	4	20.51	0.05	43.18	0.77	0.19	0.06	0.18	0.02	0.19	0.04	23.99	0.79	0.04	0.03	10.73	0.34	0.00	0.00	0.72	0.21					99.72
			L	5	14.91	0.57	14.59	0.18	43.21	0.17	13.63	0.22			0.12	0.04	0.19	0.02	10.40	0.22			1.47	0.02	0.22	0.02	0.01	0.01	98.77
w62-2	-1.7	1350	ol	11	48.51	0.12	0.08	0.01	40.77	0.12	0.28	0.02		0.00	0.20	0.02	0.11	0.02	9.86	0.09	0.01	0.01		0.00					99.82
			sp	5	16.72	0.21	24.9	0.90	0.15	0.01	0.20	0.04	0.18	0.04	41.70	1.29	0.02	0.02	14.57	0.62	0.02	0.04	1.02	0.14					99.48
			L	5	15.9	0.22	12.3	0.05	47.6	0.25	10.0	0.10			0.35	0.22	0.14	0.03	11.1	0.12			1.05	0.05	0.42	0.03	0.04	0.01	99.01
w66-1	-1.7	1350	ol	9	51.3	0.13	0.13	0.01	41.3	0.17	0.35	0.02			0.06	0.01	0.12	0.02	6.47	0.07	0.01	0.02							99.78
			sp	8	24.4	0.16	61.7	0.72	0.14	0.02	0.09	0.03	0.26	0.01	7.0	0.68	0.06	0.03	6.14	0.26	0.02	0.02	0.22	0.01					99.96
			L	5	15.5	0.10	18.0	0.05	44.4	0.14	12.3	0.06			0.07	0.03	0.20	0.03	6.78	0.04			1.37	0.03	0.21	0.02	0.02	0.00	98.95

ph: phase; ol: olivine; sp: spinel; L: liquid; n: number of analyses; 1σ: one standard deviation.

Table 3.5 (continued) Major and minor element concentrations (wt%) determined by EMP in the experimental results.

Run	ΔQFM	T(°C)	ph	n	MgO	1σ	Al_2O_3	1σ	SiO_2	1σ	CaO	1σ	V_2O_3	1σ	Cr_2O_3	1σ	MnO	1σ	FeO	1σ	NiO	1σ	TiO_2	1σ	Na_2O	1σ	K_2O	1σ	SUM
w66-3	-1.7	1350	ol	7	49.4	0.15	0.12	0.01	41.0	0.11	0.35	0.02			0.11	0.01	0.15	0.02	8.69	0.15	0.01	0.01							99.75
			sp	8	21.6	0.27	50.3	1.43	0.15	0.04	0.13	0.03	0.31	0.03	17.8	1.54	0.03	0.02	8.97	0.16	0.02	0.03	0.31	0.02					99.53
			L	5	15.4	0.08	16.4	0.10	44.0	0.15	12.0	0.05			0.12	0.04	0.19	0.05	9.42	0.09			1.27	0.03	0.25	0.01	0.02	0.01	99.10
w61-1	-1.6	1400	ol	12	50.38	0.15	0.13	0.01	41.08	0.09	0.42	0.02		0.00	0.17	0.01	0.13	0.03	7.52	0.14	0.01	0.01		0.00					99.83
			sp	5	20.68	0.19	39.13	0.71	0.31	0.28	0.26	0.09	0.29	0.05	28.81	0.73	0.07	0.03	9.46	0.13	0.01	0.01	0.59	0.16					99.61
			L	5	18.0	0.07	13.7	0.10	43.2	0.10	12.6	0.07			0.21	0.03	0.19	0.03	9.73	0.20			1.33	0.04	0.06	0.01	0.01	0.01	99.01
w61-2	-1.6	1400	ol	10	49.4	0.14	0.09	0.00	40.9	0.14	0.28	0.02			0.25	0.01	0.09	0.02	8.95	0.08	0.01	0.01							99.92
			sp	5	16.9	0.18	21.6	0.63	0.18	0.03	0.14	0.06	0.29	0.03	47.4	1.04	0.01	0.01	12.8	0.21	0.02	0.03	0.62	0.06					100.0
			L	5	18.5	0.13	11.4	0.09	47.1	0.19	9.23	0.05			0.42	0.05	0.13	0.03	11.3	0.31			0.97	0.01	0.16	0.01	0.02	0.02	99.20
w60-1	-1.7	1450	ol	9	50.69	0.10	0.15	0.01	41.24	0.16	0.40	0.01		0.00	0.21	0.02	0.11	0.02	6.85	0.06	0.01	0.01		0.00					99.65
			sp	5	20.36	0.27	34.10	1.99	0.18	0.02	0.10	0.03	0.19	0.06	34.74	1.93	0.01	0.01	9.17	0.16	0.01	0.02	0.67	0.18					99.54
			L	5	20.0	1.44	12.9	0.40	42.8	0.21	11.7	0.52			0.33	0.03	0.16	0.04	10.4	0.29			1.24	0.06	0.05	0.02	0.01	0.01	99.47
w60-2	-1.7	1450	ol	10	49.9	0.10	0.10	0.00	41.0	0.11	0.24	0.02			0.29	0.02	0.08	0.01	8.16	0.08	0.01	0.01							99.79
			sp	7	16.8	0.08	18.1	0.35	0.17	0.01	0.12	0.04	0.23	0.02	51.7	0.41	0.01	0.01	11.9	0.11	0.01	0.02	0.52	0.02					99.58
			L	5	21.4	0.15	10.3	0.04	46.2	0.10	8.36	0.07			0.54	0.03	0.12	0.03	11.6	0.16			0.87	0.02	0.08	0.01	0.02	0.01	99.50

ph: phase; ol: olivine; sp: spinel; L: liquid; n: number of analyses; 1σ: one standard deviation.

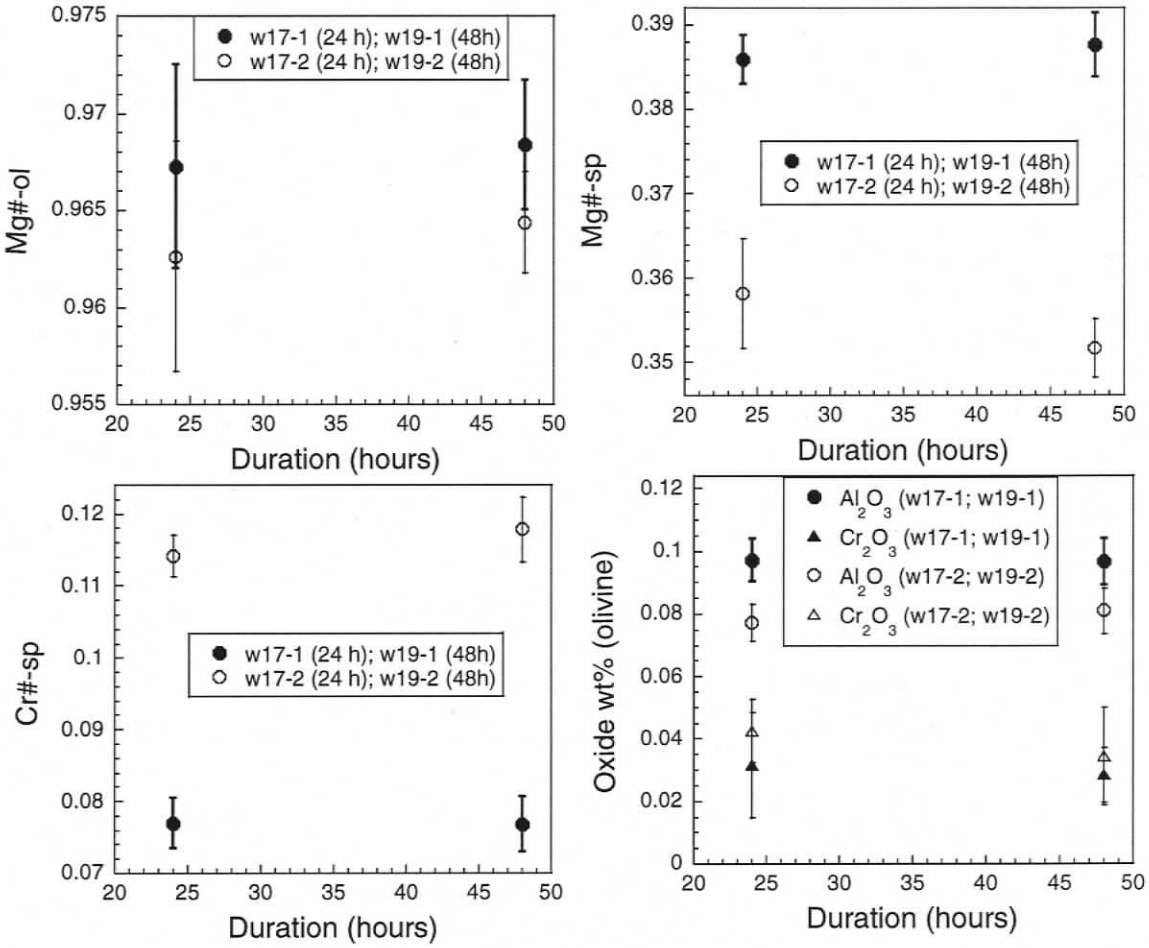

Figure 3.5 Olivine and spinel compositions over run times varying from 24 hours to 48 hours suggesting that equilibrium is attained within 24 hours. Mg#-ol: Mg# of olivine. Mg#-sp: Mg# of spinel. Cr#-sp: Cr# of spinel. The error bars are derived from the one standard deviation of Al_2O_3 and Cr_2O_3 concentration in olivine analyses.

3.6 Development of thermometers

3.6.1 Introduction

Experimental results can be divided into two groups based on experimental fO_2: the first group is at $\log(fO_2)$ = QFM – 1.8 and has Fe^{3+}# of spinel ranging from 0.02 to 0.05, and the second group is at $\log(fO_2)$ = QFM + 3.5-5 and has Fe^{3+}# of spinel ranging from 0.62 to 0.79. Because over 82% of the spinel from mantle peridotites has Fe^{3+}# < 0.1 (Figure 3.3b) and the aim of this study is to develop thermometers applicable for spinel-bearing peridotites, only the first group is used to calibrate the thermometers. By comparing $D_{Al}^{ol/sp}$ and $D_{Cr}^{ol/sp}$ between the first and second group, the effect of Fe^{3+}# of spinel on Al and Cr partitioning between olivine and spinel is examined.

3.6.2 The partitioning of Al between olivine and spinel: Al thermometer

The Cr# of spinel (Cr#-sp) in the experimental results for calibrating the thermometers ranges from 0.07 to 0.63. Since $D_{Al}^{ol/sp}$ is controlled by both temperature and Cr#-sp (Section 3.3), the temperature dependence of $D_{Al}^{ol/sp}$ should be tested at a narrow Cr#-sp range to eliminate the effect of Cr#-sp on $D_{Al}^{ol/sp}$. Therefore, experimental results are divided into four groups according to the Cr#-sp (0.07-0.2, 0.28-0.39, 0.42-0.47, and 0.49-0.63). Only those groups at Cr#-sp = 0.28-0.39 and Cr# = 0.49-0.63 are used to test the temperature dependence of $D_{Al}^{ol/sp}$ because of their wide temperature range (Figure 3.6). Two linear relationships between $\ln(D_{Al}^{ol/sp})$ and 10000/T are observed for these two groups (lines 1 and 2, Figure 3.6). This indicates that the partitioning of Al between olivine and spinel potentially makes a good thermometer. Before quantifying the relationship between temperature and $\ln(D_{Al}^{ol/sp})$, the effect of Cr#-sp on $\ln(D_{Al}^{ol/sp})$ is investigated.

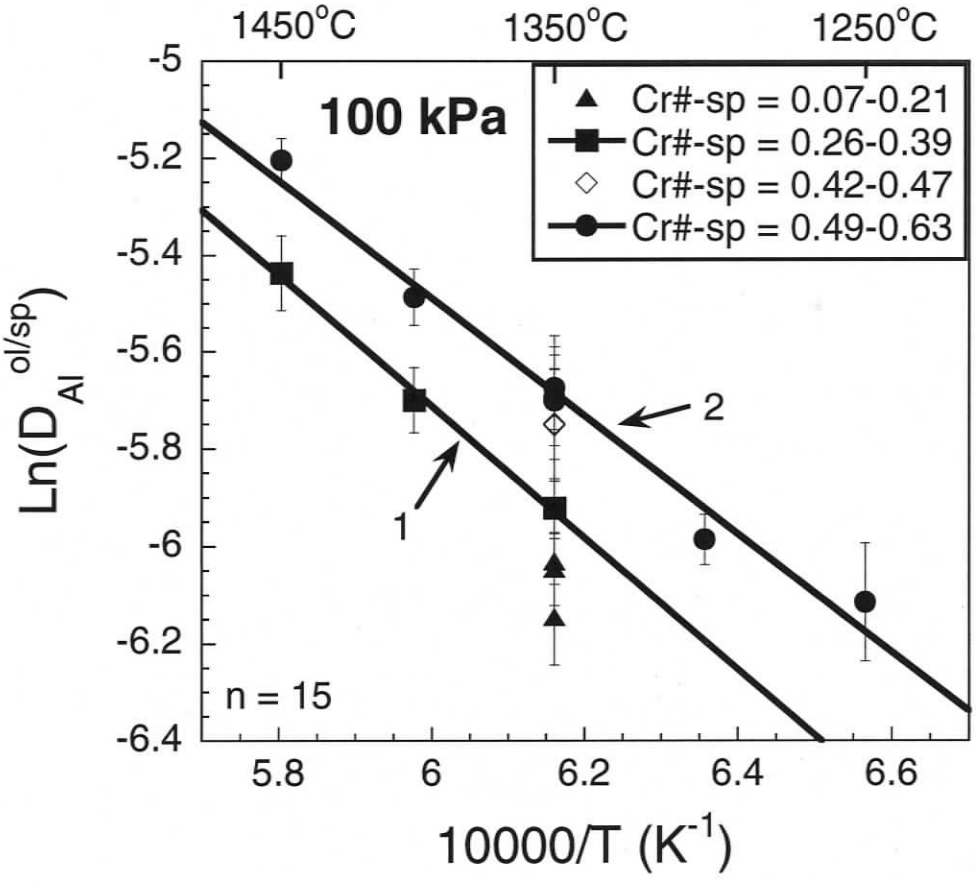

Figure 3.6 Plot of $\ln(D_{Al}^{ol/sp})$ versus 10000/T for experimental results from the present study at Fe^{3+}#-sp = 0.02-0.05 ($\log(fO_2)$ = QFM – 1.8). The results are shown in four groups according to the Cr# of spinel (Cr#-sp). The error bars for $\ln(D_{Al}^{ol/sp})$ are derived from the one standard deviation of Al_2O_3 concentrations in olivine. Lines 1 and 2 are least squares linear regressions of the results for experiments with Cr#-sp in the range of 0.28-0.39 and 0.49-0.63, respectively.

3.6.2.1 The effect of spinel Cr# on Al partitioning between olivine and spinel

A series of experiments at 1350°C at $\log(fO_2)$ = QFM – 1.8 (Table 3.3) are used to investigate the effect of Cr#-sp on $D_{Al}^{ol/sp}$ (Figure 3.7). These experimental results show that the dependence of $\ln(D_{Al}^{ol/sp})$ on Cr#-sp can be represented by a linear relationship. Although the thermodynamic model predicts a third order polynominal relationship between $\ln(D_{Al}^{ol/sp})$ and Cr#-sp at constant temperature (Section 3.3), it is not necessary to fit the these experimental results to a third order polynominal relationship because 1) the thermodynamic model is only preliminary, and 2) a linear regression of these experimental results represent the $\ln(D_{Al}^{ol/sp})$ - Cr#-sp relationship very well (R^2 = 0.96). Additionaly, the linear relation between $\ln(D_{Al}^{ol/sp})$ and Cr#-sp observed from the experimental results at 1350°C might indicate that the second order parameter K_2 and third order parameter K_3 in Equation (3.11) are small at 1350°C. The least-squares regression for the $\ln(D_{Al}^{ol/sp})$ - Cr#-sp data at 1350°C gives the following equation:

$$Ln(D_{Al}^{ol/sp}) = k*(Cr\#\text{-}sp) + b \qquad (3.12)$$

where $k = 0.98 \pm 0.06$, $b = -6.20 \pm 0.03$, *and* $R^2 = 0.96$ (solid line, Figure 3.7). Numbers 0.06 and 0.03 are standard errors of the regression coefficients k (0.98) and b (–6.20).

At temperatures of 1250°C, 1300°C, 1400°C, and 1450°C, experimental results in the present study are not sufficient for investigating the dependence of $\ln(D_{Al}^{ol/sp})$ on Cr#-sp since only one or two experiments were carried out at each of these temperatures (Figure 3.7). The thermodynamic model predicts different relationships between $\ln(D_{Al}^{ol/sp})$ and Cr#-sp at different temperature, because K_1, K_2 and K_3 in Equation (3.11) are expected to change with temperature (Section 3.2). However, the change of K_1, K_2 and K_3 with temperature is unknown, and K_2 and K_3 are suggested to be small by the

experimental results at 1350°C. Due to many unknown factors, the relationships between between $\ln(D_{Al}^{ol/sp})$ and Cr#-sp at temperatures 1250 °C, 1300 °C, 1400 °C, and 1450°C are not well understood. In this study, the relations between $\ln(D_{Al}^{ol/sp})$ and Cr#-sp at temperatures between 1250-1450°C are assumed to be parallel to that at 1350°C (dashed lines, Figure 3.7). These assumed relationships between $\ln(D_{Al}^{ol/sp})$ and Cr#-sp at 1400°C and 1450°C are consistent with the experimental results (Figure 3.7). The relationships between $\ln(D_{Al}^{ol/sp})$ and Cr#-sp at 1250-1450°C have the same slope as that at 1350°C (0.98) and can be expressed as:

$$Ln(D_{Al}^{ol/sp}) = 0.98*(Cr\#\text{-}sp) + c \qquad (3.13)$$

where c is the intercept of the linear relationship between $\ln(D_{Al}^{ol/sp})$ and Cr#-sp with the $\ln(D_{Al}^{ol/sp})$ axis. Note that c increases with increasing temperature. Equation (3.13) represents the relationship between $\ln(D_{Al}^{ol/sp})$ and Cr#-sp at 1250-1450°C. According to Equation (3.13), $\ln(D_{Al}^{ol/sp})$ at given Cr#-sp can be corrected to a fixed Cr#-sp (m) using the relationship

$$Ln(D_{Al}^{ol/sp})' = ln(D_{Al}^{ol/sp}) + 0.98*(m - Cr\#\text{-}sp) \qquad (3.14)$$

where $ln(D_{Al}^{ol/sp})'$ is the corrected value for Al_2O_3 partitioning between olivine and spinel at $Cr\#\text{-}sp = m$, and m is a number between 0.07 and 0.63.

The thermodynamic model (Section 3.3) indicates that the relationship between $\ln(D_{Al}^{ol/sp})$ and 10000/T should be investigated at constant Cr#-sp. Therefore, all experiments in the present study were corrected to a Cr#-sp of 0.5 because most experimental results contain spinel with a Cr# around 0.5. The corrected $\ln(D_{Al}^{ol/sp})$ values for all the experimental results follow the relation:

$$Ln(D_{Al}^{ol/sp})' = ln(D_{Al}^{ol/sp}) + 0.98*(0.5 - Cr\#\text{-}sp) \qquad (3.15)$$

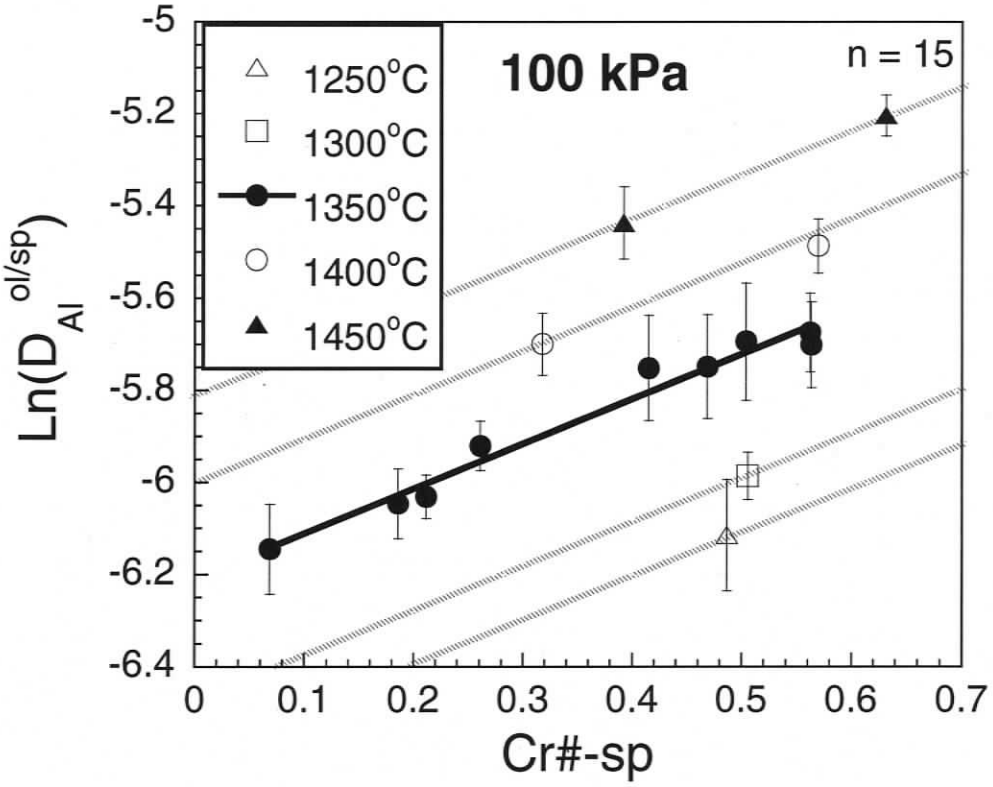

Figure 3.7 Dependence of $\ln(D_{Al}^{ol/sp})$ on Cr#-sp. Data were divided into different groups according to temperature. Cr#-sp: Cr# of spinel. The error bars are based on one standard deviation of the Al_2O_3 concentration of olivine. The solid line is the least squares linear regression of the data at 1350°C. Dashed lines are drawn by hand parallel to the solid line through data points at 1250°C, 1300°C, 1400°C and 1450°C; they represent the assumed linear relationships between $\ln(D_{Al}^{ol/sp})$ and Cr#-sp at 1250°C, 1300°C, 1400°C and 1450°C.

3.6.2.2 The effect of temperature on Al partitioning between olivine and spinel

The corrected values ($\ln(D_{Al}^{ol/sp})'$) for all experimental results represent the $D_{Al}^{ol/sp}$ at Cr#-sp = 0.5 over the temperature range of 1250-1450°C. Using $\ln(D_{Al}^{ol/sp})'$ values, the effect of temperature on the partitioning of Al between olivine at Cr#-sp = 0.5 can be quantified (Figure 3.8). The relationship between $\ln(D_{Al}^{ol/sp})'$ and temperature can be fitted using the relationship:

$$Ln(D_{Al}^{ol/sp})' = k*(10000/T) + b \qquad (3.16)$$

where $k = -1.05\pm0.05$, $b = 0.75\pm0.3$, and $R^2 = 0.97$. Numbers 0.05 and 0.3 are the standard errors for the regression coefficients k (–1.05) and b (0.75). By substituting Equation (3.15) into Equation (3.16), the following equation is derived

$$Ln(D_{Al}^{ol/sp}) + 0.98*(0.5–Cr\#\text{-}sp) = -1.05*(10000/T) + 0.75 \qquad (3.17)$$

Thus,

$$T = -10500 / \{[Ln(D_{Al}^{ol/sp}) – 0.98*(Cr\#\text{-}sp–0.5)] – 0.75)\} \qquad (3.18)$$

where T is in Kelvin. Equation (3.18) is the final geothermometer based on Al partitioning between olivine and spinel, hereafter named as the Al thermometer (T_{Al}).

3.6.2.3 Precision estimation

In order to estimate the precision for T_{Al}, calculated temperatures ($T_{calculated}$) using the Al thermometer are compared to the experimental temperature (T_{exp}) for each experimental result in the present study (Figure 3.9). All the calculated temperatures lie in the range of T_{exp} – 20 to T_{exp} + 15 (Figure 3.9). This suggests the precision for the estimated temperatures using the Al thermometer is ±20°C.

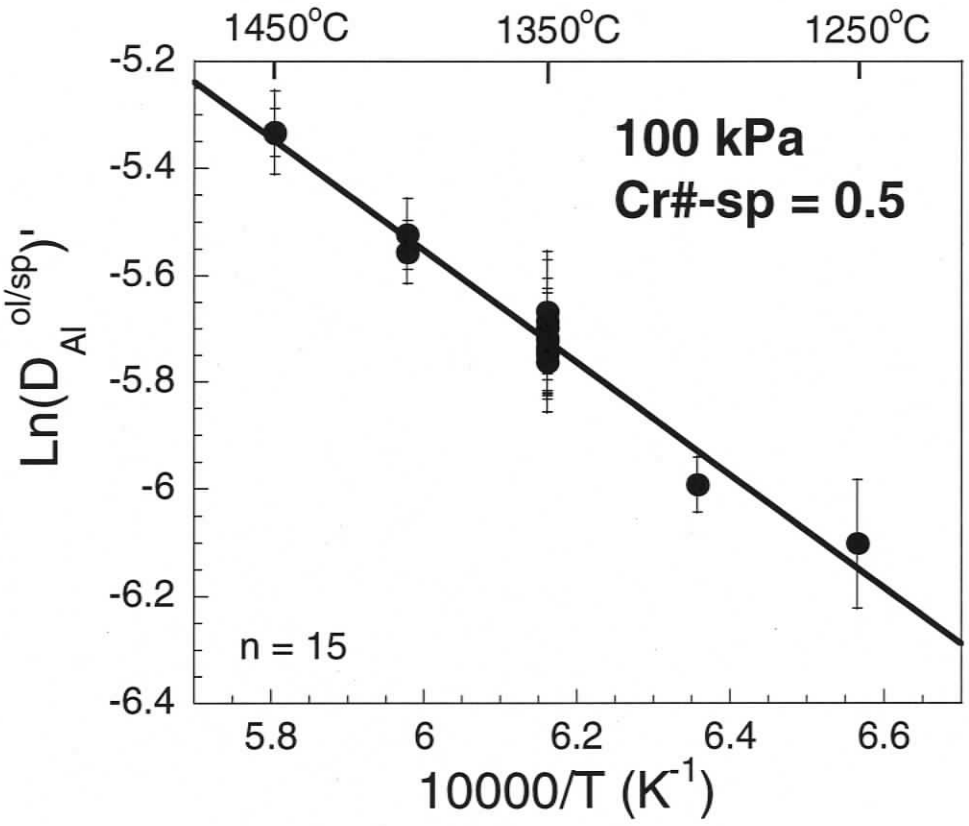

Figure 3.8 Plot of $\ln(D_{Al}^{ol/sp})$' versus 10000/T for all the experiments at $\log(fO_2)$ = QFM – 1.8 in the present study. $\mathrm{Ln}(D_{Al}^{ol/sp})$' is the corrected $\ln(D_{Al}^{ol/sp})$ to a Cr#-sp of 0.5 using Equation (3.15). n: number of experiments. Error bars are derived from one standard deviation of the Al_2O_3 concentration in olivine. The solid line is the least squares linear regression of all the data.

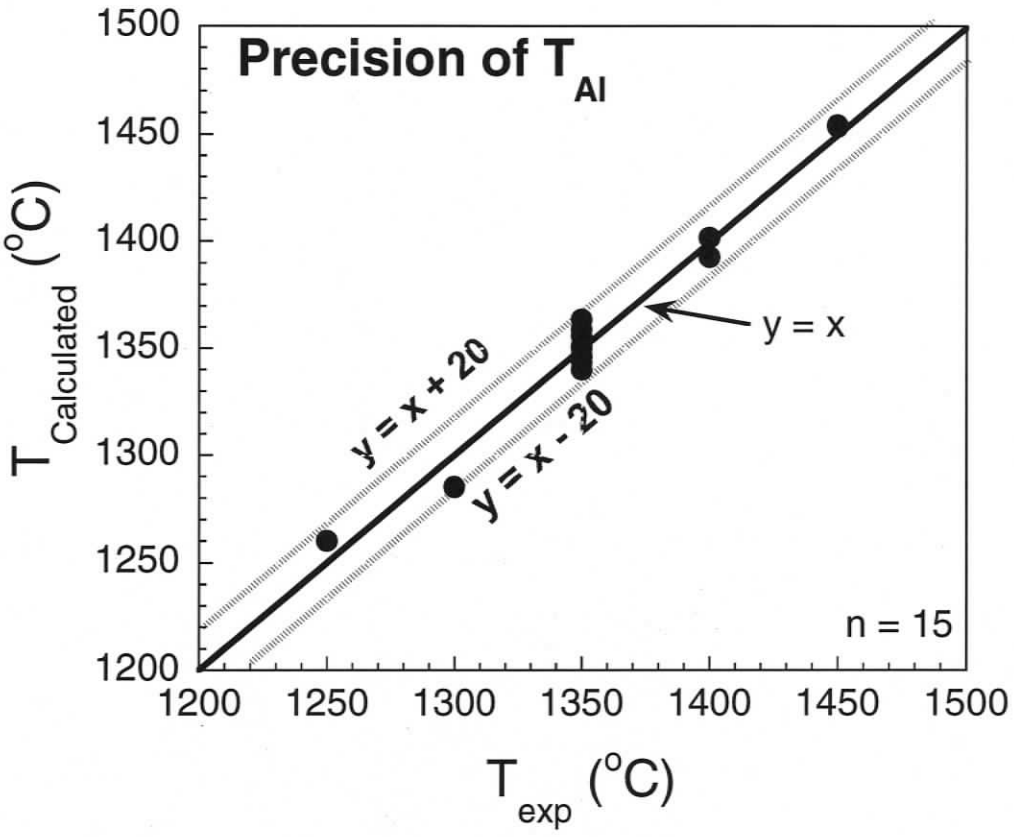

Figure 3.9 Comparison between the calculated temperature ($T_{Calculated}$) for experiments in this study using T_{Al} and the experimental temperature (T_{exp}). n: number of experiments. Solid line is y = x. Dashed lines are y = x + 20 and y = x – 20. All the calculated temperatures lie in the range of T_{exp} – 20 to T_{exp} + 20. This suggests the precision of the estimated temperature using T_{Al} is ± 20°C.

3.6.2.4 The effect of pressure on Al partitioning between olivine and spinel

One way to study the effect of pressure on $D_{Al}^{ol/sp}$ is to apply the Al thermometer developed in this study to experimental data at varying pressures. Experimental results in this study at low fO_2, experimental study of Grove and Bryan (1983) at 100 kPa, and the compiled data in Section 3.2.2 at high pressure conditions are employed. Only those data with Cr#-sp within the calibration range of the Al thermometer (Cr#-sp = 0.07-0.63) are used. Pressure and temperature ranges for the selected data are 100 kPa - 2 GPa and 900-1450°C. The difference between the calculated temperature and the experimental temperature are plotted against pressure in Figure 3.10. Although the large scatter in this plot caused by the low precision of Al_2O_3 concentration in olivine analyzed by EMP might hinder understanding of the effect of pressure on $D_{Al}^{ol/sp}$, no obvious effect of pressure on $D_{Al}^{ol/sp}$ over the pressure range from 100 kPa to 2 GPa is observed.

3.6.2.5 The effect of Fe^{3+}# in spinel on Al partitioning between olivine and spinel

Some of the experiments in this study were carried under high fO_2 (QFM + 3.5 to QFM + 5) conditions, and Fe^{3+}#-sp in the run products from these experiments ranges from 0.62 to 0.79. The comparison of $D_{Al}^{ol/sp}$ in these experimental results and $D_{Al}^{ol/sp}$ in the experimental results in which Fe^{3+}#-sp = 0.02 - 0.05 provides insight into the effect of Fe^{3+}#-sp on $D_{Al}^{ol/sp}$. Before studying the effect of Fe^{3+}#-sp on $D_{Al}^{ol/sp}$, the effect of Cr#-sp on $D_{Al}^{ol/sp}$ is accounted for by adjusting $\ln(D_{Al}^{ol/sp})$ to the corresponding value $\ln(D_{Al}^{ol/sp})'$ at Cr#-sp = 0.5 using Equation (3.15) for all of the experiments. The $\ln(D_{Al}^{ol/sp})'$ is plotted against Fe^{3+}#-sp at different temperature (Figure 3.11) and it shows that $\ln(D_{Al}^{ol/sp})'$ at higher Fe^{3+}#-sp is higher than that at lower Fe^{3+}#-sp. This suggests that T_{Al} should only be applied to samples that contain Fe^{3+}#-sp less than 0.1.

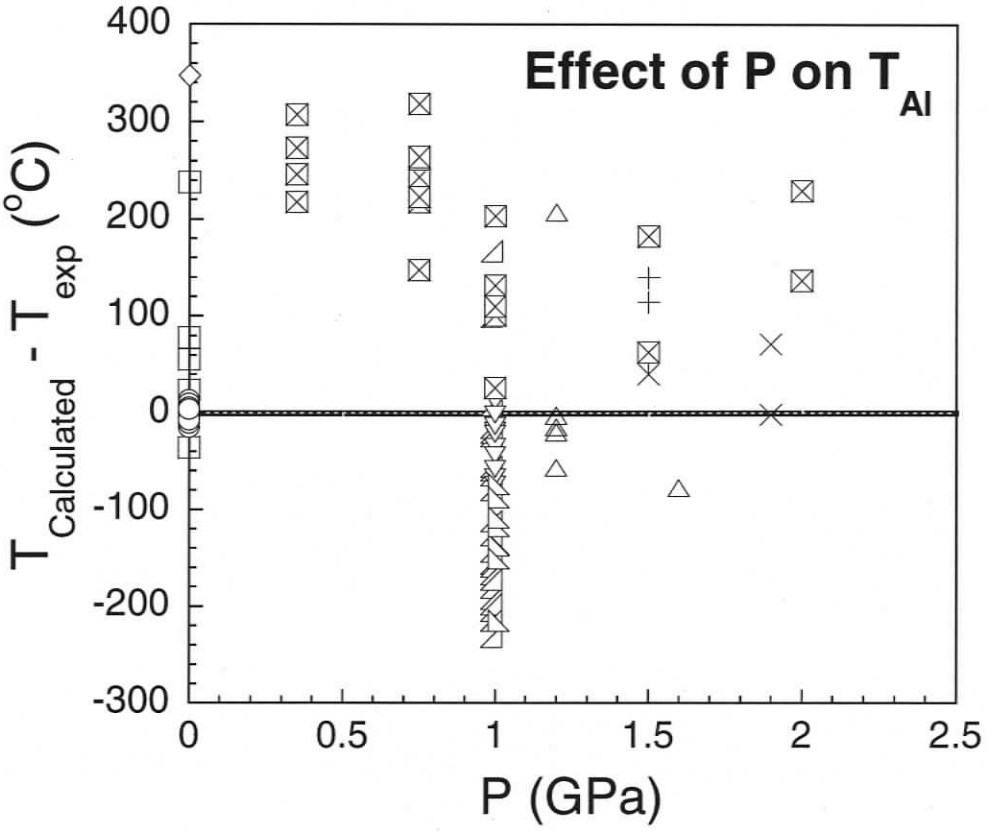

Figure 3.10 Plot of the difference between the calculated temperatures ($T_{Calculated}$) using T_{Al} and experimental temperatures (T_{exp}) against experimental pressure for published experimental results at Cr#-sp = 0.07-0.63 and the experimental results in the present study at $\log(fO_2)$ = QFM – 1.8. The scatter is most likely due to the poor precision of Al_2O_3 analyses in olivine in most experimental studies. No systematic effect of pressure on $T_{Calculated} - T_{exp}$ is observed. Data sources:

- △ Gaetani and Grove, 1998
- □ Grove and Bryan, 1983
- ◇ Tormey et al, 1987
- × Kinzler, 1997
- + Robinson et al, 1998
- ◿ Schwab and Johnston, 2001
- ▽ Pickering-Witter and Johnston, 2000
- ◺ Wasylenki et al, 2003
- ⊠ Bulatov et al, 2002
- ○ Experiments in the present study

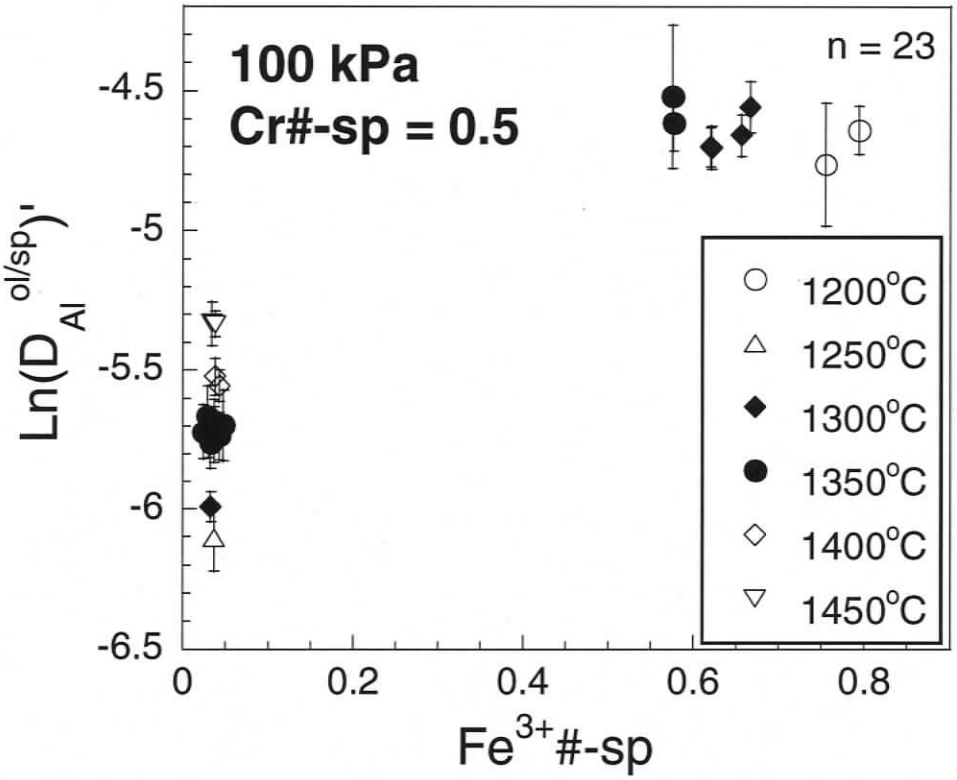

Figure 3.11 Effect of Fe^{3+}# of spinel on Al partitioning between olivine and spinel at Cr#-sp = 0.5. n: number of experiments. The $\ln(D_{Al}^{ol/sp})$' is the corrected value for $D_{Al}^{ol/sp}$ using Equation (3.15). The error bars are derived from one standard deviation of the Al_2O_3 concentration of olivine. This diagram shows that $\ln(D_{Al}^{ol/sp})$' is higher at high Fe^{3+}#-sp than that at low Fe^{3+}#-sp.

3.6.2.6 Summary

A geothermometer based on the exchange of Al_2O_3 between olivine and spinel that accounts for the Cr# of spinel has been experimentally calibrated:

$$T_{Al} = -10500 / \{[Ln(D_{Al}^{ol/sp}) - 0.98*(Cr\#\text{-}sp - 0.5)] - 0.75)\} \qquad (3.19)$$

where $D_{Al}^{ol/sp} = [Al_2O_3]^{ol}/[Al_2O_3]^{sp}$, $[Al_2O_3]^{ol}$ and $[Al_2O_3]^{sp}$ are the concentrations of Al_2O_3 in olivine and spinel (wt%), $Cr\#\text{-}sp = Cr/(Cr+Al+Fe^{3+})$ in spinel, and T is in Kelvin. The calibration range for this thermometer is P = 100 kPa, T = 1250-1450°C, Cr#-sp = 0.07-0.63, Fe^{3+}#-sp = 0.02-0.05, and $\log(fO_2)$ = QFM – 1.8. The estimated precision of this thermometer is ±20°C. No significant pressure effect on $D_{Al}^{ol/sp}$ is found based on comparison with published data from both high and low pressure experiments.

3.6.3 Preliminary analysis of Cr partitioning between olivine and spinel

The same experiments have been used to undertake a preliminary analysis of the partitioning of Cr between olivine and spinel at P = 100 kPa, T = 1250-1450°C, Cr#-sp = 0.07-0.63, and Fe^{3+}#-sp = 0.02-0.05. The $\ln(D_{Cr}^{ol/sp})$ for all the experiments are plotted against 10000/T in Figure 3.12 to test the temperature dependence of $D_{Cr}^{ol/sp}$. For experiments in which the Cr# of spinel is in the range of 0.28-0.63, there is a linear relationship between $\ln(D_{Cr}^{ol/sp})$ and 10000/T (Figure 3.12). This suggests that the partitioning of Cr between olivine and spinel makes a promising thermometer. However, $\ln(D_{Cr}^{ol/sp})$ at Cr#-sp = 0.07-0.21 is not consistent with the linear relationship defined by the data at Cr#-sp = 0.28-0.63 (Figure 3.12). Therefore, before quantifying the effect of temperature on $D_{Cr}^{ol/sp}$, the effect of Cr#-sp is studied first.

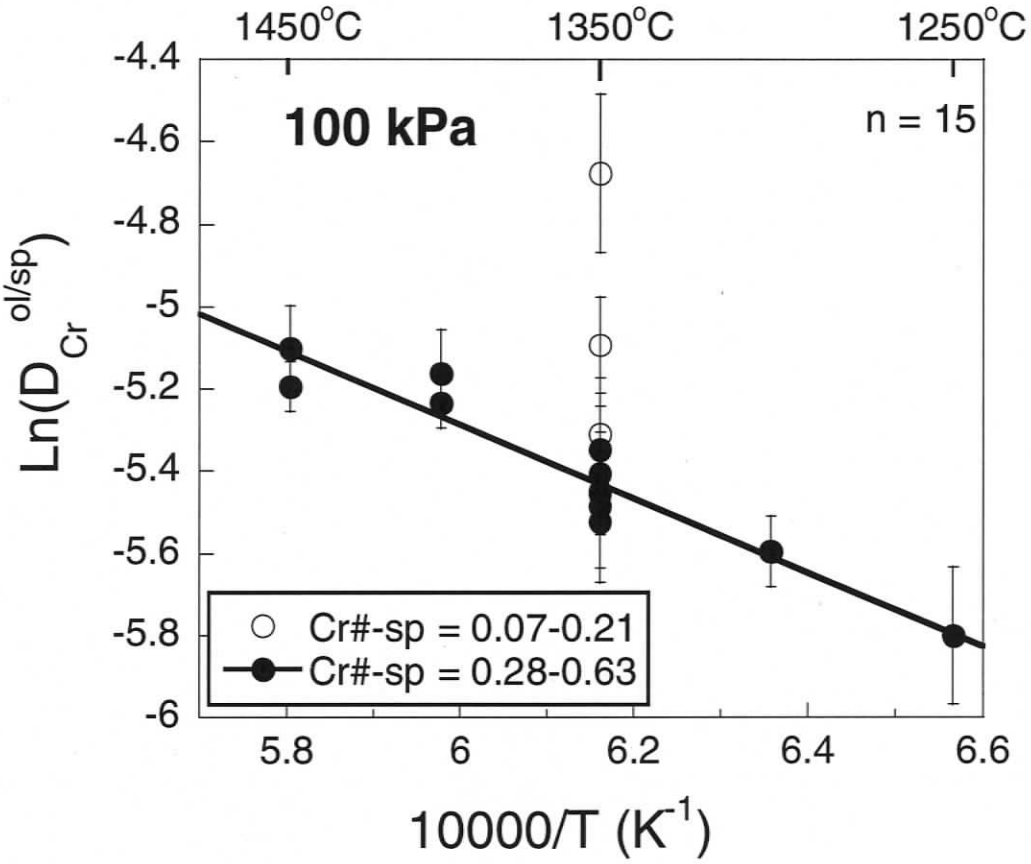

Figure 3.12 Plot of $\ln(D_{Cr}^{ol/sp})$ versus 10000/T for experimental results at Fe^{3+}# of spinel between 0.02 and 0.05 ($\log(fO_2)$ = QFM – 1.8) at 100 kPa in the present study. n: number of experiments. The error bars are derived from one standard deviation of Cr_2O_3 concentration in olivine. The data fall into two groups according to the Cr#-sp: Cr#-sp = 0.07-0.21 and Cr#-sp = 0.28-0.63. At Cr#-sp = 0.28-0.63, $\ln(D_{Cr}^{ol/sp})$ decreases linearly with increasing 10000/T and the solid line is the least squares linear regression of the data. The $\ln(D_{Cr}^{ol/sp})$ values at Cr#-sp = 0.07-0.21 are above the solid line.

3.6.3.1 The effect of spinel Cr# on Cr partitioning between olivine and spinel

A series of experiments at 1350°C at $\log(fO_2)$ = QFM – 1.8 (Table 3.3) with varying Cr#-sp in the run products are used to examine the relationship between $D_{Cr}^{ol/sp}$ and Cr#-sp (Figure 3.13). In these experiments, at high Cr#-sp (0.20-0.56), there is no obvious change on $D_{Cr}^{ol/sp}$ with changing Cr#-sp, and at low Cr#-sp (0.07-0.20), $D_{Cr}^{ol/sp}$ decreases with increasing Cr#-sp (Figure 3.13). However, the relationship between $D_{Cr}^{ol/sp}$ and Cr#-sp at Cr#-sp = 0.07-0.20 is not well constrained because there are only three data points in this Cr#-sp range and the error of $D_{Cr}^{ol/sp}$ at Cr# = 0.07 is large. Therefore, the data at Cr# < 0.2 are not considered in the calibration of the thermometer. For experiments at 1250°C, 1300°C, 1400°C, and 1450°C, Cr#-sp ranges from 0.3 to 0.63 and the relationship between $D_{Cr}^{ol/sp}$ and Cr#-sp is not clear since only one or two experiments were carried at each of these temperatures. The following assumption is made to calibrate the thermometer based on $D_{Cr}^{ol/sp}$: at Cr#-sp = 0.20-0.63, Cr#-sp has no effect on $D_{Cr}^{ol/sp}$ over a temperature range of 1250-1450°C.

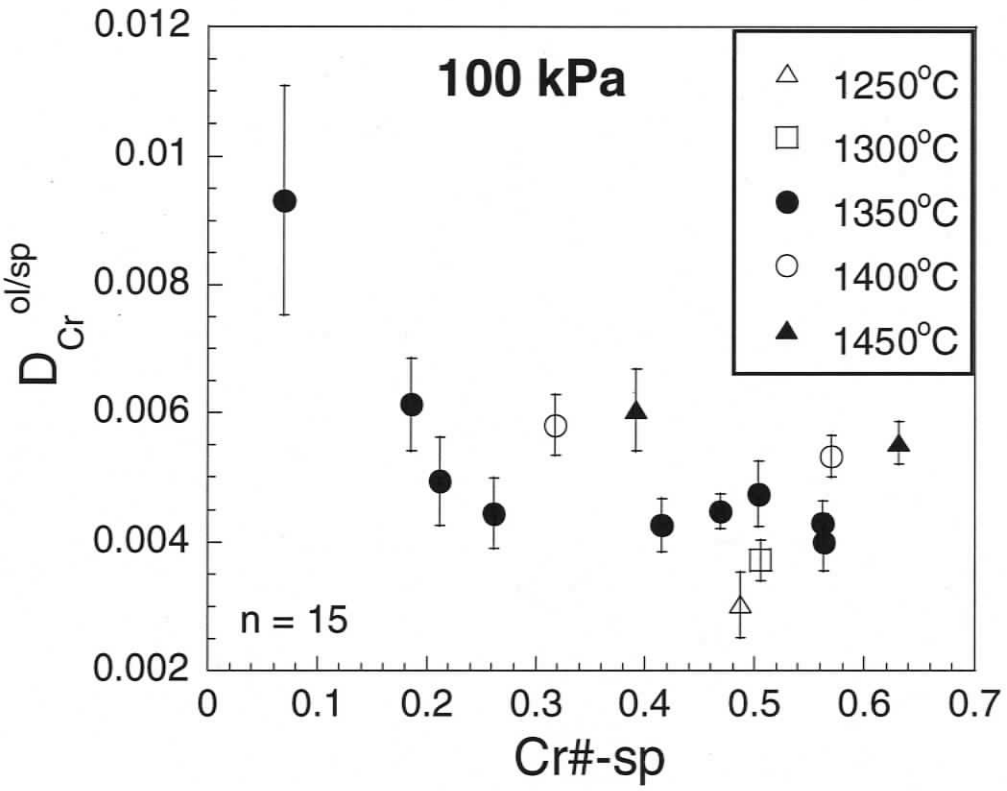

Figure 3.13 Plot of $D_{Cr}^{ol/sp}$ versus Cr#-sp for the experimental results in the present study that have Fe^{3+}#-sp ranging from 0.02 to 0.05. n: number of experiments. The error bars are derived from one standard deviation of the measured Cr_2O_3 concentration of olivine. At 1350°C, $D_{Cr}^{ol/sp}$ decreases with increasing Cr#-sp at Cr#-sp = 0.07-0.20 and is not significantly affected by Cr#-sp at Cr#-sp = 0.2-0.56. The relationship between $D_{Cr}^{ol/sp}$ and Cr#-sp is poorly constrained at 1250°C, 1300°C, 1400°C and 1450°C. Only those data at Cr#-sp > 0.2 are used for calibrating the thermometer based on Cr partitioning between olivine and spinel, and it is assumed that $D_{Cr}^{ol/sp}$ is not affected by Cr#-sp at Cr#-sp = 0.2-0.63 over the temperature range of 1250-1450°C.

3.6.3.2 The effect of temperature on Cr partitioning between olivine and spinel

Experiments at Cr# = 0.2-0.63 in the present study are chosen to calibrate the effect of temperature on $D_{Cr}^{ol/sp}$ (Figure 3.14). The least-squares regression for $\ln(D_{Cr}^{ol/sp})$ versus 10000/T gives the temperature dependence of $D_{Cr}^{ol/sp}$ at Cr#-sp = 0.20-0.63:

$$Ln(D_{Cr}^{ol/sp}) = k*(10000/T) + b \qquad (3.20)$$

where $k = -0.9\pm0.1$, $b = 0.02\pm0.6$, *and* $R^2 = 0.89$. Numbers 0.1 and 0.6 are standard errors for the regression coefficients k (–0.9) and b (0.02), respectively. The final version of the thermometer based on Cr partitioning between olivine and spinel is:

$$T = -9000/[ln(D_{Cr}^{ol/sp}) - 0.02] \qquad (3.21)$$

where T is in Kelvin. Equation (3.21) represent the empirical relation of $D_{Cr}^{ol/sp}$ and temperature over a temperature range of 1250-1450°C and Cr#-sp range of 0.2-0.63 at 100 kPa, hereafter named as the Cr thermometer (T_{Cr}).

3.6.3.3 Precision estimation

The method used to estimate the precision of T_{Cr} is the same as that for T_{Al}. Figure 3.15 is a plot of the calculated temperature ($T_{Calculated}$) using the Cr thermometer for the experiments in the present study against the experimental temperature (T_{exp}). All the $T_{Calculated}$ lie in the range between T_{exp} – 35 and T_{exp} + 50. Thus, the precision of temperatures calculated using T_{Cr} is estimated to be about ±50°C.

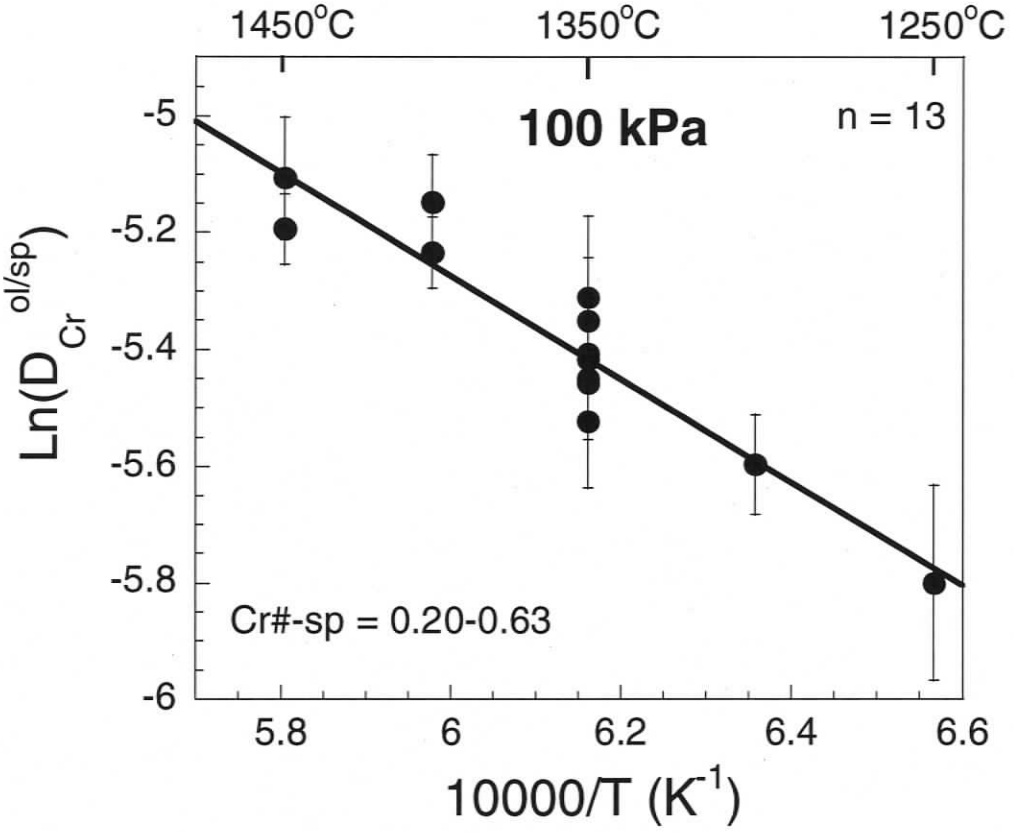

Figure 3.14 Plot of $\ln(D_{Cr}^{ol/sp})$ versus 10000/T at 100 kPa and at Fe^{3+}#-sp = 0.02-0.05 over a Cr#-sp range of 0.20-0.63. n: number of experiments. The error bars are derived from one standard deviation of the Cr_2O_3 concentration in olivine. Solid line is the least square linear regression of all the data.

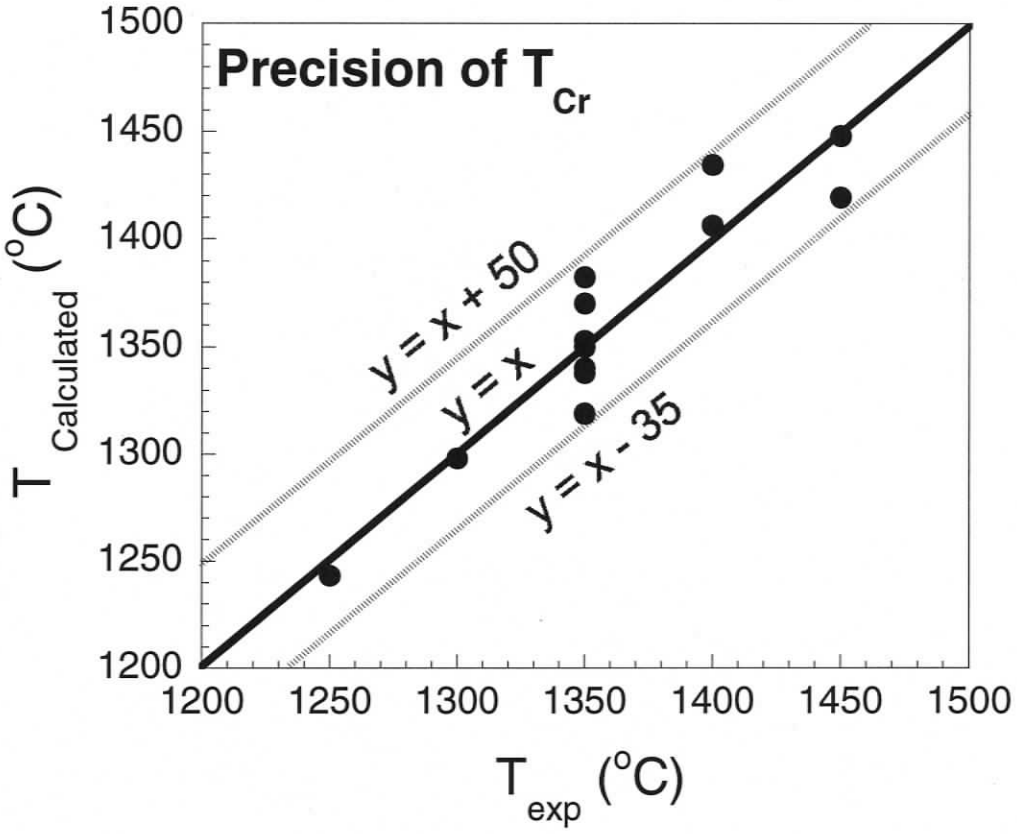

Figure 3.15 Comparison of the calculated temperature ($T_{Calculated}$) for experiments in this study using T_{Cr} and the experimental temperature (T_{exp}). Solid line is the y = x. Dashed lines are y = x + 50 and y = x – 35. All the calculated temperatures lie in the range of T_{exp} – 35 to T_{exp} + 50, which suggests the precision for the thermometer is ± 50°C.

3.6.3.4 The effect of pressure on Cr partitioning between olivine and spinel

Compiled experimental data for investigating the temperature dependence of $D_{Cr}^{ol/sp}$ (Section 3.2.2) are employed to study the effect of pressure on $D_{Cr}^{ol/sp}$. Only those experimental data with Cr#-sp = 0.20-0.63 in the run products are selected, since the Cr thermometer is calibrated for spinel with Cr# = 0.2-0.63. Pressure and temperature ranges for the selected data are 0.35 GPa - 2 GPa, and 900-1450°C. As shown in Figure 3.16, the difference between the calculated temperature ($T_{Calculated}$) and the experimental temperature (T_{exp}) ranges from -100°C to 800°C. This scatter is most likely caused by the low precision of the Cr_2O_3 concentration in olivine analyzed by EMP. Despite the scatter of the data, $T_{Calculated}$ for most experiments is higher than T_{exp}. This suggests that the Cr thermometer underestimates experimental temperatures at high pressures, which indicates that $D_{Cr}^{ol/sp}$ may decrease with increasing pressure.

3.6.3.5 The effect of Fe^{3+}# of spinel on Cr partitioning between olivine and spinel

The effect of Fe^{3+}#-sp on $D_{Cr}^{ol/sp}$ is studied by comparing the $D_{Cr}^{ol/sp}$ in the experimental results at low fO_2 and at high fO_2. The Cr# of spinel in experiments carried under high fO_2 (QFM + 3.5-5) conditions ranges from 0.03 to 0.18. Since the effect of Cr#-sp on $D_{Cr}^{ol/sp}$ is not known at Cr#-sp < 0.2, the effect of Fe^{3+}#-sp on $D_{Cr}^{ol/sp}$ should be investigated at constant temperature within narrow Cr#-sp ranges. Only four experiments (two at high fO_2 and two at low fO_2) at 1350°C with Cr#-sp = 0.13-0.21 in the run products fit the requirement (Figure 3.17). The results from these experiments show that $D_{Cr}^{ol/sp}$ is smaller at high Fe^{3+}#-sp than that at low Fe^{3+}#-sp. However, the effect of Fe^{3+}#-sp on $D_{Cr}^{ol/sp}$ cannot be ruled out due to the lack of data.

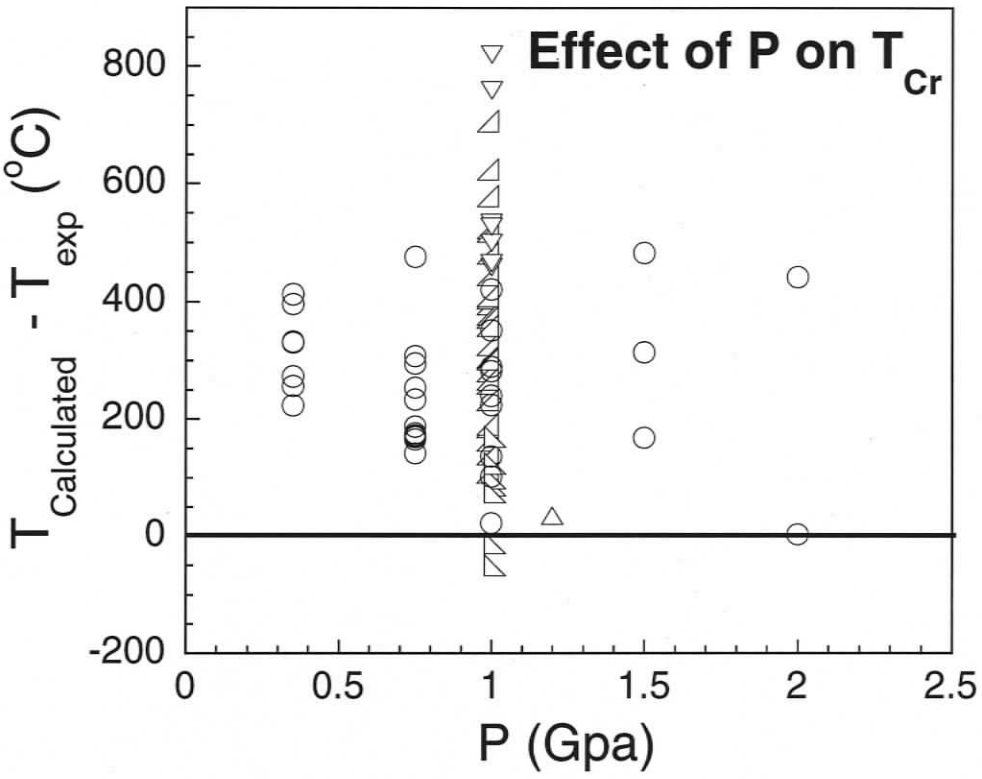

Figure 3.16 Plot of the difference between the calculated temperatures ($T_{Calculated}$) using T_{Cr} and experimental temperatures (T_{exp}) against the experimental pressure for published experimental results at Cr#-sp = 0.20-0.63. The scatter of the data is likely caused by the low precision of the Cr_2O_3 concentration in olivine analyzed by EMP. Data sources: △: Gaetani and Grove, 1998; ◿ : Schwab and Johnston, 2001; ▽ : Pickering-Witter and Johnston, 2000; ◺ : Wasylenki et al, 2003; O: Bulatov et al, 2002.

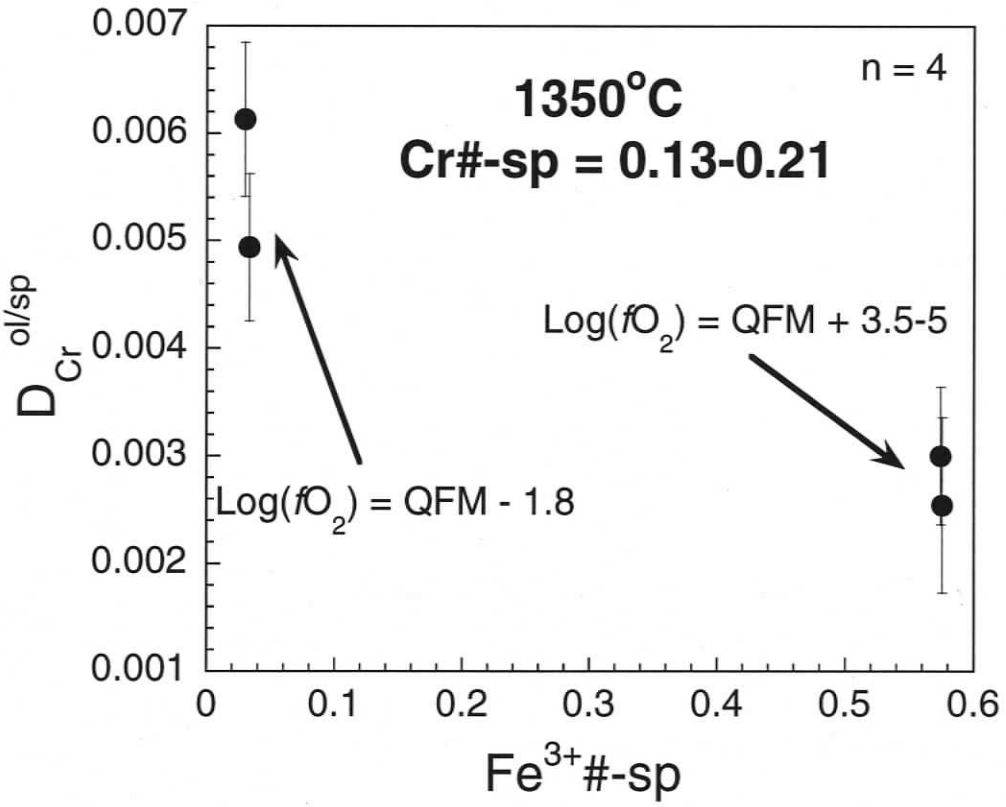

Figure 3.17 Plot of $D_{Cr}^{ol/sp}$ versus Fe^{3+}#-sp at 100 kPa, 1350°C, Cr#-sp = 0.13-0.21, and log(fO_2) = QFM + 3.5-5 and QFM – 1.8. n: number of experiments. The error bars are derived from one standard deviation of the Cr_2O_3 concentration of olivine. This diagram shows that $D_{Cr}^{ol/sp}$ at high Fe^{3+}#-sp is lower than that at low Fe^{3+}#-sp at 1350°C within a Cr#-sp range of 0.13 to 0.21. Alternatively, the difference between $D_{Cr}^{ol/sp}$ at different Fe^{3+}#-sp might be caused by the different Cr^{3+}/Cr^{2+} ratios in olivine.

3.6.3.6 Summary

A preliminary geothermometer based on Cr partitioning between olivine and spinel at 100 kPa and Cr#-sp = 0.2-0.63 was developed:

$$T_{Cr} = -9000/[\ln(D_{Cr}^{ol/sp}) - 0.02] \quad (3.22)$$

where $D_{Cr}^{ol/sp} = [Cr_2O_3]^{ol}/[Cr_2O_3]^{sp}$, $[Cr_2O_3]^{ol}$ and $[Cr_2O_3]^{sp}$ are the concentrations of Cr_2O_3 in olivine and spinel (wt%), *Cr#-sp* is $Cr/(Cr+Al+Fe^{3+})$ cation ratio in spinel, and *T* is in Kelvin. The calibration range for this thermometer is P = 100 kPa, T = 1250-1450°C, Cr#-sp = 0.20-0.63, Fe^{3+}#-sp = 0.02-0.05, and $\log(fO_2)$ = QFM – 1.8. The estimated precision of the Cr thermometer is ±50°C. Caution is suggested when using this geothermometer due to poor constraints on the role of Cr#-sp in controlling $D_{Cr}^{ol/sp}$.

3.7 Discussion

In this section, the lattice strain model (Blundy and Wood, 1994) is used to model the expected temperature dependence of Al and Cr substitution into the olivine structure. Experimental results in the present study are compared to these predictions. Additionally, the experimental results from the present study, along with the published experimental data, are used to test the other thermometers calibrated for cation exchange between olivine and spinel: the Fe-Mg exchange thermometer (Ballhaus et al, 1991; Fabries, 1977; Kretz, 1994; O'Neill and Wall, 1987).

3.7.1 Comparison between the present study and the lattice strain model

In general, the trace element partition coefficient between two phases is controlled by temperature, pressure, and the major element compositions of both phases (e.g.

O'Neill and Eggins, 2002; Witt-Eickschen & O'Neill, 2005). Traditionally, the partitioning of trace elements is modeled as a reaction, either by formation or exchange (e.g. Salters et al, 2002). Blundy and Wood (1994) proposed a model for calculating the absolute value of trace element partition coefficients (D) between minerals and melt based on how well the ion "fits" in the lattice of the crystal. Their expression is:

$$D_i(P,T,X) = D_o(P,T,X) * exp((-4\pi EN[1/2r_o(r_i-r_o)^2 + 1/3(r_i-r_o)^3])/RT) \quad (3.23)$$

where r_o is the optimum radius of the lattice site, r_i is the radius of the cation substitution into the lattice, N is Avogadro's number, E is the Young's modulus of the lattice site, and $D_o(P,T,X)$ is the "strain-compensated partition coefficient", which describes strain-free cation substitution ($r_i = r_o$) at the P, T and composition of interest. At a fixed temperature, pressure and phase composition, for a suite of isovalent cations entering a particular mineral lattice site, the Blundy and Wood (1994) model gives a parabolic distribution of ln(D) values centered at the ionic radius of the host site 'r_0', which gives the position of the curve apex on the ionic radius axis (Figure 3.18).

In the olivine structure, Mg^{2+} and Fe^{2+} occupy the octahedral site (M site) and Si^{4+} occupies the tetrahedral site (T site). Based on the lattice strain model, Taura et al (1998) concluded that Al^{3+} could enter both the M and T sites in the olivine structure because its ionic radius (0.535×10^{-10} m) lies between the optimum radius of the M site (0.71×10^{-10} m) and the optimum radius of the T site (~0.4×10^{-10} m). Taura et al (1998) also concluded that Cr^{3+} would only enter the M site of olivine because its ionic radius (0.615×10^{-10} m) is closer to the optimum radius of the M site (0.71×10^{-10} m) than the optimum radius of the T site (~0.4×10^{-10} m).

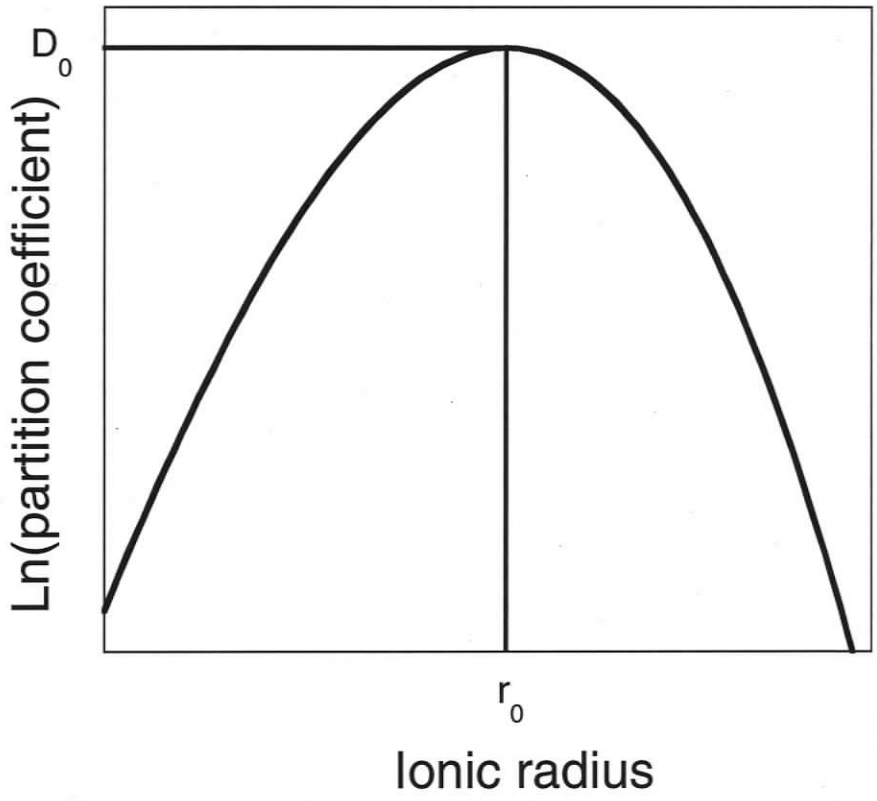

Figure 3.18 Schematic diagram illustrating the lattice strain model of trace element partitioning (after Blundy and Wood, 2003). For an isovalent series of ions entering a crystal lattice site, the partitioning coefficient can be described in terms of three parameters: r_0 (the radius of that site), E (the Young's modulus of that site that controls the tightness of the parabola), and D_0 (the partitioning coefficient for a (fictive) ion with radius r_0) according to Equation (3.23).

Although the absolute value of $D_{Cr}^{ol/L}$ and $D_{Al}^{ol/L}$ for Cr and Al substitution into the M site of olivine cannot be calculated since D_0 is unknown in Equation (3.23), the difference between the temperature dependence of Cr and Al substitution into the olivine structure can be calculated. According to Equation (3.23),

$$D_{Cr}^{ol/L} = D_0 * exp((-4\pi EN[1/2r_o(r_{Cr}-r_o)^2 + 1/3(r_{Cr}-r_o)^3])/RT) \quad (3.24)$$

$$D_{Al}^{ol/L} = D_0 * exp((-4\pi EN[1/2r_o(r_{Al}-r_o)^2 + 1/3(r_{Al}-r_o)^3])/RT) \quad (3.25)$$

Therefore,

$$Ln((D_{Cr}^{ol/L})/(D_{Al}^{ol/L})) = (-4\pi EN[1/2r_o(r_{Cr}-r_o)^2+1/3(r_{Cr}-r_o)^3])/RT - (-4\pi EN[1/2r_o(r_{Al}-r_o)^2+1/3(r_{Al}-r_o)^3])/RT \quad (3.26)$$

The difference between the temperature dependence of Cr and Al substitution into the olivine structure can also be calculated using the experimental results in the present study. Dividing the relationship between $D_{Cr}^{ol/sp}$ and 10000/T at Cr#-sp = 0.2-0.63 (Equation (3.20)) by the relationship between $D_{Al}^{ol/sp}$ and 10000/T at Cr#-sp = 0.5 (Equation (3.16)) yields the following equation:

$$Ln((D_{Cr}^{ol/sp})/(D_{Al}^{ol/sp})) = (0.02-9000/T)/(0.8-1.0500/T) \quad (3.27)$$

Using E = 360 GPa and $r_0 = 0.71 \times 10^{-10}$ m, $\ln((D_{Cr}^{ol/L})/(D_{Al}^{ol/L}))$ is calculated over a temperature range of 1200-1450°C using Equation (3.26). The $\ln((D_{Cr}^{ol/sp})/(D_{Al}^{ol/sp}))$ is also calculated over the same temperature range using Equation (3.27). Both $\ln((D_{Cr}^{ol/L})/(D_{Al}^{ol/L}))$ and $\ln((D_{Cr}^{ol/sp})/(D_{Al}^{ol/sp}))$ decrease with increasing temperature (Figure 3.19). This suggests that Cr substitution into the olivine structure is less sensitive to temperature than Al substitution into the olivine structure. The predicted difference between the temperature dependence of Cr and Al substitution into the M site of olivine from the lattice strain model is consistent with the experimental results in this study.

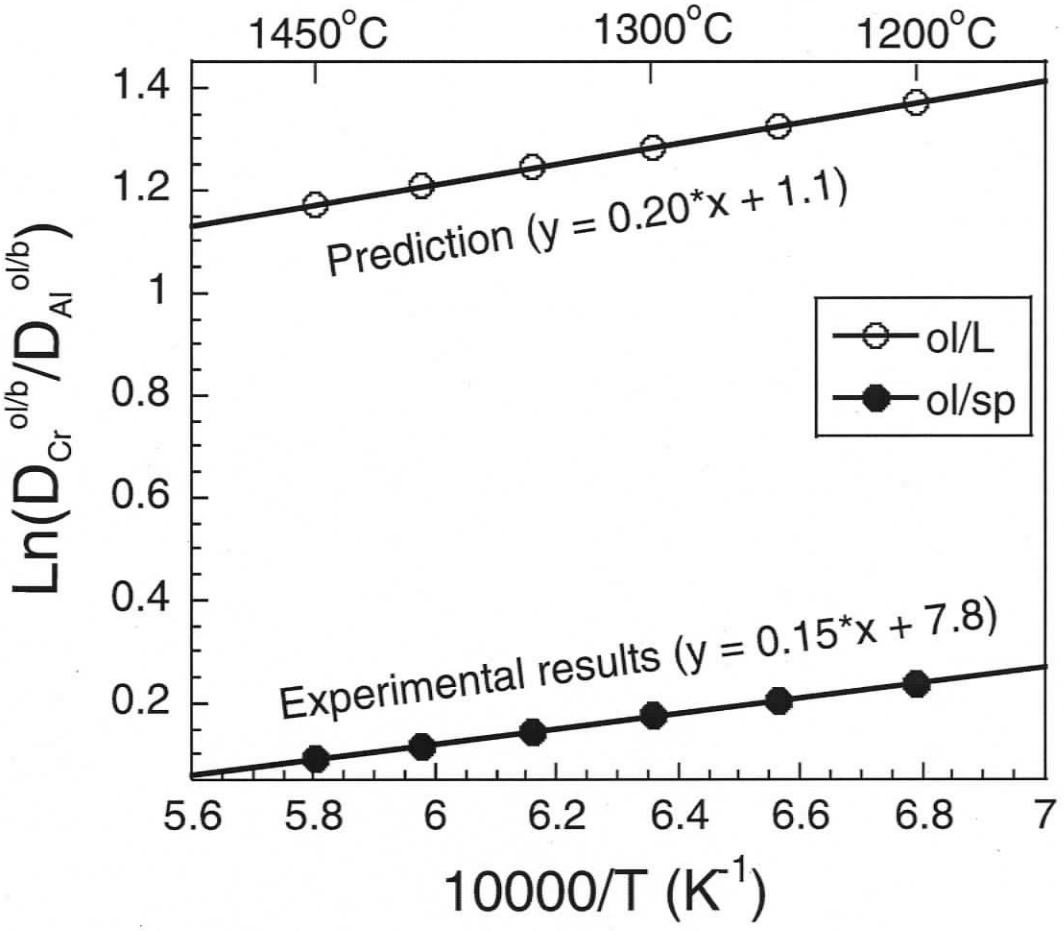

Figure 3.19 Plot of $\ln((D_{Cr}^{ol/L})/(D_{Al}^{ol/L}))$ and $\ln((D_{Cr}^{ol/sp})/(D_{Al}^{ol/sp}))$ versus 10000/T. "b" in $\ln((D_{Cr}^{ol/b})/(D_{Al}^{ol/b}))$ represents liquid (open circle) or spinel (solid circle). Symbols represent the calculated $\ln((D_{Cr}^{ol/L})/(D_{Al}^{ol/L}))$ and $\ln((D_{Cr}^{ol/sp})/(D_{Al}^{ol/sp}))$ at corresponding temperatures using Equation (3.26) and (3.27). Solid lines are the linear regression of the data. The difference between the slopes of the experimental results (0.15) and the prediction (0.20) might be caused by the existence of Cr^{2+} in olivine or that Al can substitute both M and T sites of the olivine structure.

3.7.2 Testing thermometers based on Fe-Mg exchange between olivine and spinel

Because the Fe-Mg olivine-spinel exchange thermometer is the only existing thermometer for olivine-spinel assemblages, it seems prudent to test this thermometer using the new experimental data for comparison with T_{Al}. The distribution of Fe^{2+} and Mg between olivine and spinel can be expressed as:

$$1/2Fe_2SiO_4 + Mg(Al,Cr,Fe^{3+})_2O_4 = 1/2Mg_2SiO_4 + Fe(Al,Cr,Fe^{3+})_2O_4 \qquad (3.28)$$

olivine spinel olivine spinel

The distribution coefficient of Mg and Fe between olivine and spinel is

$$K_{DMg/Fe}^{ol/sp} = (X_{Mg}^{ol} * X_{Fe2+}^{sp}) / (X_{Fe}^{ol} * X_{Mg}^{sp}) \qquad (3.29)$$

where X_i^{α} is the mole fraction of component i in phase α. The $K_{DMg/Fe}^{ol/sp}$ is dependent on temperature and the mole fractions of trivalent ions i: Y^i_{sp} = i/(Cr+Al+Fe^{3+}), where i is Cr, Al, or Fe^{3+}, especially Y_{Cr}^{sp}, and many different versions of this thermometer have been developed (e.g. Irvine, 1965; Fabries, 1977; O'Neill and Wall, 1987; Ballhaus et al, 1991; Kretz, 1994).

In the present study, for the experiments in which the Fe^{3+}#-sp ranges from 0.02 to 0.05, $K_{DMg/Fe}^{ol/sp}$ shows a strong dependence on Cr#-sp, and the dependence of $K_{DMg/Fe}^{ol/sp}$ on temperature is within the precision of the data (Figure 3.20). These data are used to test the four most recent versions of Mg-Fe olivine-spinel thermometers calibrated by Fabries (1977), O'Neill and Wall (1987), Ballhaus et al (1991), and Kretz (1994), hereafter named as $T_{Fabries}$, $T_{O'Neill\ and\ Wall}$, $T_{Ballhaus}$, and T_{Kretz}. These four versions of the Fe-Mg olivine-spinel exchange thermometer do not reproduce the experimental temperature very well (Figure 3.21). The $T_{Fabries}$, $T_{Ballhaus}$, and $T_{O'Neill\ and\ Wall}$ underestimate the experimental temperature by 0-360°C. The T_{Kretz} reproduces the experimental temperature better, but the difference between T_{Kretz} and T_{exp} is still large (–100-160°C).

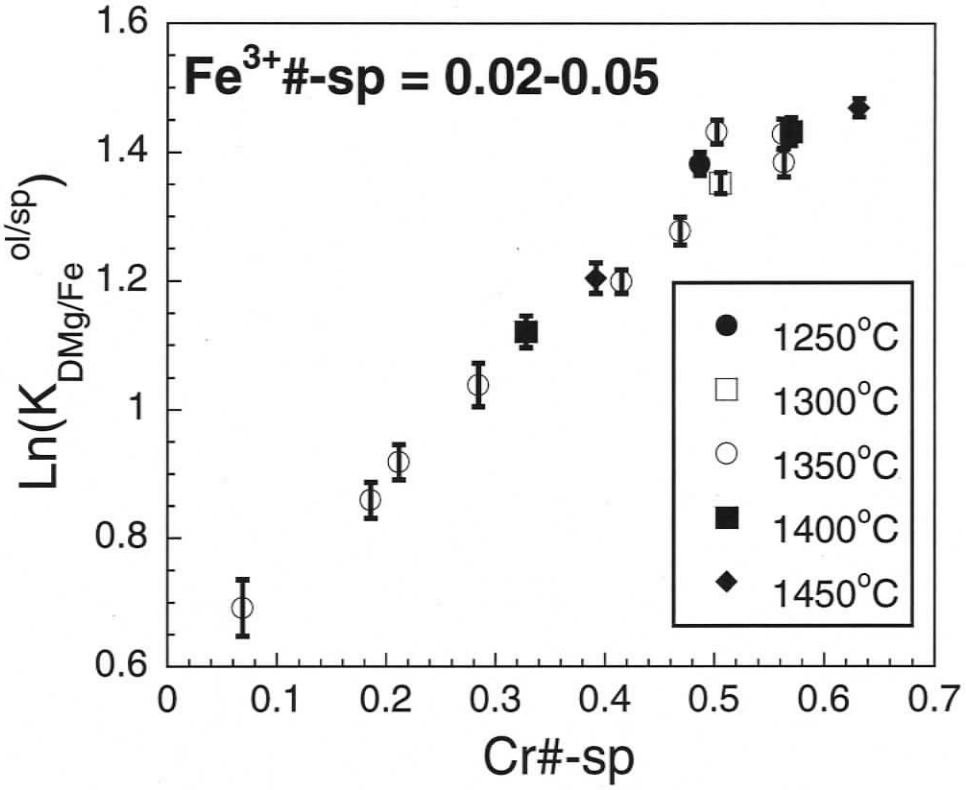

Figure 3.20 Plot of $\ln(K_{DMg/Fe}^{ol/sp})$ versus Cr# of spinel for the experimental products at Fe^{3+}#-sp = 0.02-0.05 in this study. $K_{DMg/Fe}^{ol/sp}$: distribution coefficient of Mg and Fe exchange between olivine and spinel. Error bars are derived from one standard deviation of MgO and FeO concentrations in olivine and spinel. Data are shown in different groups according to temperature. This diagram shows that $K_{DMg/Fe}^{ol/sp}$ increases exponentially with increasing Cr#-sp in the experimental products at Fe^{3+}#-sp = 0.02-0.05 in this study. The temperature dependence of $K_{DMg/Fe}^{ol/sp}$ is within the precision of the data.

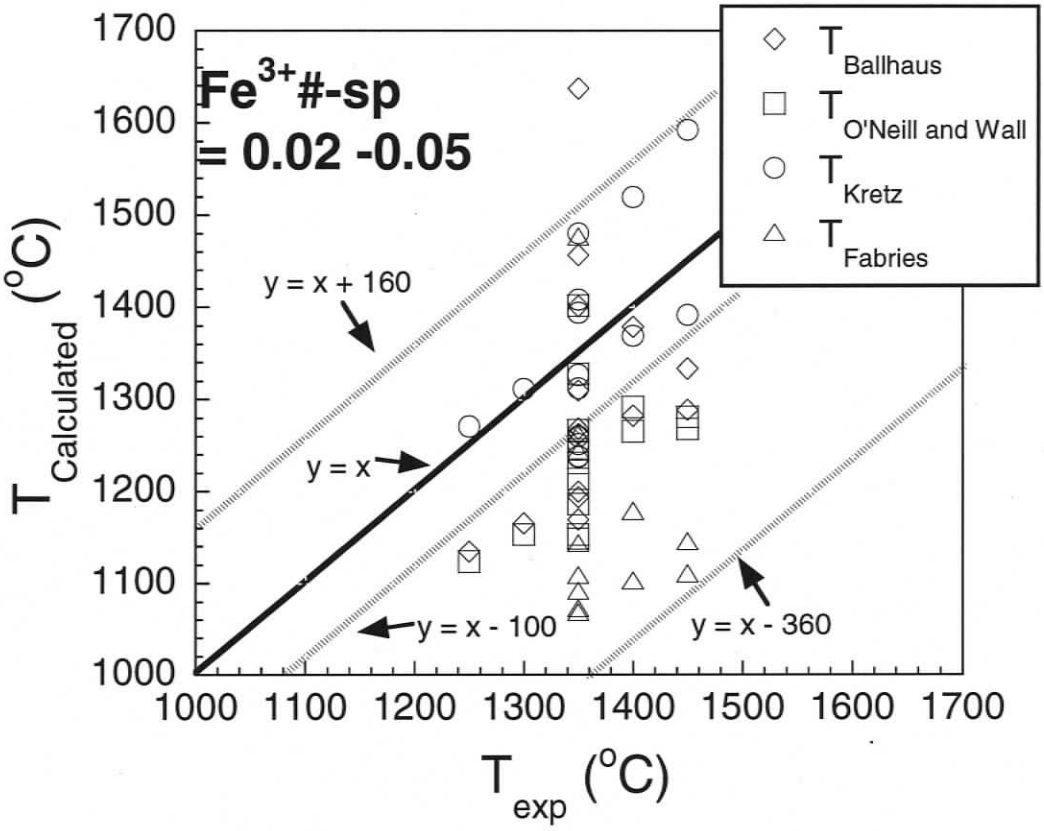

Figure 3.21 Plot of calculated temperatures ($T_{Calculated}$) for the experiments in this study with Fe^{3+}#-sp = 0.02-0.05 using various Mg-Fe olivine-spinel thermometers versus the experimental temperature (T_{exp}). Temperatures calculated using the Mg-Fe olivine-spinel thermometer developed by Fabries (1977), O'Neill and Wall (1987), Ballhaus et al (1991), and Kretz (1994) are represented by $T_{Fabries}$, $T_{O'Neill\ and\ Wall}$, $T_{Ballhaus}$, and T_{Kretz}, respectively.

In order to understand the cause of the difference between $T_{Calculated}$ and T_{exp}, other experimental studies that have olivine and spinel in the run products are compiled and $T_{Fabries}$, T_{Kretz}, $T_{O'Neill\ and\ Wall}$, and $T_{Ballhaus}$ are also applied to these experimental results. The difference between $T_{Calculated}$ and T_{exp} is plotted against experimental pressure, T_{exp}, Cr#-sp, Mg#-sp, Fe^{3+}#-sp, and Mg#-ol for these four versions of the Fe-Mg olivine-spinel thermometer in Figures 3.22, 3.23, 3.24, and 3.25.

For $T_{Ballhaus}$, no obvious systematic dependence of $T_{Ballhaus} - T_{exp}$ on pressure, temperature, Cr#-sp, Fe^{3+}#-sp, Mg#-sp, and Mg#-ol is found (Figures 3.22). However, this thermometer underestimates the experimental temperature by 0-400°C (Figure 3.22). The same observation is found for $T_{O'Neill\ and\ Wall}$ (Figure 3.23). The difference between $T_{O'Neill\ and\ Wall}$ and T_{exp} increases with increasing Cr#-sp (Figure 3.23). Figure 3.24 shows that $T_{Fabries}$ is 0-400°C lower than T_{exp} and $T_{Fabries} - T_{exp}$ decreases with increasing Fe^{3+}#-sp (Figure 3.24d). Figure 3.25 shows that $T_{Kretz} - T_{exp}$ increases with increasing Cr#-sp (Figure 3.25c). This indicates that T_{Kretz} does not correct for the effect of Cr#-sp on $K_{DMg/Fe}^{ol/sp}$ accurately in its calibration. Kessel et al (2007) also tested different versions of the olivine-spinel thermometers and they suggested that the thermometer developed by Sack and Ghiorso (1991a, b) provided the best performance although the difference between $T_{Calculated}$ and T_{exp} can vary from –100°C to 100°C.

In conclusion, the existing Mg-Fe olivine-spinel thermometers do not reproduce experimental temperatures accurately. Caution is suggested when using these thermometers. For the above reason, the Al in olivine thermometer developed in this study may provide more accurate temperature estimations for olivine-spinel pairs.

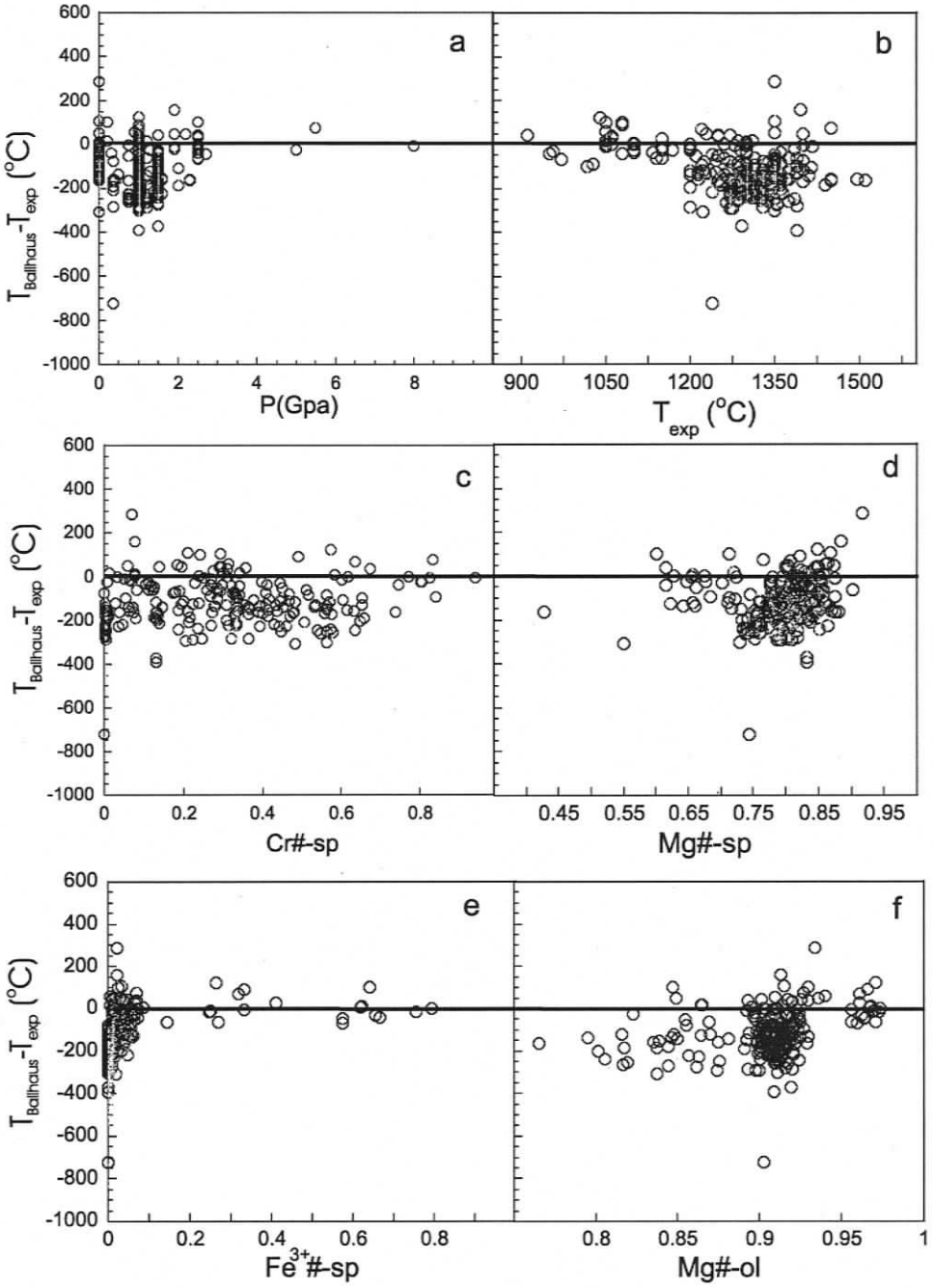

Figure 3.22 Plots of $T_{Ballhaus} - T_{exp}$ versus pressure (a), T_{exp} (b), Cr#-sp (c), Mg#-sp (d), Fe^{3+}#-sp (e), and Mg#-ol (f) for published experimental data and the experimental data from this study. Sources of published experimental data: Grove and Bryan, 1983; Tormey et al, 1987; Ballhaus et al, 1991; Bartels et al, 1991; Canil and Wei, 1992; Kinzler and Grove, 1992; Sisson and Grove, 1993; Kinzler, 1997; Robinson et al, 1998; Pickering-Witter and Johnston, 2000; Schwab and Johnston, 2001; Bulatov et al, 2002; Wasylenki et al, 2003; Witt-Eickschen and O'Neill, 2005.

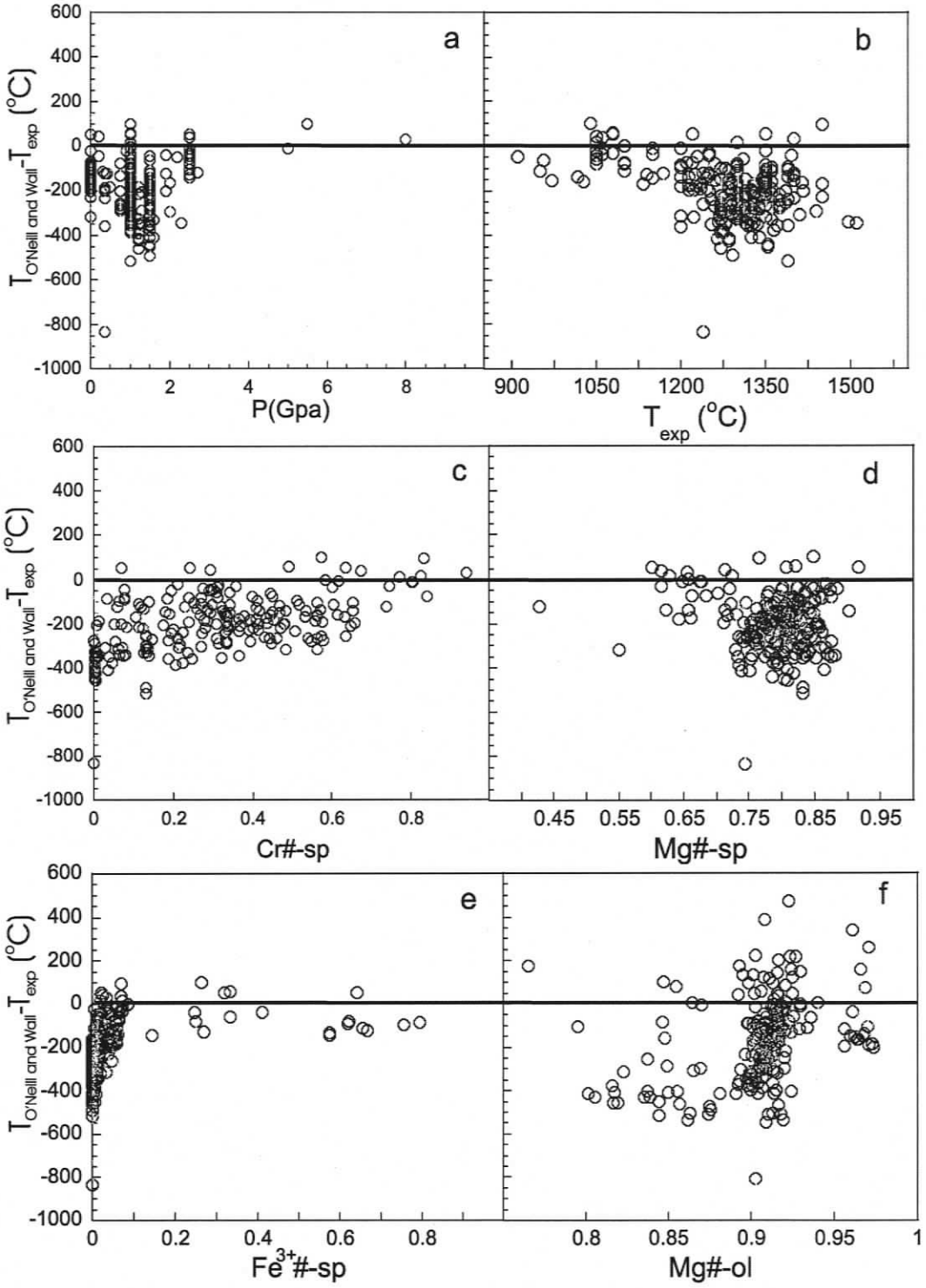

Figure 3.23 Plots of $T_{O'Neill\ and\ Wall} - T_{exp}$ versus pressure (a), T_{exp} (b), Cr#-sp (c), Mg#-sp (d), Fe^{3+}#-sp (e), and Mg#-ol (f) for published experimental data and the experimental data from this study. Data sources are the same as that for Figure 3.22.

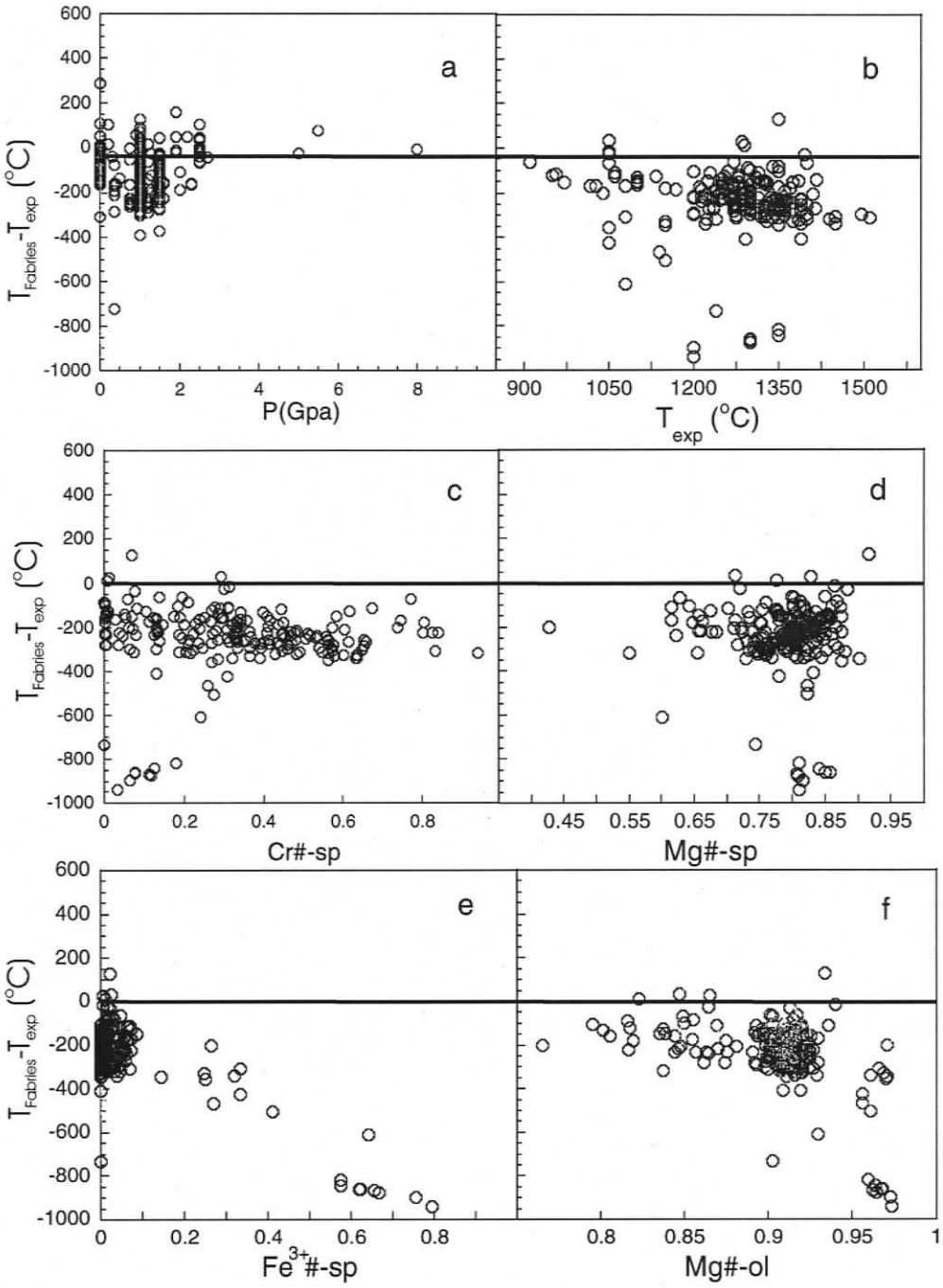

Figure 3.24 Plots of $T_{Fabries} - T_{exp}$ versus pressure (a), T_{exp} (b), Cr#-sp (c), Mg#-sp (d), Fe^{3+}#-sp (e), and Mg#-ol (f) for published experimental data and the experimental data from this study. Data sources are the same as that for Figure 3.22.

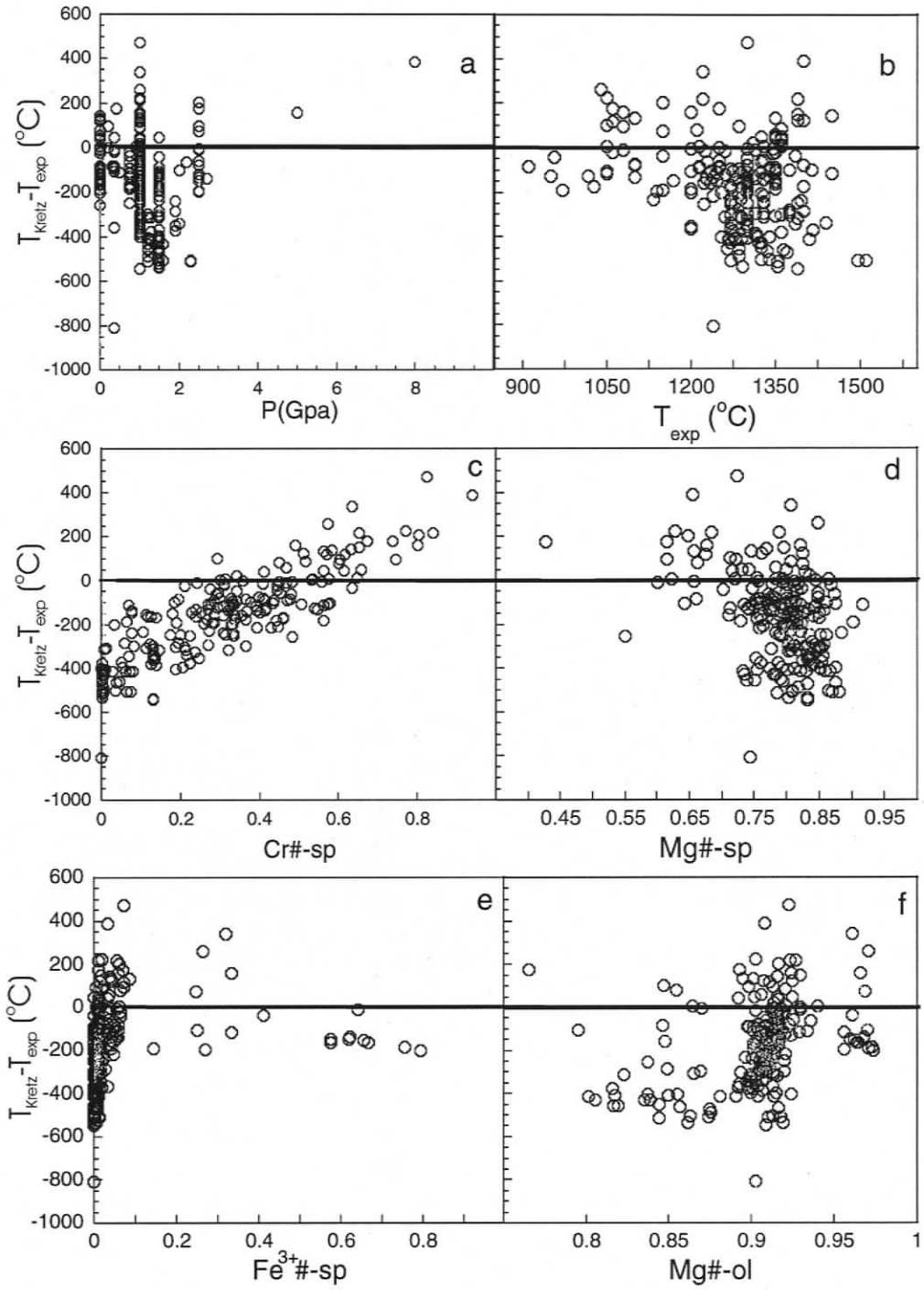

Figure 3.25 Plots of $T_{Kretz} - T_{exp}$ versus pressure (a), T_{exp} (b), Cr#-sp (c), Mg#-sp (d), Fe^{3+}#-sp (e), and Mg#-ol (f) for published experimental data and the experimental data from this study. Data sources are the same as that for Figure 3.22.

3.7.3 Future work

A major future work project would be to better understand the effect of Cr# of spinel on Al and Cr partitioning between olivine and spinel at a wider range of Cr#-sp and at different temperatures. More experiments need to be done at 1200°C, 1250°C, 1300°C and 1450°C using starting materials with different Cr_2O_3/Al_2O_3 ratios to grow spinel with lower and higher Cr# than those produced in this study. In addition, the ratio of Cr_2O_3/Al_2O_3 in the starting compositions needs to be expanded to expand the range of Cr# of spinel in experimental results so that the relation between Cr# of spinel and $D_{Al}^{ol/sp}$ and $D_{Cr}^{ol/sp}$ is fully understood over the entire Cr#-sp range of mantle rocks. An experimental study on Fe-Mg exchange between olivine and spinel needs to be carried out to precisely calibrate the relationship between $K_{DMg/Fe}^{ol/sp}$ and temperature and the relationship between $K_{DMg/Fe}^{ol/sp}$ and Cr#-sp.

3.8 Summary

Using experimental results at 100 kPa and 1250°C to 1450°C in natural basaltic compositions, two thermometers based on Al and Cr partitioning between olivine and spinel were developed.

The Al in olivine thermometer is given by:

$$T_{Al} = -10500 / \{[Ln(D_{Al}^{ol/sp}) - 0.98*(Cr\#\text{-}sp - 0.5)] - 0.75)\} \qquad (3.19)$$

where $D_{Al}^{ol/sp} = [Al_2O_3]^{ol}/[Al_2O_3]^{sp}$, $[Al_2O_3]^{ol}$ and $[Al_2O_3]^{sp}$ are the concentrations of Al_2O_3 in olivine and spinel, *Cr#-sp* is $Cr/(Cr+Al+Fe^{3+})$ in spinel, and *T* is in Kelvin. This thermometer is based on the assumption that the relationship between $\ln(D_{Al}^{ol/sp})$ and Cr#-sp is linear and relations at different temperatures are parallel to each other. The

calibration range for this thermometer is P = 100 kPa, T = 1250-1450°C, Cr#-sp = 0.07-0.63, Fe^{3+}#-sp = 0.02-0.05, and $\log(fO_2)$ = QFM – 1.8. The estimated precision for this thermometer is ±20°C. No significant pressure effect on Al partitioning between olivine and spinel was found. More work needs to be done to understand the relationship between $\ln(D_{Al}^{ol/sp})$ and Cr#-sp at different temperatures and to extrapolate this thermometer to a larger temperature and Cr#-sp range.

The Cr thermometer is given in the following form:

$$T_{Cr} = -9000/[\ln(D_{Cr}^{ol/sp}) - 0.02] \qquad (3.22)$$

where $D_{Cr}^{ol/sp} = [Cr_2O_3]^{ol}/[Cr_2O_3]^{sp}$, $[Cr_2O_3]^{ol}$ and $[Cr_2O_3]^{sp}$ are the concentrations of Cr_2O_3 in olivine and spinel, *Cr#-sp* is $Cr/(Cr+Al+Fe^{3+})$ in spinel, and *T* is in Kelvin. The calibration range for this thermometer is P = 100 kPa, T = 1250-1450°C, Cr#-sp = 0.2-0.63, Fe^{3+}#-sp = 0.02–0.05, and $\log(fO_2)$ = QFM – 1.8. The precision for the Cr thermometer is ±50°C. This study is only a preliminary study of Cr partitioning between olivine and spinel. Caution is suggested when using this thermometer.

Chapter 4

Application of the Al thermometer to natural samples

4.1 Introduction

The Al thermometer developed in Chapter 3, based on Al exchange between olivine and spinel, is applied to a suite of peridotite samples in this chapter. Samples studied are from the southern Canadian Cordillera, southeast Australia, Canary Islands, southern Africa, Tanzania, the Slave craton, Oman ophiolite, and the Southwest Indian Ridge. Based on the Al concentrations in olivine analyzed by LA-ICPMS and published Al concentration in spinel, temperatures are calculated using the Al thermometer (T_{Al}) for these samples. To test the feasibility of the Al thermometer when applied outside of the experimental calibration, the T_{Al} results are compared to the temperatures calculated using the thermometer based on Ca-Mg exchange between orthopyroxene and clinopyroxene (T_{BKN}, Brey & Köhler, 1990). The calculated T_{Al} for natural samples is generally lower than T_{BKN}. The difference might be caused by the inaccuracy of the thermometers or the different rates of Al diffusion in olivine and Ca diffusion in clinopyroxene and orthopyroxene. The latter model is validated by the different closure temperatures for Al exchange between olivine and spinel and Ca-Mg exchange between clinopyroxene and orthopyroxene in the same sample. Zoning profiles of Al and Ca in olivine for six xenolith samples were analyzed and they are used to access the thermal histories of the samples.

4.2 Sample suite studied

Seventeen mantle xenoliths from on- and off-craton settings, and six samples from the oceanic lithosphere are studied. The samples selected represent a broad range in Cr# of spinel (0.1 - 0.8), and include both garnet-spinel peridotites and spinel peridotites (Table 4.1).

4.2.1 Continental xenoliths

Continental xenoliths include nine spinel peridotite samples from off-craton settings and two spinel peridotite samples and six garnet-spinel peridotite samples from on-craton settings. The Cr#-sp in on-craton samples ranges from 0.09 to 0.44 (Table 4.1). The Cr#-sp in off-craton samples is higher, ranging from 0.39 to 0.84 (Table 4.1).

4.2.1.1 On-craton xenoliths

Sample FRB1530 is a graphite-bearing garnet-spinel lherzolite hosted in a kimberlite emplaced in the Kaapvaal craton, southern Africa between late Precambrian and Cretaceous (Canil and O'Neill, 1996). Sample 89-777 is a protogranular wehrlite from the Olmani cinder cone, Tanzania (Canil and O'Neill, 1996). Sample 89-661 is a garnet-spinel lherzolite from a Pleistocene Lashaine cinder cone, Tanzania (Canil and O'Neill, 1996). Samples 22-1, 22-4, 22-5, 25-4, and 26-11 are garnet-spinel peridotite xenoliths from the Jericho kimberlite, Slave Craton, Canada (Kopylova et al, 1999). Their mineralogy includes subhedral olivine and orthopyroxene and anhedral clinopyroxene, garnet and spinel (Kopylova et al, 1999).

4.2.1.2 Off-craton xenoliths

Samples JL1, JL8, TKN15, KLBR1, and SL47 are from four volcanic centers in the southern Canadian Cordillera: Summit Lake, Kostal Lake, Boss Mountain, and Jaques Lake (Brearley et al, 1984; Canil et al, 1990; Fujii and Scarfe, 1980). These samples are of xenoliths that are hosted in Neogene alkali basalt and basanite flows which were derived from the lithospheric mantle beneath the Canadian Cordillera (Peslier et al, 2002). In these samples, olivine ranges in size from 1 mm to 3 mm, orthopyroxene ranges in size from 1 mm to 4 mm, and clinopyroxene is less than 1 mm. Interstitial spinels are common but it also occurs as inclusion in olivine (sample SL47). Sample KLBR-1 was metasomatized indicated by the existence of phlogopite (Canil & Scarfe, 1988). Samples 84-402, 85-168, and 2905 are from basanitic lavas from southeast Australia. None of these samples show evidence of metasomatism.

4.2.2 Oceanic lithosphere samples

Samples of the oceanic lithosphere are represented by three samples from the Oman ophiolite, one abyssal peridotite from the Southwest Indian Ridge (SWIR), and two xenolith samples from Lanzarote, Canary Islands. Samples 2001OL24, 2004OL43, and 2001OL4 are spinel peridotite samples from the Wadi Bani Kharus section in the Nakhl-Rustaq block in the south-central part of the Oman ophiolite (personal communication, Coogan LA, University of Victoria, 2007). These samples contain spinel, olivine, clinopyroxene, and orthopyroxene. Olivine, the major mineral, has been serpentinized to varying extents. Sample 6K-DI-465-002 is from the Atlantis Bank segment of SWIR (Personal communication, Coogan LA, University of Victoria, 2007).

Table 4.1 Natural peridotite samples studied for application of the Al thermometer

Label	Type	Name	Texture	Location	Cr#-sp	Mg#-ol	Reference
FRB 1530	On-C	Gt-sp lher	coarse	S Africa	0.61	0.92	Canil and O'Neil, 1996
89-777	On-C	Weh	-	Tanzania	0.84	0.94	Canil and O'Neil, 1996
89-661	On-C	Gt-sp lher	coarse	Tanzania	0.63	0.93	Canil and O'Neil, 1996
22-1	On-C	Gt-sp lher	coarse	Jericho Kim	0.39	0.92	Kopylova et al, 1999
22-4	On-C	Gt-sp lher	coarse	Jericho Kim	0.74	0.92	Kopylova et al, 1999
26-11	On-C	Gt-sp lher	coarse	Jericho Kim	0.74	0.92	Kopylova et al, 1999
25-4	On-C	Gt-sp lher	coarse	Jericho Kim	0.74	0.92	Kopylova et al, 1999
22-5	On-C	Gt-sp lher	coarse	Jericho Kim	0.78	0.92	Kopylova et al, 1999
84-402	Off-C	Sp lher	equigranular	SE Australia	0.44	0.91	Canil and O'Neil, 1996
2905	Off-C	Sp lher	protogranular tabular	SE Australia	0.12	0.90	Canil and O'Neil, 1996
85-168	Off-C	Sp lher	granoblastic tabular	SE Australia	0.32	0.88	Canil and O'Neil, 1996
JL1	Off-C	Sp lher	-	BC JL	0.09	0.90	Canil et al, 1990; Fujii and Scarfe, 1982
JL8	Off-C	Sp lher	-	BC JL	0.14	0.91	Canil et al, 1990; Fujii and Scarfe, 1982
TKN15	Off-C	Sp lher	-	BC BS	0.10	0.90	Canil et al, 1990; Fujii and Scarfe, 1982
KLBR1	Off-C	Sp lher	-	BC KL	0.18	0.86	Canil et al, 1990
SL47	Off-C	Sp lher	-	BC SL	0.14	0.87	Canil et al, 1990; Brearley et al, 1984
LEIUG114018	Ocean	Sp Peri	-	Lanzarote	0.35	0.91	PersComm Coogan
LEIUG114019	Ocean	Sp Peri	-	Lanzarote	0.35	0.92	PersComm Coogan
2001OL24	Ocean	Sp Peri	-	Oman	0.49	0.91	PersComm Coogan
2001OL43	Ocean	Sp Peri	-	Oman	0.49	0.91	PersComm Coogan
2001OL4	Ocean	Sp Peri	-	Oman	0.53	0.92	PersComm Coogan
6K-DI-465-002	Ocean	Sp Peri	-	SWIR	0.22	0.90	Coogan et al, 2004

Mg#-ol: Mg/(Mg+Fe) ratio in olivine. On-C: On-craton xenolith. Off-C: Off-craton xenolith. Sp: spinel. Gt: garnet. Lher: lherzolite. Weh: wehrlite. Harz: harzburgite. Peri: peridotite. S Africa: South Africa. Kim: kimberlite. JL: Jaques Lake. BS: Boss Mountain. KL: Kostal Lake. SL: Summit Lake. SWIR: Southwest Indian Ridge. BC: British Columbia. Ocean: oceanic lithosphere. PersComm Coogan: personal communication with Coogan LA, University of Victoria.

Compared to the ophiolite samples, olivine in this sample is more extensively serpentinized.

Samples LEIUG114018 and LEIUG114019 are spinel peridotite xenoliths from Lanzarote, Canary Islands. Olivine in these two samples ranges from 1 to 6 mm in size. Spinels occur interstitially and as inclusions in olivine. No evidence of metasomatism was found.

4.3 Analytical methods

Aluminum and Ca contents in olivine crystals in the selected samples were determined using LA-ICPMS. San Carlos olivine was used as the external standard. The Al content in the San Carlos olivine was determined by both solution ICPMS and Electron Microprobe (EMP). The Ca content in San Carlos olivine was determined by EMP.

4.3.1 Standard development: Electron Microprobe and solution ICPMS

To test the homogeneity of San Carlos olivine, 22 analyses of major and minor elements across a piece (1 mm) of one olivine grain were determined using EMP. The EMP analyses were carried out with a CAMECA SX50 EMP at the University of British Columbia at a 15.0 kV acceleration voltage and a beam current of 39.8 nA with a 1-2 μm beam diameter. Analytical conditions were 20 s counting time on peak and background for all elements except for Al (60 s) and Cr (60 s). One standard deviation for all the analyses is 0.3-0.9wt% for the concentration of major elements (Mg, Si, and Fe). The Al content in San Carlos olivine determined using EMP is 97±20 ppm, and the Ca content in

San Carlos olivine determined using EMP is 509±65 ppm (the concentration is the average of the analyses and the analytical precision is represented by one standard deviation of the analyses).

Aluminum concentration of San Carlos olivine was also determined by solution ICPMS. A single olivine grain was carefully crushed and examined under a binocular microscope. About 100 mg of inclusion-free olivine were hand-picked under the microscope. These pieces were cleaned 13 times ultrasonically using deionized (DI) water for 15 minutes each time. The clean samples were dried in an oven at 100°C over night. About 30 mg of samples were weighed into a clean Teflon bottle and then digested in a mixture of 4.8 ml concentrated HCl, 4.2 ml concentrated HNO_3, and 6 ml concentrated HF at 180°C over a period of 11 days. The final solution was transferred to a 60 ml high density polyethylene (HDPE) bottle, with DI water and an internal standard (Be) added to the solution. Three series of solutions and a procedure blank were prepared. A series of external standards were made by adding different Al spikes to a diluted HNO_3 matrix.

Aluminum concentrations in these solutions were determined by solution ICPMS, using a VG PQ II+ ICPMS. Because ^{27}Al has a polyatomic interference from $^{12}C^{15}N$, a low RF power (900 Watts) was employed to reduce the background at mass 27. Data acquisition was performed in peak-jumping mode, acquiring individual intensity data for each analyte isotope during each mass spectrometer sweep. Isotopes ^{9}Be, ^{10}B, and ^{27}Al were monitored and the dwell time was 10 ms on ^{9}Be, 0.1 ms on ^{10}B, and 10 ms on ^{27}Al. The acquisition time for each sample was 16 s in total and a 2.5 minute rinse of 2% environmental HNO_3 acid between each sample was carried out. All data processing was

performed off-line. Operating conditions employed for the ICPMS instrument are listed in Table 4.2.

Aluminum concentration in San Carlos olivine obtained from solution ICPMS is 99±16 ppm (the concentration is the average of the analyses and the analytical precision is represented by one standard deviation of the analyses), which is very close to the results from EMP (97±20 ppm). A concentration of 99 ppm was used as the external standard concentration for LA-ICPMS analysis on the natural samples.

4.3.2 Analysis of aluminum and calcium in olivine: LA-ICPMS

The natural samples were analyzed in two sets. The first set of samples includes all the samples except LEIUG114018 and LEIUG114019. The samples were carefully crushed, minerals were separated, and olivine crystals were hand picked to optical purity under a binocular microscope. Each olivine grain was mounted in epoxy and polished. For each sample, about five olivine grains were analyzed by LA-ICPMS with one analysis at the center of each grain. The second set of analyses was aimed at examining Al zoning in olivine and included samples 22-4, 22-5, 25-4, 26-11, LEIUG114018 and LEIUG114019. Minerals were separated from samples 22-4, 22-5, 25-4, and 26-11, and only olivine crystals attached to spinel grains were selected. These were mounted in epoxy, and polished to expose the olivine-spinel contact. Samples LEIUG114018 and LEIUG114019 were studied using thin sections and olivine crystals adjacent to spinel grains were selected for analysis. The concentration of Al in olivine was measured as zoning profiles away from the olivine-spinel boundary.

Aluminum and Ca concentration of olivines in the first set of samples were determined using a VG PQ II+ ICPMS and a Merchantek UV LA Microprobe. Spot analyses with a spot size of 150 μm were employed. Low RF power (900 Watts) was used to reduce the background of ^{27}Al. The Al and Ca concentrations of olivine in the second set of samples were determined using a Thermo-Electron X7 ICPMS and a Merchantek UV LA Microprobe. In the second set of analysis, spot analysis with a 100 μm spot size was employed for samples 22-4, 22-5, 25-4, and 26-11. A scanned line profile (rather than a spot) was used for samples LEIUG114018 and LEIUG114019, because these two samples are standard thin sections of only 30 microns thickness. The scanning speed was 0.01 mm/s. For both sets of analysis, ^{57}Fe was used as the internal standard, and data acquisition was performed in peak-jumping mode, acquiring individual intensity data for each analyte isotope during each mass spectrometer sweep. The dwell time on each mass was 10 ms. Three analyses on the external standard (San Carlos olivine) were carried out at the beginning and the end of each set of sample analysis and between every 10 analyses. The external standard was also analyzed before and after changing samples. Operating conditions employed for the first and second set of analysis using LA-ICPMS are listed in Table 4.2.

Before analyzing the olivine samples, the gas background on all the analytes was collected for about 20 seconds (e.g. Figure 4.1). The laser was then switched on and the signal for the samples was collected for about 5-40 seconds (e.g. Figure 4.1). The raw counts per second (cps) for selected background and selected stable signal were exported and all data manipulations were done manually off-line.

Table 4.2 Optimized instrumental measurement settings for solution ICPMS analysis of San Carlos olivine and LA-ICPMS.

Instrumental settings	Solution ICPMS	LA-ICPMS	
		First set	Second set
ICPMS	Thermo-Electron X7	VG PQ II+ ICPMS	Thermo-Electron X7
Forward RF power (Watts)	900	900	1435
Nebuliser gas flow (L/min)	1.3	0.58	0.84
Carrier He gas flow (L/min)	2.9	1.3	1.0
Auxiliary Ar gas flow (L/min)	0.98	0.98	0.80
Cooling Ar gas flow (L/min)	15	15	13
Isotopes monitored	^{9}Be, ^{10}B, ^{27}Al	^{10}B, ^{27}Al, ^{44}Ca, ^{57}Fe	^{10}B, ^{27}Al, ^{28}Si, ^{44}Ca, ^{57}Fe

First set: first set of analyses. Second set: second set of analyses. The first set of analyses is for analyzing the Al concentration in olivine from natural samples. The second set of analyses is for examining the zoning of Al and Ca in olivine for selected samples.

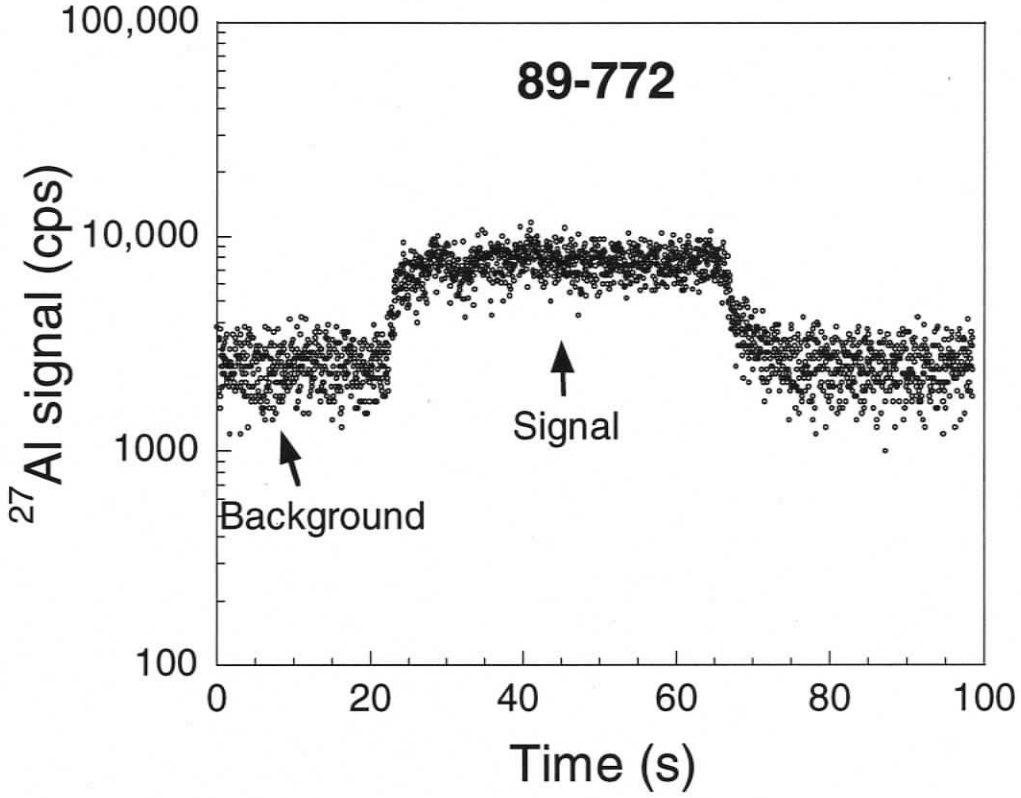

Figure 4.1 Time-resolved laser ablation signals for ^{27}Al in olivine in sample 89-772. Laser ablation analysis was done in time-resolved mode. Cps: counts per second. A 25 s background was collected while the laser was off. This was followed immediately by turning on the laser and ablating the sample, generating a time-dependent signal. Measurements were made for 40 s and the laser was turned off. Background was collected for another 35 s.

4.3.3 Analytical error for LA-ICPMS

Aluminum concentrations in olivines for all samples studied range from 3.3 ppm to 179 ppm (Table 4.3 and Table 4.5). Based on one standard deviation of the Al concentration in San carlos olivine, the analytical precision is about 5 ppm at 100 ppm concentration. The analytical precision at lower Al concentrations is not known. However, for sample 22-5, which contains 15-16 ppm Al, the difference between Al concentrations from different analyses of one olivine grain is likely to be caused by the analytical precision since no zoning of Al in this olivine grain is observed (Figure 4.6). This difference (1 ppm) provides an upper limit for analytical precision at 15 ppm Al. The Ca contents in olivine range from 220 ppm from 680 ppm (Appendix 3). Based on the Ca concentrations in San Carlos olivine, the analytical precision is 15 ppm at 500 ppm Ca.

4.4 Results

4.4.1 Aluminum concentration in olivine

Olivines from on-craton xenolith samples (22-1, 22-4, 22-5, 26-11, FRB1530, and 89-777) generally have the lowest Al concentrations (3.4-14.2 ppm) of all the samples studied, except sample 89-661, a garnet-spinel lherzolite on-craton xenolith from Tanzania, in which olivine contains about 56 ppm Al (Table 4.3 and Table 4.5). For these on-craton samples, the variation of Al contents in different grains for one sample is usually within 3 ppm. Olivines from spinel peridotite xenoliths from off-craton settings have a wide range of Al contents: 13-163 ppm, and the Al contents of different olivine grains from one sample vary by up to 65% (Table 4.3). Of the oceanic lithosphere

samples, samples 2001OL4, 2001OL24, 2001OL43, and 6K-DI-465-002 have low Al contents in olivine (8.5-28.7 ppm) and the Al contents for different grains from the same sample vary by up to 106% (Table 4.3). Samples LEIUG114018 and LEIUG114019 have Al contents in olivine ranging 59-75 ppm and 85-132 ppm respectively within the same olivine grain (Table 4.5).

4.4.2 Application of the Al thermometer to natural samples

To test the Al thermometer, it was applied to all of the natural samples studied. For each grain, T_{Al} was calculated and ranges from 630°C to 1080°C (Table 4.4). Calculated T_{Al} for on-craton xenoliths has a wide range: 630-1000°C (Table 4.4). Calculated T_{Al} for off-craton spinel peridotite xenoliths ranges from 810°C to 1080°C. Calculated T_{Al} for samples from oceanic lithosphere ranges from 730°C to 840°C and is characterized by a large variation in calculated temperatures (29-60°C) between different grains from the same sample. The calculated T_{Al} values for all the natural samples appear to be geologically reasonable.

Table 4.3 Aluminum contents of different olivine grains (1-5) from the first set of samples and corresponding T_{Al} values.

Sample	Type	Location	Al (ppm)							T_{Al} (°C)						
			1	2	3	4	5	Ave	1σ	1	2	3	4	5	Ave	2σ
FRB1530	On-C	S Africa	13.4	12.3	11.8	11.6		12.3	0.8	798	790	785	783		789	14
89-777	On-C	Tanzania	12.2	13.0	12.9	12.5	12.7	12.7	0.3	900	908	908	904	905	905	7
89-661	On-C	Tanzania	59	55	57	58	51	56	3.1	1003	992	998	1000	981	995	17
22-1	On-C	Jericho Kim	5.3	5.3	4.7	3.3	5.1	4.8	0.9	675	675	664	635	672	664	34
22-4	On-C	Jericho Kim	9.4	9.6	8.3			9.1	0.7	829	832	815			825	18
26-11	On-C	Jericho Kim	9.9	8.5				9.2	0.9	836	819				828	23
25-4	On-C	Jericho Kim	9.2	10.1	12.5			10.6	1.7	829	840	865			845	38
22-5	On-C	Jericho Kim	14.4	13.6	14.3	13.7		14.0	0.4	902	895	901	895		898	7
84-402	Off-C	SE Australia	90	88	92	87	88	89	2	1008	1003	1011	1003	1004	1006	8
2905	Off-C	SE Australia	111	102	108	109	114	109	5	994	981	990	991	998	991	13
85-168	Off-C	SE Australia	135	134	141	131	119	132	8	1060	1058	1067	1054	1039	1055	21
JL1	Off-C	BC JL	34.9	28.9	32.4	29.5	40.3	33	5	839	817	830	819	856	832	32
JL8	Off-C	BC JL	29.9	47.8	28.9	32.5	33.4	35	8	824	880	820	833	837	839	48
TKN15	Off-C	BC BS	52	46	51	49	58	51	4	886	872	884	879	900	884	20
KLBR-1	Off-C	BC KL	159	208	155	142	148	162	26	1075	1123	1070	1056	1062	1077	53
SL47	Off-C	BC SL	153	165	165	179		166	11	1071	1058	1085	1071		1071	22
2004OL24	Ocean	Oman	9.2	8.0	10.7			9.3	1.4	743	729	758			743	29
2001OL43	Ocean	Oman	15.3					15		791					791	
2001OL4	Ocean	Oman	20.6	13.8	15.1	11.2	10.0	14	4.2	833	788	798	766	755	788	61
6K-465-002	Ocean	SWIR	27.8	23.0	31.7	17.3	27.8	26	6	824	803	839	772	824	812	52

On-C: On-craton xenolith. Off-C: Off-craton xenolith. Ocean: oceanic lithosphere. S Africa: South Africa. Kim: kimberlite. BC: British Columbia. JL: Jaques Lake. BS: Boss Mountain. KL: Kostal Lake. SL: Summit Lake. SWIR: Southwest Indian Ridge. Ave: average. 1σ: one standard deviation. 2σ: two standard deviation.

4.5 Comparison between the Al thermometer and the two pyroxene solvus thermometer

To test the Al thermometer, T_{Al} for natural samples need to be compared to temperatures calculated using other thermometers. Since existing versions of the thermometer based on Mg and Fe exchange between olivine and spinel were found to poorly reproduce published experimental results (Chapter 3), this thermometer is not used to test the Al thermometer. The thermometer based on Ca-Mg exchange between orthopyroxene and clinopyroxene (T_{BKN}, Brey and Köhler, 1990) is used here. Due to the slow exchange of Ca-Mg between orthopyroxene and clinopyroxene, the equilibrium distribution of these elements is not easily affected by late thermal events such as heating of xenoliths by magma (Brey and Köhler, 1990). Another advantage of this thermometer is that it is not significantly affected by pressure (Brey and Köhler, 1990). Due to the lack of suitable geobarometers for spinel peridotites, the pressures of spinel peridotite xenoliths in this study are not accurately known and thus using a pressure insensitive thermometer is critical.

The pressures for spinel-garnet peridotites are calculated using a combination of T_{BKN} and the garnet-orthopyroxene Al-exchange barometer of Brey and Köhler (1990) (P_{BKN}). For spinel peridotites, the barometer based on Ca exchange between olivine and clinopyroxene (P_{BK}, Köhler and Brey, 1990) is combined with T_{BKN} in an attempt to determine the pressure for these samples. However, this temperature sensitive barometer yields unreasonable pressures (e.g. -2 GPa). This indicated that T_{BKN} is inappropriate temperature for calculating P_{BK}. Thus, the pressures for all spinel peridotite xenoliths are assumed to be 1.5 GPa. For samples from the oceanic lithosphere, the pressures of spinel

Table 4.4 Pressure-temperature conditions of the mantle peridotite samples.

Label	Type	Location	P (GPa)	T_{BKN}	T_{Alave}	2σ
FRB 1530	On-C	S Africa	2.2	715	789	14
89-777	On-C	Tanzania	1.5	1080	905	7
89-661	On-C	Tanzania	1.5	1041	995	17
22-1	On-C	Jericho Kim	2.6	674	664	34
22-4	On-C	Jericho Kim	4	824	825	18
26-11	On-C	Jericho Kim	4.5	947	828	23
25-4	On-C	Jericho Kim	5.5	993	845	38
22-5	On-C	Jericho Kim	4.1	930	898	7
84-402	Off-C	SE Australia	1.5	1028	1006	8
2905	Off-C	SE Australia	1.5	1004	991	13
85-168	Off-C	SE Australia	1.5	1187	1055	21
JL1	Off-C	BC JL	1.5	1001	832	32
JL8	Off-C	BC JL	1.5	836	839	48
TKN15	Off-C	BC BS	1.5	958	884	20
KLBR1	Off-C	BC KL	1.5	1122	1077	53
SL47	Off-C	BC SL	1.5	1094	1071	22
LEIUG114018	Ocean	Lanzarote	1.5	985	956	29
LEIUG114019	Ocean	Lanzarote	1.5	953	1023	64
2001OL24	Ocean	Oman	0.5	986	743	29
2001OL43	Ocean	Oman	0.5	846	791	
2001OL4	Ocean	Oman	0.2	866	788	61
6K-DI-465-002	Ocean	SWIR	0.5	930	812	52

On-C: On-craton xenolith. Off-C: Off-craton xenolith. Ocean: oceanic lithosphere. S Africa: South Africa. Kim: kimberlite. BC: British Columbia. JL: Jaques Lake. BS: Boss Mountain. KL: Kostal Lake. SL: Summit Lake. SWIR: Southwest Indian Ridge. Temperatures are in °C. 2σ: two standard deviation. T_{Alave}: the average of the calculated T_{Al} from different analyses for the same sample.

peridotites from Oman ophiolite are calculated according to the depths of the samples based on geological mapping, and the pressure of the spinel peridotite from SWIR is assumed to be 0.5 GPa (personal communication, Coogan LA, University of Victoria, 2007).

In the next section, temperatures calculated using the two pyroxene thermometer are compared to temperatures calculated using the Al thermometer for all natural samples. Samples with Cr#-sp outside of the experimental calibration range (Cr#-sp > 0.6) are discussed to test the feasibility of the extrapolation of the Al thermometer to Cr#-sp range higher than the calibrated range.

4.5.1 Comparison between the Al thermometer and the two pyroxene solvus thermometer

For all of the samples with Cr#-sp within the experimental calibration range (six oceanic lithosphere samples and ten continental xenolith samples), T_{BKN} increases with increasing T_{Al}, and falls in the range of T_{Al} – 100°C and T_{Al} + 200°C except for one sample that has T_{BKN} 240°C higher than T_{Al} (Figure 4.2). For those samples with T_{BKN} = T_{Al} – 100°C - T_{Al} + 200°C, thirteen samples have T_{BKN} 0-200°C higher than T_{Al}, and two samples have T_{BKN} 0-100°C lower than T_{Al} (Figure 4.2). For samples outside the experimental calibration range (seven continental xenolith samples), T_{BKN} also falls in the range of T_{Al} – 100°C and T_{Al} + 200°C. Six samples have T_{BKN} 0-200°C higher than T_{Al} (Figure 4.2), and only one sample has T_{BKN} 0-100°C lower than T_{Al} (Figure 4.2).

To investigate the difference between T_{BKN} and T_{Al}, $T_{BKN} - T_{Al}$ is plotted against pressure, Cr#-sp, Mg#-sp (Mg/(Mg+Fe) ratio of spinel), Mg#-ol, T_{Al} and T_{BKN} in Figure

4.3. No systematic relations between $T_{BKN} - T_{Al}$ and any of these parameters exist. Taking the temperature range (660 °C - 1080°C) and Cr#-sp range (0.09 - 0.84) of these samples into consideration, the extrapolation of the Al thermometer to low temperature and high Cr#-sp appears to be feasible.

There are several possible reasons for the difference between T_{Al} and T_{BKN}.

1) Inaccuracy of T_{BKN}. The thermometer calibrated by Brey and Köhler (1990) based on Ca-Mg exchange between orthopyroxene and clinopyroxene may not be accurate since this thermometer was not calibrated in the natural system (Brey and Köhler, 1990). The accuracy of T_{BKN} can be tested by applying this thermometer to experiments that are carried out in the natural system and have coexisting orthopyroxene and clinopyroxene in the run products.

2) Inaccuracy of the Al thermometer when applied to temperatures lower than the calibration range: the Al thermometer is only calibrated within the temperature range of 1250-1450°C. The extrapolation of the thermometer to lower temperatures is likely to lead to some error (Figure 4.4).

3) Kinetic effects: rates of Al exchange between olivine and spinel might be different from those for Ca-Mg exchange between orthopyroxene and clinopyroxene. The olivine-spinel pair or clinopyroxene-orthopyroxene pair, or both may not reach equilibrium and the difference between T_{BKN} and T_{Al} might reflect that the equilibrium of Al olivine-spinel exchange and the equilibrium of Ca-Mg clinopyroxene-orthopyroxene exchange are affected to different extents by the late thermal events.

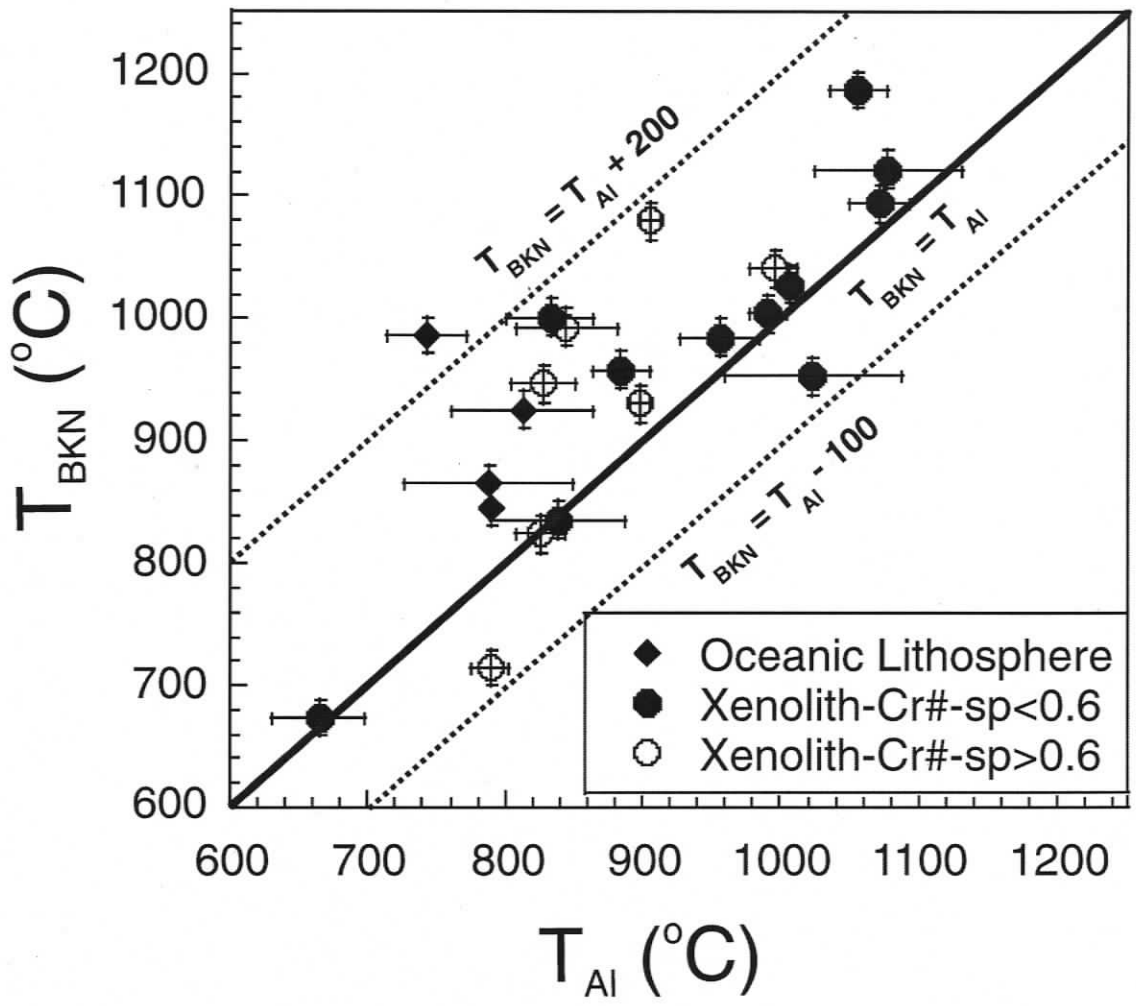

Figure 4.2 Plot of T_{BKN} versus T_{Al} for the studied natural samples. Xenolith: xenolith samples from on- and off-craton settings. Oceanic Lithosphere: samples from the oceanic lithosphere. Samples from the oceanic lithosphere all have Cr#-sp < 0.6. The T_{Al} value is represented by the symbol and the error bar for T_{Al} represents the two standard deviation value of the T_{Al} calculated for different Al in olivine analyses from the same sample. The error bar of T_{BKN} shown is 15°C, which is based on how well the T_{BKN} reproduces the experiments of Brey and Köhler (1990).

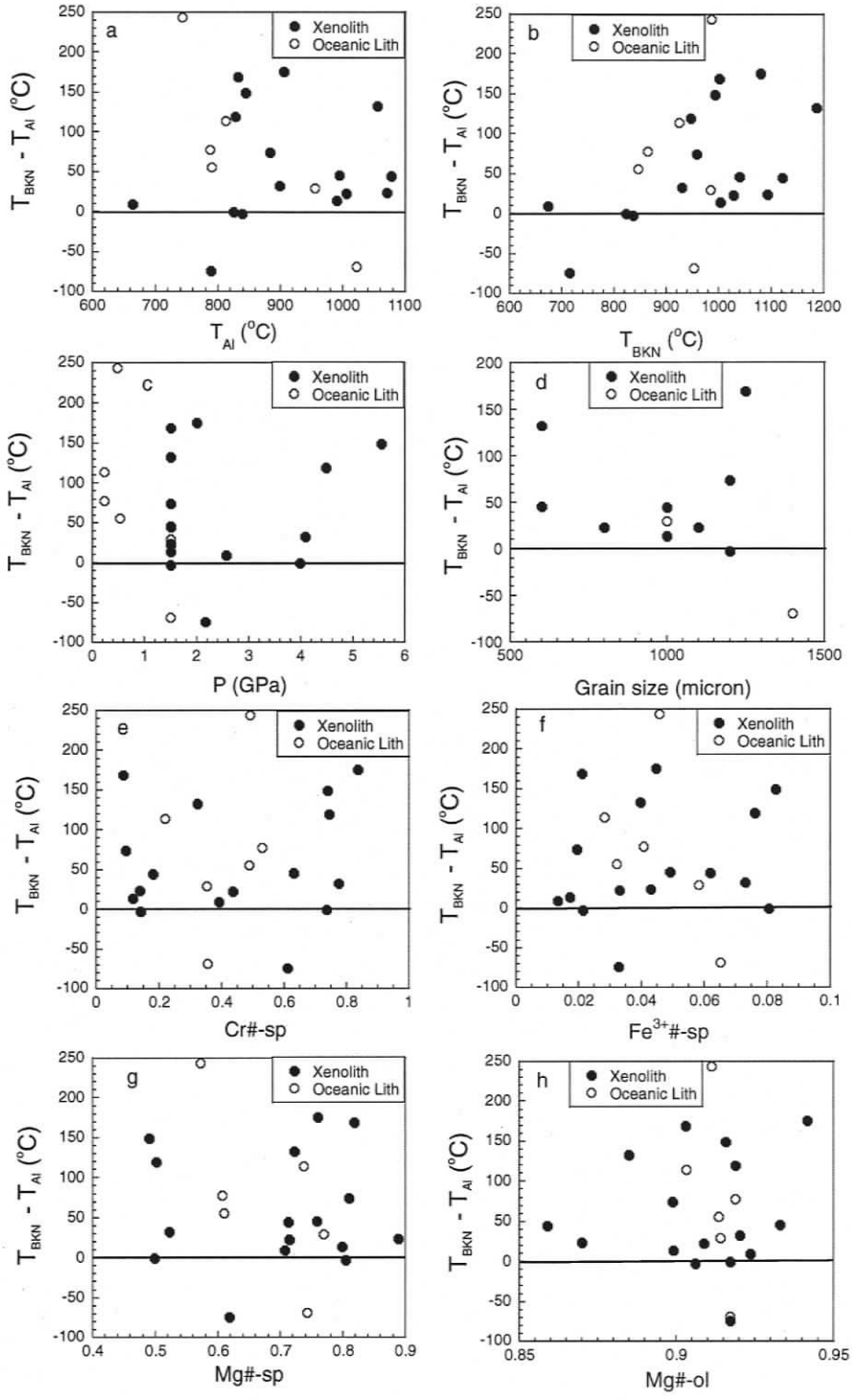

Figure 4.3 Plot of $T_{BKN} - T_{Al}$ versus T_{Al} (a), T_{BKN} (b), P (c), Grain size (d), Cr#-sp (e), Fe^{3+}#-sp (f), Mg#-sp (g), and Mg#-ol (h) for natural samples. Fe^{3+}#-sp: Fe^{3+}/ ($Cr+Al+Fe^{3+}$) in spinel. P: pressure. $T_{BKN} - T_{Al}$: temperature difference between T_{BKN} and T_{Al}. Oceanic Lith: Oceanic Lithosphere.

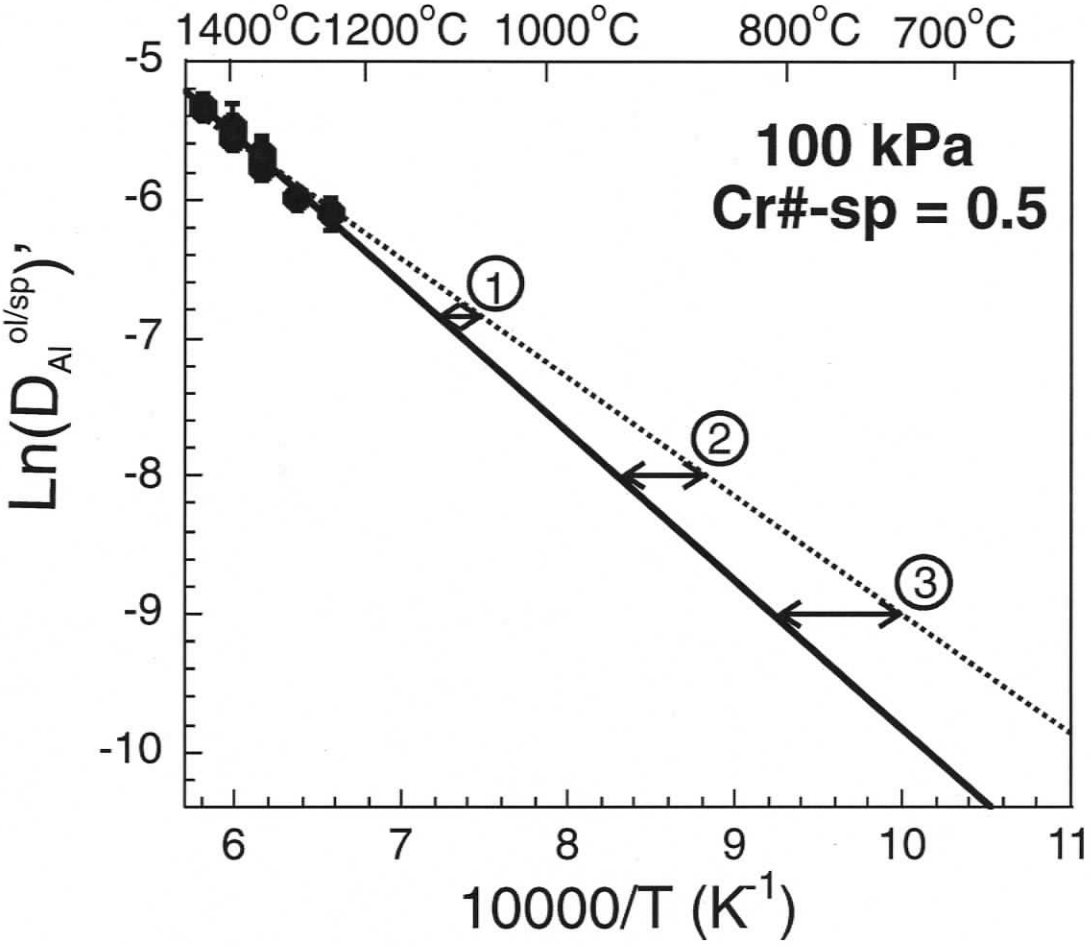

Figure 4.4 Illustration of the extrapolation of the Al thermometer to low temperatures. Symbols represent the experimental results from Chapter 3 and are the same as symbols for Figure 3.8. Solid line is the linear regression of the data. Dashed line is drawn by hand through data points. It represents the possible relations between $\ln(D_{Al}^{ol/sp})$' and 10000/T. The difference between the solid line and the dashed line (①, ②, and ③) in this diagram represents the possible error of the Al thermometer when it is applied to temperature conditions lower than the calibration range of Al thermometer (1250°C - 1450°C). As shown in this figure, the possible error of T_{Al} increases with decreasing temperature (③ > ② > ①).

4.5.2 Is aluminum diffusion in olivine faster than calcium diffusion in orthopyroxene and/or clinopyroxene?

For mantle samples that have experienced later thermal events, the equilibrium of element exchange between mineral pairs may have been disturbed because subsolidus diffusion is thermally activated. The temperature dependence of the diffusion coefficient of an element in a mineral is defined by an Arrhenius relationship:

$$D_{Diff} = D_{Diff0} * exp(-E/RT) \qquad (4.1)$$

where D_{Diff} is the diffusion coefficient at absolute temperature T, R is the gas constant, E is the activation energy for the diffusion process, and D_{Diff0} is the diffusion coefficient at infinite temperature conditions.

For a system in which a mineral containing trace amounts of element i coexists with a semi-infinite reservoir of element i, as the temperature decreases, the element concentration at the edge of the mineral starts to change to maintain equilibrium. At sufficiently high temperatures, the process of solid state diffusion is rapid enough to maintain thermodynamic equilibrium (Dodson, 1976; Figure 4.5 between Ts and T_0). At lower temperatures, diffusion becomes too slow to maintain complete equilibrium, and during cooling the distribution of an element is eventually "frozen" (Figure 4.5 at T less than T_1). The temperature derived from an element concentration in this scenerio is known as the "closure temperature" (T_c). Dodson (1973) derived the solution for the T_c of whole grains for a trace element equilibrating with an infinite reservoir of this element:

$$T_c = R/[Eln(A\tau D_0/\alpha^2)] \qquad (4.2)$$

where α is a characteristic diffusion size (here equal to grain size), A is a numerical constant depending on the geometry, and τ is the time constant with which the diffusion

coefficient D_{Diff} diminishes by a factor e^{-1} and is given as

$$\tau = -RT_c^2/[E(dT/dt)] \quad (4.3)$$

where dT/dt is the cooling rate. As seen in Equation (4.2) and (4.3), the closure temperature is dependent on the cooling rate and the kinetic properties of the element in the mineral of interest. Aluminum is a trace component in olivine and is a major element in spinel. For olivine-spinel mineral pairs that are adjacent to each other, the rim of spinel can store sufficient Al for it to act as an approximate semi-infinite reservoir. Therefore, the closure temperature of Al exchange between olivine and spinel is considered to be mainly dependent on the cooling rate and Al diffusion in olivine.

All minerals in the same rock have experienced the same cooling rate. Thus, the closure temperature for an element that has faster diffusion rate will be lower than that for the element that has lower diffusion rate. An ophiolite is a sequence of rock that is interpreted as representing the oceanic crust and upper mantle sections that have been obducted onto continental crust, and samples from the ophiolite have experienced cooling (Dilek, 2003). In the mid-ocean ridge, peridotites formed from the residue of mantle melting also experienced cooling down during ascent to the sea floor. Therefore, for samples from the Oman ophiolite and the SWIR, the calculated temperatures using the Al thermometer and T_{BKN} must represent the closure temperature for cation exchange during cooling. In this study, T_{Al} is found to be about 100-240°C lower than T_{BKN} for these samples (Table 4.4). This might suggest that Al diffusion in olivine is faster than Ca diffusion in clinopyroxene and/or orthopyroxene. Detailed investigation on the geometry and size of the olivine, clinopyroxene and orthopyroxene grains in these samples should be carried out to confirm this conclusion.

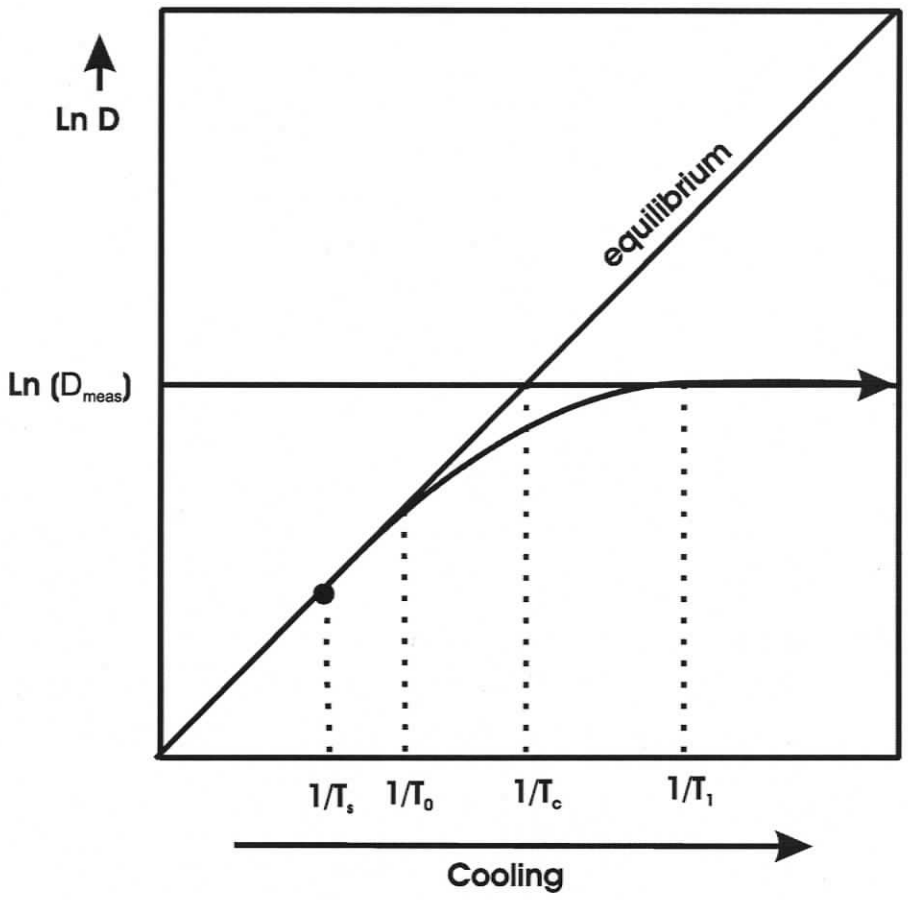

Figure 4.5 Illustration of the relationship between the partition coefficient (D) for an element between two phases with temperature during cooling (modified from Coogan et al, 2002). D_{meas}: measured D value. T_s: starting temperature. T_0: the temperature after which the diffusion becomes too slow to maintain equilibrium. T_1: temperature at which the diffusion profile is already frozen. T_c : closure temperature. As shown in this diagram, the D_{meas} at $T \leq T_1$ is always the same.

4.6 Zoning of aluminum and calcium in olivine and determination of thermal histories

When coexisting olivine and spinel that are originally in equilibrium undergo heating or cooling, the equilibrium condition is disturbed and the Al content in olivine will increase or decrease to regain equilibrium. The Al concentrations at the edge of olivine start to increase or decrease first and diffusion will maintain equilibrium by homogenizing the concentration gradient of Al in olivine between the edge and the core (Chakraborty, 2006). However, the new equilibrium may not be fully reached and the olivine grain develops Al zoning profiles, the "shape" of which records the details of the thermal history (Dodson, 1973; 1976). Based on the Al thermometer, if the Al content of an olivine decreases from the rim to the core, it suggests that Al diffused into the olivine and the sample has been heated, and vice versa. Calcium exchange between olivine and clinopyroxene is temperature dependent and Ca diffuses into olivine as the temperature increases (Köhler and Brey, 1990). Therefore, if the Ca content in olivine decreases from the rim to the core, it suggests that the sample has been heated, and vice versa.

Aluminum and Ca contents for olivine from the second set of analysis aimed at examining the zoning of Al and Ca in olivine are given in Table 4.5 and Appendix 4. Zoning profiles of Al and Ca in olivine for samples 22-1, 22-4, 25-4, and 26-11 from the Jericho Kimberlite, Slave Craton are shown in Figures 4.6 and 4.7.

Table 4.5 Aluminum concentrations in olivine from the second analytical session designed to examine the zoning of Al in olivine.

LEIUG114018		LEIUG114019		22-4		22-5		25-4		26-11	
d (μm)	Al (ppm)	d (μm)	Al (ppm)	d (μm)	Al (ppm)	d (μm)	Al (ppm)	d (μm)	Al (ppm)	d (μm)	Al (ppm)
150	74.5	62	132	150	13.5	100	16.1	90	13.8	130	10.8
200	70.9	620	85	330	11.6	230	15.9	250	12.9	420	11.1
400	61.4	720	88	330	11.7	525	15.2	480	12.4	1040	12.2
550	62.8	1000	103	500	11.6	730	16.2	520	11.3		
900	58.9			570	11.5	920	15.0	675	10.9		
				780	11.4	1120	16.0				
				610	11.5	1400	15.1				

"d" is the distance between the olivine-spinel boundary and the center of the analysis spot. "Al" is the corresponding Al concentration from different analysis spots.

For sample 22-5, no obvious zoning of Al in olivine is observed (Figure 4.6b). For samples 22-4, 25-4, and 26-11, the maximum difference between Al contents at different analysis spots in the olivine grain (2-3 ppm) is larger than the analytical precision (≤1 ppm). Therefore, the zoning of Al in olivine for these samples can be used to infer the thermal history of the samples. Aluminum content increases towards the olivine-spinel rim for samples 22-4 and 25-4 (Figure 4.6a and c), suggesting that these two samples have been heated at a late stage in its history prior to eruption. The difference between the highest T_{Al} and the lowest T_{Al} is about 25-30°C for these two samples. For sample 26-11, the Al concentration in olivine decreases towards the rim, suggesting a cooling process prior to eruption.

The maxium difference between different Ca in olivine analyses in the same olivine grain for these four samples is higher than the precision. The zoning of Ca in olivine is also used to determine the thermal histories of these samples (Figure 4.7). Calcium concentration in olivine from samples 22-4 and 25-4 increases towards the rim (Figure 4.7a and c), suggesting a heating process prior to their eruption. Calcium concentration in olivine from samples 26-11 decreases towards the rim (Figure 4.7d), suggesting a cooling process prior to its eruption. Thermal histories of samples 22-4, 25-4, and 26-11 inferred from the zoning of Ca in olivine are consistent with those inferred from the zoning of Al in olivine. For sample 22-5, the Ca content in olivine increases towards the rim (Figure 4.7b), suggesting that this sample was heated before its eruption. However, zoning of Al in olivine is not observed (Figure 4.6b). This may suggest that the heating process was not intense enough to affect the equilibrium of Al exchange between olivine and spinel. Calcium diffusion in olivine may be faster than Al diffusion in olivine.

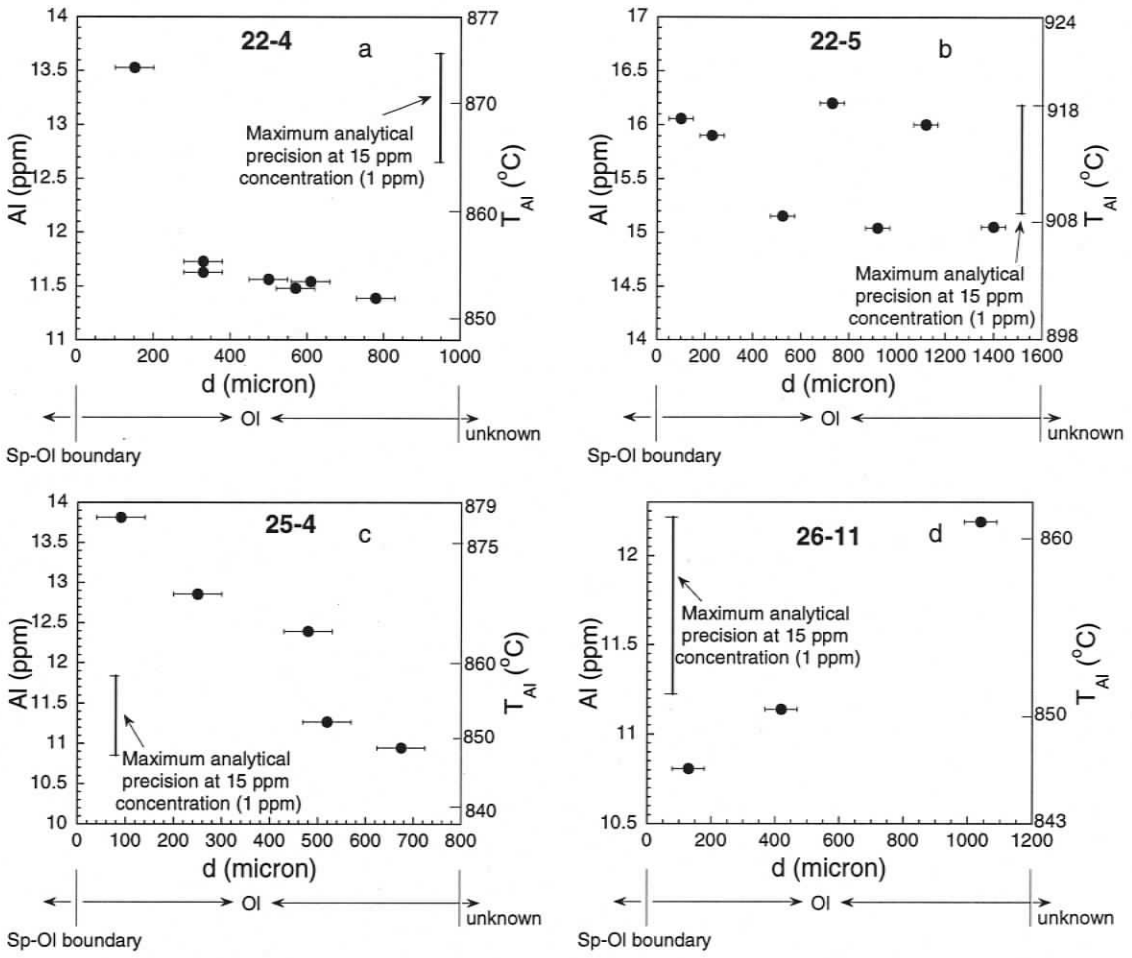

Figure 4.6 Zoning of Al in olivine for samples 22-4 (a), 22-5 (b), 25-4 (c), and 26-11 (d). The Al contents (ppm) are shown on the left vertical axis and corresponding T_{Al} values are shown on the right vertical axis. d: the distance to the spinel-olivine boundary. Sp: spinel. Ol: olivine. The symbol represents the center of each analysis spot and the error bar represents the radius of the analysis spot. Overlap of "d" for some analysis spots is because that these analyses in olivine are at different directions away from the olivine-spinel boundary. The positions of the cores of the olivine crystals are unknown because minerals were separated from the samples. Analytical precision is less than 1 ppm at 15 ppm concentration.

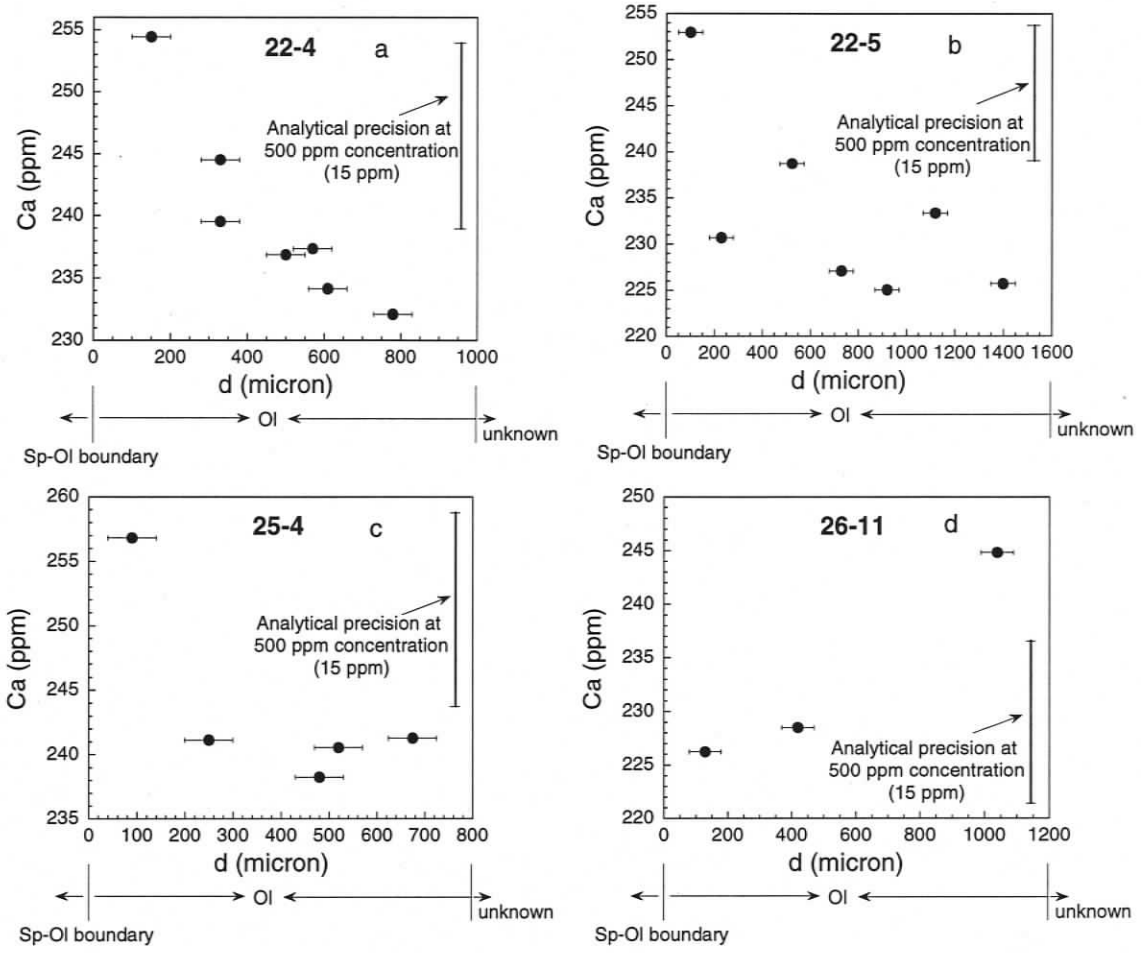

Figure 4.7 Zoning of Ca in olivine for samples 22-4 (a), 22-5 (b), 25-4 (c), and 26-11 (d). The Ca contents (ppm) are shown on the left vertical axis. d: the distance to the spinel-olivine boundary. Sp: spinel. Ol: olivine. The symbol represents the center of each analysis spot and the error bar represents the radius of the analysis spot. Overlap of "d" for some analysis spots is because these analyses in olivine are at different directions away from the olivine-spinel boundary. The positions of the cores of the olivine crystals are unknown because minerals were separated from the samples. Analytical precision of Ca concentration in olivine is 15 ppm at Ca concentration of 500 ppm.

Zoning of Al and Ca in olivine in sample LEIUG114018 is shown in Figures 4.8a and b. The difference between Al and Ca contents at different spots is larger than the analytical precision. This olivine crystal is at the edge of the thin section and only the position where olivine and spinel attach is known (d = 0 in Figures 4.8a and b). Both Al content and Ca content in olivine in sample LEIUG114018 increase towards the rim (Figures 4.8a and b) suggesting that this sample was heated at a late stage of its thermal history prior to eruption. The difference between the highest T_{Al} and the lowest T_{Al} is about 35°C.

Zoning of Al and Ca in olivine for sample LEIUG114019 is shown in Figures 4.8c and d. This olivine crystal is between a spinel crystal and an orthopyroxene crystal. The Al and Ca contents of olivine near the olivine-spinel boundary are higher than that in the core of the olivine (Figures 4.8c and d). Also, Al and Ca concentrations increase towards the olivine-orthopyroxene boundary. These data suggest that this sample was also heated at a late stage in its history prior to eruption. The calculated difference in temperature using the Al thermometer between the core and the rim is about 70°C.

In summary, the zoning of Al and Ca in olivine is used to infer the thermal histories of six xenolith samples and it indicates that most of these samples have been heated prior to eruption.

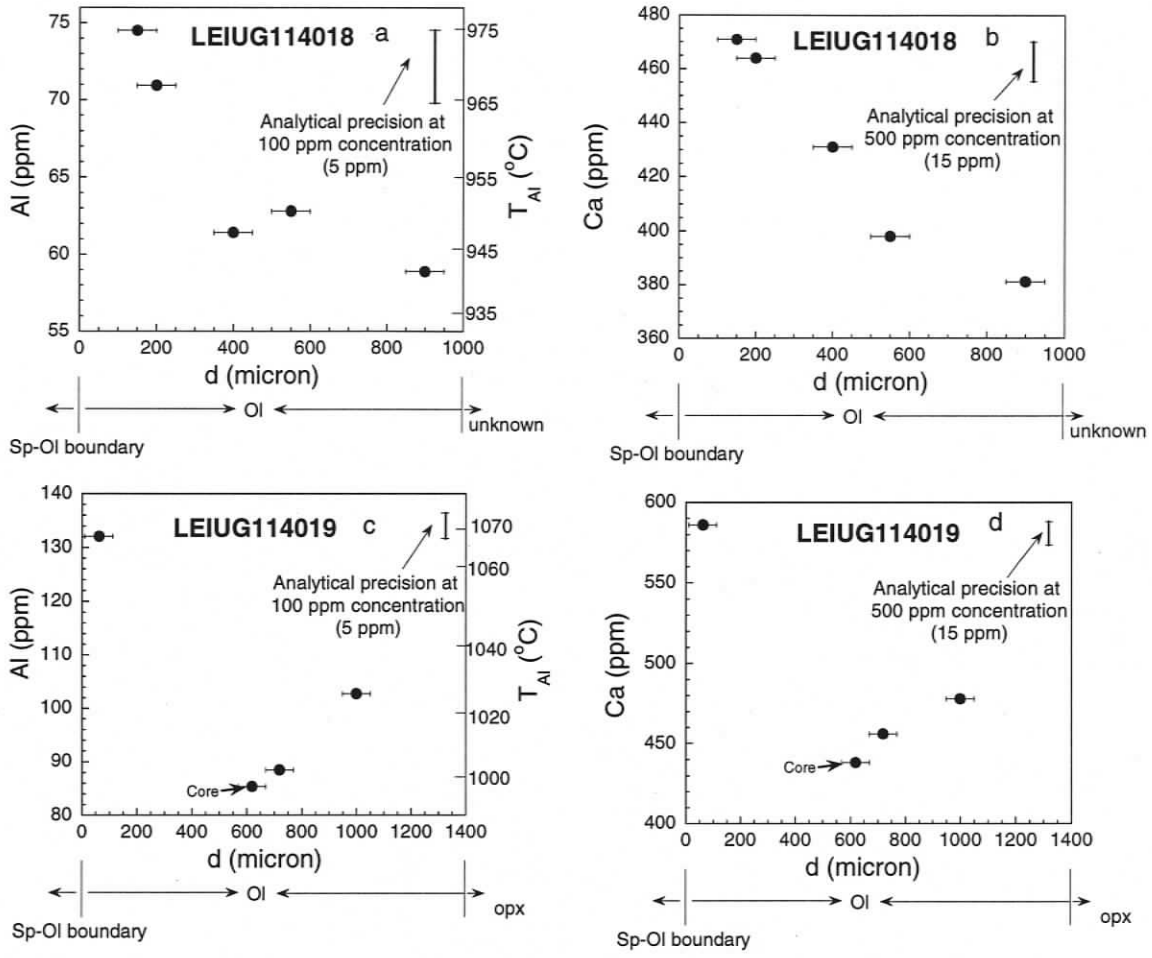

Figure 4.8 Zoning of Al and Ca in olivine for samples LEIUG114018 (a, b) and LEIUG114019 (c, d). Aluminum and Ca contents are shown on the left vertical axis. For zoning of Al in olivine, the corresponding T_{Al} values are shown on the right vertical axis. d: distance to the spinel-olivine boundary. The symbol represents the center of each analysis scan, and the error bar represents half of the width of the scan. The position of the core of the olivine crystal for sample LEIUG114018 is unknown because the olivine grain is at the edge of the thin section. The olivine crystal for sample LEIUG114019 is between a spinel crystal and an orthopyroxene crystal. Ol: olivine. Opx: orthopyroxene. Sp: spinel. Overlap of "d" for some analyses in sample LEIUG114018 is because that these analyses in olivine are at different directions away from the olivine-spinel boundary.

4.7 Future work

Future work should include: 1) improving the analytical precision of Al analyses in olivine. Since olivines from some samples only contain 5-10 ppm Al, if the Al content in olivine is analyzed by the LA-ICPMS method, the background of ^{27}Al needs to be reduced, probably using the collision cell technique, 2) the diffusion rate of Al in olivine needs to be investigated to better interpret the T_{Al} values for natural samples, and 3) detailed zoning of Ca in clinopyroxene and Al in olivine for each sample needs to be investigated to understand the thermal history of these samples and the difference between T_{Al} and T_{BKN}.

4.8 Summary

Aluminum contents in natural olivine grains were analyzed using LA-ICPMS and based on the measured Al contents, T_{Al} was calculated. Calculated T_{Al} are geologically reasonable: 630-1080°C for continental xenolith samples; 730-1030°C for samples from the oceanic lithosphere. Calculated T_{Al} was compared to temperatures calculated using the two pyroxene thermometer (T_{BKN}, Brey and Köhler, 1990) for all the natural samples, and it generally increases with increasing T_{BKN}, but is mostly about 0-200°C lower than T_{BKN}. There are several possible reasons for the difference between T_{Al} and T_{BKN}, and further work needs to be done to fully understand this. Calculated T_{Al} and T_{BKN} for four oceanic lithosphere samples represent closure temperatures. The fact that T_{Al} is about 100-240°C lower than T_{BKN} for these samples indicates that Al diffusion in olivine may be faster than Ca diffusion in clinopyroxene and orthopyroxene. The zoning of Al and Ca in olivine is used to infer the thermal histories of six xenolith samples.

References

Agee CB, Walker D (1990) Aluminum partitioning between olivine and ultrabasic silicate liquid to 6 GPa. Contributions to Mineralogy and Petrology 105:243-254

Arai S (1994) Characterization of spinel peridotites by olivine-spinel compositional relationships: Review and interpretation. Chemical Geology 113:191-204

Baker MB, Stolper EM (1994) Determining the composition of high-pressure mantle melts using diamond aggregates. Geochimica et Cosmochimica Acta 58:2811-2827

Balarm V (1997) Microwave dissolution techniques for the analysis of geological materials by ICP-MS. Current Science 73(11):1019-1023

Ballhaus C, Berry RF, Green DH (1991) High pressure experimental calibration of the olivine-orthopyroxene-spinel oxygen geobarometer: Implications for the oxidation state of the upper mantle. Contributions to Mineralogy and Petrology 107:27-40

Barnes SJ, Roeder PL (2004) The range of spinel compositions in terrestrial mafic and ultramafic rocks. Journal of Petrology 42: 2279-2302

Bartels KS, Kinzler RJ, Grove TL (1991) High pressure phase relations of primitive high-alumina basalts from Medicine Lake volcano, northern California. Contributions to Mineralogy and Petrology 108:253-270

Beattie P (1994) Systematics and energetics of trace-element partitioning between olivine and silicate melts: Implications for the nature of mineral/melt partitioning. Chemical Geology 117:57-71

Blundy J, Wood B (1994) Prediction of crystal-melt partition coefficients from elastic moduli. Nature 372:452-454

Blundy J, Wood B (2003) Trace element partitioning under crustal and uppermost mantle conditions: The influences of ionic radius, cation charge, pressure and temperature, in Holland HD, Turekian KK, Carlson RW eds. Treatise on Geochemistry 2: The Mantle and Core: 395-424. Elsevier, Amsterdam, Netherlands.

Bodinier JL, Godard M (2002) Orogenic, ophiolitic, and abyssal peridotites, in Holland HD, Turekian KK, Carlson RW eds. Treatise on Geochemistry 2: The Mantle and Core: 103-170. Elsevier, Amsterdam, Netherlands.

Boyd FR, Gurney JJ, Richardson SH (1985) Evidence for a 150-200 km thick Archaean lithosphere from diamond inclusion thermobarometry. Nature 315:387-389

Brearley M, Scarfe CM, Fujii T (1984) The petrology of ultramafic xenoliths from Summit Lake, near Prince George, British Columbia. Contributions to Mineralogy and Petrology 88:53-63

Brey GP, Köhler T (1990) Geothermobarometry in four-phase lherzolites II. New thermobarometers, and practical assessment of existing thermobarometers. Journal of Petrology 31(6):1353-1378

Bulatov VK, Girnis AV, Brey GP (2002) Experimental melting of a modally heterogeneous mantle. Mineralogy and Petrology 75:131-152

Canil D, Fedortchouk Y (2001) Olivine-liquid partitioning of vanadium and other trace elements, with applications to modern and ancient picrites. The Canadian Mineralogist 39:319-330

Canil D, O'Neill HSC (1996) Distribution of ferric iron in some upper-mantle assemblages. Journal of Petrology 37(3):609-635

Canil D, Scarfe CM (1988) Origin of phlogopite in mantle xenoliths from Kostal Lake, Wells Gray Park, British Columbia. Journal of Petrology 30(5):1159-1179

Canil D, Virgo D, Scarfe CM (1990) Oxidation state of mantle xenoliths from British Columbia, Canada. Contributions to Mineralogy and Petrology 104:453-462

Canil D, Wei K (1992) Constraints on the origin of mantle-derived low Ca garnets. Contributions to Mineralogy and Petrology 109:421-430

Chakraborty S (2006) Diffusion modeling as a tool for constraining timescales of evolution of metamorphic rocks. Mineralogy and Petrology 88:7-27

Choi KS, Lee CH, Park YJ, Joe KS, Kim WH (2001) Separation of Gold, Palladium and Platinum in chromite by anion exchange chromatography for inductively coupled plasma atomic emission spectrometric analysis. Bulletin of the Korean Chemical Society 22(8):801-804

Cohen LH, Ito K, Kennedy GC (1967) Melting and phase relations in an anhydrous basalt to 40 kilobars. American Journal of Science 265(6):475-518

Coogan LA, Jenkin GRT, Wilson RN (2002) Constraining the cooling rate of the lower oceanic crust: A new approach applied to the Oman ophiolite. Earth and Planetary Science Letters 199:127-146

Coogan LA, Thompson GM, MacLeod CJ, Dick HJB, Edwards SJ, Hosford Scheirer A, Barry TL (2004) A combined basalt and peridotite perspective on 14 million years of melt generation at the Atlantis Bank Segment of the Southwest Indian Ridge: Evidence for temporal changes in mantle dynamics? Chemical Geology 207:13-30

Deer WA, Howie RA, Zussman J (1996) An introduction to the rock-forming minerals. Longman Scientific and Technical, New York, United States.

Dessai AG, Knight K, Vaselli O (1999) Thermal structure of the lithosphere beneath the Deccan Trap along the western Indian continental margin: Evidence from xenolith data. Journal Geological Society of India 54:585-598

Dilek Y (2003) Ophiolites in earth history. Geological Society of London, London, England.

Dodson MH (1973) Closure temperature in cooling geochronological and petrological systems. Contributions to Mineralogy and Petrology 40:259-274

Dodson MH (1976) Kinetic processes and thermal history of slowly cooling solids. Nature 259:551-553

Dolezal J, Lenz J, Sulcek Z (1969) Decomposition by pressure in inorganic analysis. Analytica Chimica Acta 47(3):517-527

Droop GTR (1987) A general equation for estimating Fe^{3+} concentrations in ferromagnesian silicates and oxides from microprobe analyses, using stoichiometric criteria. Mineralogical Magazine 51:431-435

Eggins SM, Woodhead JD, Kinsley LPJ, Mortimer GE, Sylvester P, McCulloch MT, Hergt JM, Handler MR (1997) A simple method for precise determination of $\geq$ 40 trace elements in geological samples by ICPMS using enriched isotope internal standardization. Chemical Geology 134:311-326

Elkins-Tanton LT, Grove TL (2003) Evidence for deep melting of hydrous metasomatized mantle: Pliocene high-potassium magmas from the Sierra Nevadas. Journal of Geophysical Research 108(B7):#2350

Fabries J (1979) Spinel-olivine geothermometry in peridotites from ultramafic complexes. Contributions to Mineralogy and Petrology 69:329-336

Fujii T, Scarfe CM (1982) Petrology of ultramafic nodules from West Kettle River, near Kelowna, Southern British Columbia. Contributions to Mineralogy and Petrology 80:297-306

Gaetani GA, Grove TL (1998) The influence of water on melting of mantle peridotite. Contributions to Mineralogy and Petrology 131:323-346

Garrido CJ, Bodinier JL, Alard O (2000) Incompatible trace element partitioning and residence in anhydrous spinel peridotites and websterites from the Ronda orogenic peridotite. Earth and Planetary Science Letters 181:341-358

Gaul OF, Griffin WL, O'Reilly SY, Pearson NJ (2000) Mapping olivine composition in the lithospheric mantle. Earth and Planetary Science Letters 182:223-235

Green DH, Ringwood AE (1967) The stability fields of aluminous pyroxene peridotite and garnet peridotite and their relevance in upper mantle structure. Earth and Planetary Science Letters 3:151-160

Grove TL, Bryan WB (1983) Fractionation of pyroxene-phyric MORB at low pressure: An experimental study. Contributions to Mineralogy and Petrology 84:293-309

Hanson B, Jones JH (1998) The systematics of Cr^{3+} and Cr^{2+} partitioning between olivine and liquid in the presence of spinel. American Mineralogist 83:669-684

Harley SL (1984) An experimental study of the partitioning of Fe and Mg between garnet and orthopyroxene. Contributions to Mineralogy and Petrology 86:359-373

Harris DC (1987) Quantitative chemical analysis, W.H. Freeman, New York, United States.

Iglesias M, Vaculovic T, Studynkova J, Poussel E, Mermet JM (2004) Influence of the operating conditions and of the optical transition on non-spectral matrix effects in inductively coupled plasma-atomic emission spectrometry, in Durig JR, Veken BJ, Johansson LBA eds. Spectrochimica Acta Part B: Atomic Spectroscopy. 59:1841-1850 Elsevier Science, Amsterdam, Netherlands.

Ionov DA, Wood BJ (1992) The oxidation state of subcontinental mantle: Oxygen thermobarometry of mantle xenoliths from central Asia. Contributions to Mineralogy and Petrology 111:179-193

Irvine TN (1965) Chromian spinel as a petrogenetic indicator I: Theory. Canadian Journal of Earth Sciences 2:648-672

Jurczyk J, Buhl F, Wilczek I (1993) Semimicro quantitative X-ray-fluorescence solution method for the analysis of spinels – determination of Cu, Ga, Zn, In, Cr and Se in monocrystals and polycrystals. Chemia Analityczna 38(4):519-526

Kessel R, Beckett JR, Stolper EM (2007) The thermal history of equilibrated ordinary chondrites and the relationship between textural maturity and temperature. Geochimica et Cosmochimica Acta 71:1855-1881

Kinzler RJ (1997) Melting of mantle peridotite at pressures approaching the spinel to garnet transition: Application to mid-ocean ridge basalt petrogenesis. Journal of Geophysical Research 102(B1):853-874

Kinzler RJ, Grove TL (1992) Primary magmas of mid-ocean ridge basalts 1. Experiments and methods. Journal of Geophysical Research 97(B5):6885-6906

Klemme S (2004) The influence of Cr on the garnet-spinel transition in the Earth's mantle: Experiments in the system MgO-Cr_2O_3-SiO_2 and thermodynamic modeling. Lithos 77:639-646

Köhler TP, Brey GP (1990) Calcium exchange between olivine and clinopyroxene calibrated as a geothermobarometer for natural peridotites from 2 to 60 kb with applications. Geochimica et Cosmochimica Acta 54:2375-2388

Kopylova MG, Russell JK, Cookenboo H (1999) Petrology of peridotite and pyroxenite xenoliths from the Jericho kimberlite: Implications for the thermal state of the mantle beneath the Slave Craton, northern Canada. Journal of Petrology 40(1):79-104

Kretz R (1994) Metamorphic Crystallization. John Wiley and Sons, Chichester, England.

Krogh EJ (1988) The garnet-clinopyroxene Fe-Mg geothermometer – A reinterpretation of existing experimental data. Contributions to Mineralogy and Petrology 99:44-48

Kushiro I, Yoder HS (1966) Anorthite-Forsterite and Anorthite – Enstatite Reaction and their bearing on the Basalt-Eclogite Transformation. Journal of Petrology 7(3):337-362

Laporte D, Toplis MJ, Seyler M, Devidal JL (2004) A new experimental technique for extracting liquids from peridotite at very low degrees of melting application to partial melting of depleted peridotite. Contributions to Mineralogy and Petrology 146:463-484

Larrea MT, Pinilla IG, Farinas JC (1997) Microwave-assisted acid dissolution of sintered advanced ceramics for inductively coupled plasma atomic emission spectrometry. Journal of Analytical Atomic Spectrometry 12:1323-1332

Lasaga AC (1983) Geospeedometry: an extension of geothermometry, in Saxena SK eds. Kinetics and Equilibrium in Mineral Reactions (Advances in Physical Geochemistry): 81-114. Springer-Verlag Berlin Heidelberg, New York, United States.

Lagasse P, Goldman L, Hobson A, Norton SR (2001) Columbia Encyclopedia, 6th Edition. Columbia University Press, New York, United States.

Longerich HP, Diegor W (2001) Introduction to mass spectrometry, in Laser-Ablation-ICPMS in the Earth Sciences, Sylvester P eds. Mineralogical Association of Canada, Canada: 1-19

Meisel T, Reisberg L, Moser J, Carignan J, Melcher F, Brugmann G (2003) Re-Os systematics of UB-N, a serpentinized peridotite reference material. Chemical Geology 201:161-179

Mori T (1977) Geothermometry of spinel lherzolites. Contributions to Mineralogy and Petrology 59:261-279

Mukhopadhyay B, Basu S, Holdaway MJ (1993) A discussion of Margules-type formulations for multicomponent solutions with a generalized approach. Geochimica et Cosmochimica Acta 57:277-283

Nasir S, Safarjalani A (2000) Lithospheric petrology beneath the northern part of the Arabian Plate in Syria: Evidence from xenoliths in alkali basalts. Journal of African Earth Sciences 30(1):149-168

Nickel KG, Green DH (1985) Empirical geothermobarometry for garnet peridotites and implications for the nature of the lithosphere, kimberlites and diamonds. Earth and Planetary Science Letters 73:158-170

Nielsen RL, Gallahan WE, Newberger F (1992) Experimentally determined mineral-melt partition coefficients for Sc, Y and REE for olivine, orthopyroxene, pigeonite, magnetite and ilmenite. Contributions to Mineralogy and Petrology 110:488-499

Oak Y, Steinke P, Chatterjee ND (1984) Thermodynamic mixing properties of $Mg(Al,Cr)_2O_4$ spinel crystalline solution at high temperatures and pressure. Contributions to Mineralogy and Petrology 87:196-204

O'Neill HSC, Eggins SM (2002) The effect of melt composition on trace element partitioning: An experimental investigation of the activity coefficients of FeO, NiO, CoO, MoO_2 and MoO_3 in silicate melts. Chemical Geology 19:151-181

O'Neill HSC, Wall VJ (1987) The olivine-orthopyroxene-spinel oxygen geobarometer, the nickel precipitation curve, and the oxygen fugacity of the earth's upper mantle. Journal of Petrology 28(6):1169-1191

Parman SW, Dann JC, Grove TL, deWit MJ (1997) Emplacement conditions of komatiite magmas from the 3.49 Ga Komati Formation, Barberton Greenstone Belt, South Africa. Earth and Planetary Science Letters 150:303-323

Pearson NJ, O'Reilly SY, Griffin WL (1995) The crust-mantle boundary beneath cratons and craton margins: A transect across the south-west margin of the Kaapvaal craton. Lithos 36:257-287

Peslier AH, Francis D, Ludden J (2002) The lithospheric mantle beneath continental margins: melting and melt-rock reaction in Canadian Cordillera xenoliths. Journal of Petrology 43:2013-2047

Pickering-Witter J, Johnston AD (2000) The effects of variable bulk composition on the melting systematics of fertile peridotitic assemblages. Contributions to Mineralogy and Petrology 140:190-211

Poustovetov AA, Roeder PL (2001) Numerical modeling of major element distribution between chromian spinel and basaltic melt, with application to chromian spinel in MORBs. Contributions to Mineralogy and Petrology 142:58-71

Righter K, Campbell AJ, Humayun M, Hervig RL (2004) Partitioning of Ru, Rh, Pd, Re, Ir, and Au between Cr-bearing spinel, olivine, pyroxene and silicate melts. Geochimica et Cosmochimica Acta 68:867-880

Robinson JAC, Wood BJ, Blundy JD (1998) The beginning of melting of fertile and depleted peridotite at 1.5 GPa. Earth and Planetary Science Letters 155:97-111

Roeder PL, Reynolds I (1991) Crystallization of chromite and chromium solubility in basaltic melts. Journal of Petrology 32(5):909-934

Rooney TO, Furman T, Yirgu G, Ayalew D (2005) Structure of the Ethiopian lithosphere: Xenolith evidence in the Main Ethiopian Rift. Geochimica et Cosmochimica Acta 69(15):3889-3910

Rudnick RL, McDonough WF, O'Connell RJ (1998) Thermal structure, thickness and composition of continental lithosphere. Chemical Geology 145:395-411

Rudnick RL, Gao S, Ling W, Liu Y, McDonough WF (2004) Petrology and geochemistry of spinel peridotite xenoliths from Hannuoba and Qixia, North China craton. Lithos 77:609-637

Sack RO, Ghiorso MS (1991a) An internally consistent model for the thermodynamic properties of Fe-Mg-titanomagnetite-aluminate spinels. Contributions to Mineralogy and Petrology 106:474-505

Sack RO, Ghiorso MS (1991b) Chromian spinels as petrogenetic indicators: Thermodynamics and petrological applications. American Mineralogist 76:827-847

Salters VJM, Lonshi JE, Bizimis M (2002) Near mantle solidus trace element partitioning at pressure up to 3.4 GPa. Geochemistry, Geophysics, Geosystems 3(7):1-23

Schwab BE, Johnston AD (2001) Melting systematics of modally variable, compositionally intermediate peridotites and the effects of mineral fertility. Journal of Petrology 42(10):1789-1811

Shimizu H, Sangen K, Masuda A (1982) Experimental study on rare-earth element partitioning in olivine and clinopyroxene formed at 10 and 20 kb for basaltic systems. Geochemical Journal 16:107-117

Sisson TW, Grove TL (1993) Experimental investigations of the role of H_2O in calc-alkaline differentiation and subduction zone magmatism. Contributions to Mineralogy and Petrology 113:143-166

Smith D (1999) Temperature and pressures of mineral equilibration in peridotite xenoliths: Review, discussion, and implications, in Fei YW, Bertka CM, Mysen BO eds. Mantle Petrology: Field Observations and High Pressure Experimentation (A Tribute to Francis R. (Joe) Boyd): 171-188. The Geochemical Society, Houston, United States.

Spear FS (1991) On the interpretation of peak metamorphic temperatures in light of garnet diffusion during cooling. Journal of Metamorphic Geology 9(4):379-388

Stosch HG (1981) Sc, Cr, Co and Ni partitioning between minerals from spinel peridotite xenoliths. Contributions to Mineralogy and Petrology 78:166-174

Sung CM, Burns RG (1978) Crystal structural features of the olivine→spinel transition. Physics and Chemistry of Minerals 2:177-197

Taura H, Yurimoto H, Kurita K, Sueno S (1998) Pressure dependence on partition coefficients for trace elements between olivine and the coexisting melts. Physics and Chemistry of Minerals 25:469-484

Thomas R (2001a) A beginner's guide to ICP-MS, Part I. Spectroscopy 16(4):38-42

Thomas R (2001b) A beginner's guide to ICP-MS, Part II: The sample-introduction system. Spectroscopy 16(5):56-60

Thomas R (2001c) A beginner's guide to ICP-MS, Part III: The plasma source. Spectroscopy 16(6):26-30

Timpa S, Gillis KM, Canil D (2005) Accretion-related metamorphism of the Metchosin Igneous Complex, southern Vancouver Island, British Columbia. Canadian Journal of Earth Sciences 42:1467-1479

Tormey DR, Grove TL, Bryan WB (1987) Experimental petrology of normal MORB near the Kane Fracture Zone: 22°-25° N, mid-Atlantic ridge. Contributions to Mineralogy and Petrology 96:121-139

Walter MJ (1998) Melting of garnet peridotite and the origin of komatiite and depleted lithosphere. Journal of Petrology 39:29-60

Wasylenki LE, Baker MB, Kent AJR, Stolper EM (2003) Near-solidus melting of the shallow upper mantle: Partial melting experiments on depleted peridotite. Journal of Petrology 44(7):1163-1191

White MW (1995) Geochemistry. An on-line textbook, eventually to be published by John-Hopkins University Press, United States. Online link: http://www.geo.cornell.edu/geology/classes/Chapters/

Will TM (1998) Phase equilibria in metamorphic rocks – Thermodynamic background and petrological applications. Springer-Verlag Berlin Heidelberg, New York, United States.

Winter JD (2001) An introduction to igneous and metamorphic petrology. Prentice Hall, New Jersey, United States.

Witt-Eickschen G, O'Neill HSC (2005) The effect of temperature on the equilibrium distribution of trace elements between clinopyroxene, orthopyroxene, olivine and spinel in upper mantle peridotite. Chemical Geology 221:65-101

Wood BJ, Fraser DG (1976) Elementary thermodynamics for geologists, Oxford University Press, Oxford, England.

Wood AB, Kornprobst J, Wood BJ (1992) Oxygen thermobarometry of lherzolite massifs. Journal of Petrology 33:203-230

Xu Y, Lin C, Shi L (1999) The geotherm of the lithosphere beneath Qilin, SE China: A re-appraisal and implications for P-T estimation of Fe-rich pyroxenites. Lithos 47:181-193

Yang HJ, Kinzler RJ, Grove TL (1996) Experiments and models of anhydrous, basaltic olivine-plagioclase-augite saturated melts from 0.001 to 10 kbar. Contributions to Mineralogy and Petrology 124:1-18

Ying J, Zhang H, Kita N, Morishita Y, Shimoda G (2006) Nature and evolution of Late Cretaceous lithospheric mantle beneath the eastern North China Craton: Constraints from petrology and geochemistry of peridotitic xenoliths from Junan, Shandong Province, China. Earth and Planetary Science Letters 244:622-638

Appendix 1

Summary of published methods on spinel digestion and developed fusion methods in this study

Source	Method	Reagents	T (°C)	P	Reagent: sample	Dur (h)	Cr#-sp	Material being dissolved	Note
Jurczyk et al, 1993	Hot plate	HCl	-	1atm	3ml: 25 mg	-	-	Cu/Ga/Cr/Se sp	-
Jurczyk et al, 1993	Hot plate	HCl	-	1atm	3ml: 10 mg	-	-	Zn/In/Cr/Se sp	-
Rudnick et al, 2004	Hot plate	$HF + HNO_3 + HClO_4$	185	1atm	-	48	-	Sp peridotite powder (200 mesh)	-
Garrido et al, 2000	Hot plate	$H_2SO_4 + HClO_4$	160	1atm	-	336	-	250-110 micron peridtite powder	-
Eggins et al, 1997	Hot plate	$10HF\text{-}1HNO_3$	*<310	1atm	-	168	0.12-0.44	Peridotite sample	Ultrasonic and hotplate alteration
Choi et al, 2001	Hot plate	$HClO_4\text{-}H_3PO_4$	-	1atm	-		0	Sp and chr	-
Dolezal et al, 1969	Hot plate	$12H_2SO_4+1HClO_4$	240	1atm	13ml:300mg	10			-
Meisel et al, 2003	Fusion	$1NaOH+1Na_2O_2$	325-625	1atm	8:1	1	0.1		-
Choi et al, 2001	Fusion	Na_2O_2	600	1atm	10:1	0.5	-	Cr-rich spinel	-
http://listserv.syr.edu/archives/plasmachem-l.html	Fusion	$BLiO_2$ / $B_4Li_2O_7$		1atm	13:1	0.4	-	Cr-rich spinel;	350-650 W powder was employed
Balaram, 1997	MW	$5aqua\ regia+3HF+2HClO_4$	210	≤625 psi	10ml:0.5g	1	-	Cr-rich spinel	-
Larrea et al, 1997	MW	1HCl +1HF	-	≤200 psi	6ml:100mg	0.5	0	5-10 micron sp powder,	180-240 W power was employed
Present study	Fusion	$Na_2B_4O_7$	950	1atm	9:1	0.5	0	Cr-free and Cr-rich spinels	0.5g Bead was dissolved in 5ml 10% HNO_3 at 60°C in 0.25 h
Present study	Fusion	$Na_2B_4O_7$	950	1atm	23:1	0.5	0.77	Same as above	Same as above

T: temperature. P: pressure. Dur: duration. Cr#-sp: $Cr/(Cr+Al+Fe^{3+})$ in spinel. MW: microwave. "-" means that relevant information was not found in the literature. *: temperature was assumed according to the melting point of the Savillex Teflon beaker.

Appendix 2

Unsuccessful spinel digestion test in this study

Label	Method	reagents	T (°C)	P	Reagent: sample	Dur (h)	Cr#
1	Hot plate	HCl	180	1atm	5ml:0.9mg	12	0
2	Hot plate	$1HCl+4HNO_3$	180	1atm	5ml:1.3mg	12	0
3	MW	HCl	175	400psi	10ml:0.5mg	0.5	0
4	MW	$4HCl+1HNO_3$	175	400psi	11.25ml:0.4mg	0.5	0
5	MW	1HF+6HCl	200, 250, 200	50, 180, 400 psi	1.4ml:0.02g	0.5, 1, 1	0
6	MW	$1HF+6HNO_3$	200, 250, 200	50, 180, 400 psi	1.4ml:0.02g	0.5, 1, 1	0
7	MW	$2HF+1HCl+8HNO_3$	200, 250, 200	50, 180, 400 psi	1.1ml:0.02g	0.5, 1, 1	0
8	MW	1HF+6HCl	200, 250, 200	50, 180, 400 psi	1.4ml:0.02g	0.5, 1, 1	0.77
9	MW	$1HF+6HNO_3$	200, 250, 200	50, 180, 400 psi	1.4ml:0.02g	0.5, 1, 1	0.77
10	MW	$2HF+1HCl+8HNO_3$	200, 250, 200	50, 180, 400 psi	1.1ml:0.02g	0.5, 1, 1	0.77

T: temperature. P: pressure. Dur: duration. Cr#: $Cr/(Cr+Al+Fe^{3+})$ in spinel. MW: microwave. For methods 4-10, three stages of microwave digestion were employed. Three numbers in T, P, and Dur columns represent the temperature and pressure conditions and duration for three stages. An interval of 12 hours was employed between each stage.

Appendix 3

Calcium contents in different olivine grains from the first set of samples.

Sample	Type	Location	Ca (ppm)						
			1	2	3	4	5	Ave	1σ
FRB1530	On-C	S Africa	347	405	469	463		421	57
89-777	On-C	Tanzania	246	255	260	261	264	257	7
89-661	On-C	Tanzania	284	326	321	313	346	318	23
22-1	On-C	Jericho Kim	242	355	346	300	303	309	45
22-4	On-C	Jericho Kim	229	218	237			228	10
26-11	On-C	Jericho Kim	273	405				339	93
25-4	On-C	Jericho Kim	368	357	322			349	24
22-5	On-C	Jericho Kim	229	260	232	249		243	15
84-402	Off-C	SE Australia	411	433	468	416	448	435	23
2905	Off-C	SE Australia	451	458	499	478	500	477	23
85-168	Off-C	SE Australia	480	496	419	451	417	453	35
JL1	Off-C	BC JL	314	310	311	313	321	314	4
JL8	Off-C	BC JL	338	328	432	406	331	367	48
TKN15	Off-C	BC BS	348	338	320	338	347	338	11
KLBR-1	Off-C	BC KL	464	423	469	470	469	459	20
SL47	Off-C	BC SL	651	666	627	679	678	660	22
2004OL24	Ocean	Oman	442	366	360			389	46
2001OL43	Ocean	Oman	338					338	
2001OL4	Ocean	Oman	364	338	376	315	301	339	32
6K-465-002	Ocean	SWIR	421	466	429	478	446	448	24

"1", "2", "3", "4", and "5" represent the grain number. Ave: average. 1σ: one standard deviation. On-C: On-craton xenolith. Off-C: Off-craton xenolith. Ocean: oceanic lithosphere. S Africa: South Africa. Kim: kimberlite. BC: British Columbia. JL: Jaques Lake. BS: Boss Mountain. KL: Kostal Lake. SL: Summit Lake. SWIR: Southwest Indian Ridge. Ave: average. 1σ: one standard deviation.

Appendix 4

Calcium concentrations in olivine from the second analytical session designed to examine the zoning of Ca in olivine.

LEIUG114018		LEIUG114019		22-4		22-5		25-4		26-11	
d (μm)	Ca (ppm)	d (μm)	Ca (ppm)	d (μm)	Ca (ppm)	d (μm)	Ca (ppm)	d (μm)	Ca (ppm)	d (μm)	Ca (ppm)
150	471	62	589	150	254	100	353	90	257	130	226
200	464	620	438	330	245	230	231	250	241	420	228
400	431	720	456	330	240	525	239	480	238	1040	245
550	398	1000	478	500	237	730	227	520	241		
900	381			570	237	920	225	675	241		
				780	232	1120	233				
				610	234	1400	236				

d: distance to the olivine-spinel boundary.